ABSTRACT

Title: Estimating the fraction of absorbed photosynthetically active radiation from multiple satellite data

Xin Tao, Doctor of Philosophy, 2015

Directed by: Dr. Shunlin Liang, Professor
Department of Geographical Sciences

The fraction of absorbed photosynthetically active radiation (FAPAR) is a critical input parameter in many climate and ecological models. The accuracy of satellite FAPAR products directly influences estimates of ecosystem productivity and carbon stocks. The targeted accuracy of FAPAR products is 10%, or 0.05, for many applications. This study evaluates satellite FAPAR products, presents a new FAPAR estimation model and develops data fusion schemes to improve the FAPAR accuracy.

Five global FAPAR products, namely MODIS, MISR, MERIS, SeaWiFS, and GEOV1 were intercompared over different land covers and directly validated with ground measurements at VAlidation of Land European Remote sensing Instruments (VALERI) and AmeriFlux sites. Intercomparison results show that MODIS, MISR, and GEOV1 agree well with each other and so do MERIS and SeaWiFS, but the difference between these two groups can be as large as 0.1. The differences between the products are consistent throughout the year over most of the land cover types, except over the forests, because of the different assumptions in the retrieval

algorithms and the differences between green and total FAPAR products over forests. Direct validation results show that the five FAPAR products have an uncertainty of 0.14 when validating with total FAPAR measurements, and 0.09 when validating with green FAPAR measurements. Overall, current FAPAR products are close to, but have not fulfilled, the accuracy requirement, and further improvements are still needed.

A new FAPAR estimation model was developed based on the radiative transfer for horizontally homogeneous continuous canopy to improve the FAPAR accuracy. A spatially explicit parameterization of leaf canopy and soil background reflectance was derived from a thirteen years of MODIS albedo database. The new algorithm requires the input of leaf area index (LAI), which was estimated by a hybrid geometric optic-radiative transfer model suitable for both continuous and discrete vegetation canopies in this study. The FAPAR estimates by the new model was intercompared with reference satellite FAPAR products and validated with field measurements at the VALERI and AmeriFlux experimental sites. The validation results showed that the FAPAR estimates by the new method had slightly better performance than the MODIS and the MISR FAPAR products when using corresponding satellite LAI product values as input. The FAPAR estimates can be further improved with the LAI estimates from the presented model as input. The improvements are apparent at grasslands and forests with an 8% reduction of uncertainty. The new model can successfully identify the growing seasons and produce smooth time series curves of estimated FAPAR over years. The root mean square error (RMSE) was reduced from 0.16 to 0.11 for MODIS and from 0.18 to 0.1 for MISR overall. Application of the

presented model at a regional scale generated consistent FAPAR maps at 30 m, 500 m, and 1100 m spatial resolutions from the Landsat, MODIS, and MISR data.

As an alternative method to improve FAPAR accuracy, in addition to developing FAPAR estimation models, two data fusion schemes were applied to integrate multiple satellite FAPAR products at two scales: optimal interpolation at the site scale and multiple resolution tree at the regional scale. These two fusion schemes removed the bias and resulted in a 20% increase in the R^2 and a 3% reduction in the RMSE as compared with the average of the individual FAPAR products. The regional scale fusion filled in the missing values and provided spatially consistent FAPAR distributions at different resolutions.

The original contribution of this study is that multiple FAPAR products have been assessed with a comprehensive set of measurements from two field experiments at the global scale. This study improved the accuracy of FAPAR using a new model and local pixel based soil background and leaf canopy albedos. High FAPAR accuracy was achieved through integration at both the temporal and spatial domains. The improved accuracy of FAPAR values from this study by 5% would help to decrease an equal amount of uncertainty in the estimation of gross and net primary production and carbon fluxes.

ESTIMATING THE FRACTION OF ABSORBED PHOTOSYNTHETICALLY ACTIVE RADIATION FROM MULTIPLE SATELLITE DATA

By

Xin Tao

Dissertation submitted to the Faculty of the Graduate School of the
University of Maryland, College Park, in partial fulfillment
of the requirements for the degree of
Doctor of Philosophy
2015

Advisory Committee:

Dr. Shunlin Liang, Chair
Dr. George C. Hurtt
Dr. Zhanqing Li
Dr. Tatiana V. Loboda
Dr. Dongdong Wang

Acknowledgements

I would like to thank the Ameriflux and VALERI PIs and staff for publishing the in situ data (WWW1, WWW2). I thank the MODIS land product processing team at Oak Ridge National Laboratory Distributed Active Archive Center for the MODIS Collection 5 data (WWW3). I am thankful to the EOS MISR, ESA MERIS, and geoland2 GEOV1 land processing teams (WWW4, WWW5, WWW6). I would like to thank the SeaWiFS project and the Distributed Active Archive Center at the Goddard Space Flight Center for the production and distribution of the SeaWiFS data as well (WWW7). I am also thankful to the NASA LEDAPS project team members for the atmospheric correction preprocessing code (WWW8).

I would like to express my gratitude to my advisor Dr. Shunlin Liang, and dissertation advisory committee members: Dr. George C. Hurtt, Dr. Zhanqing Li, Dr. Tatiana V. Loboda, and Dr. Dongdong Wang for their helpful comments and suggestions on this study. This dissertation would not be possible without their help. I am thankful to the group members I worked with as well. Thank you all for your helps and suggestions.

Table of Contents

List of Tables

List of Figures

Chapter 1 Introduction

Vegetation plays a key role in the global energy balance, carbon cycle, and water budget of the Earth by controlling the exchanges between the lower atmosphere and the continental biosphere. For example, photosynthesis is responsible for the conversion of about 50 PgC yr^{-1} of atmospheric CO_2 into biomass, which represents about 10% of the atmospheric carbon (Carrer et al., 2013). Land use changes, mainly due to deforestation, lead to the emission of 1.7 PgC yr^{-1} in the tropics, offsetting by a small amount of uptake (about 0.1 PgC) in temperate and boreal areas—thereby producing a net source of around 1.6 PgC yr^{-1} (Houghton, 1995). One of the most important factors to monitor vegetation status is the distribution of the fraction of absorbed photosynthetically active radiation (FAPAR, or FPAR) within vegetation as it constrains the photosynthesis rate. The FAPAR is the fraction of incoming solar radiation in the spectral range from 400 nm to 700 nm that is absorbed by plants (Liang et al., 2012). FAPAR is one of the 50 Essential Climate Variables (ECVs) recognized by the UN Global Climate Observing System (GCOS, 2011). FAPAR is a critical input parameter in the biogeophysical and biogeochemical processes described by many climate and ecological models (e.g., Community Land Model, Community Earth System Model, and crop growth models) (Bonan et al., 2002; Kaminski et al., 2012; Maselli et al., 2008; Tian et al., 2004). The MODIS FAPAR product (MOD15) is a critical input for MODIS evapotranspiration (MOD16) and gross primary production (GPP) and net primary production (NPP) products (MOD17) (Liang et al., 2012). A 10% increase in FAPAR would result in an equal amount

increase of gross and net primary production and carbon sink. Hall et al. (2006) conducted sensitivity analysis and found that NPP is largely driven by FAPAR in the Carnegie Ames Stanford Approach (CASA) model, with weaker effects from the lower variability of PAR and lower sensitivity to temperature and precipitation.

Despite the fact the aforementioned numbers exist, the spatial distributions of carbon sources and sinks still remain a core question, being a debate for a broad scientific community. In this regard, a better representation of vegetation status in the ecological modeling is desirable. The reliable estimates of gross and net primary production and carbon flux depend on a high accuracy of FAPAR as an input. An accuracy of ±0.05 or relative accuracy of 10% in FAPAR is considered acceptable to describe the vegetation attribute exactly and be effectively applied in agronomical and other applications (GCOS, 2011).

The remainder of this chapter is organized as follows. Section 1.1 introduces the FAPAR estimation methods from optical remote sensing. Section 1.2 briefly summarizes the accuracy of the FAPAR products used in this study. Possible solutions to improve the FAPAR accuracy are presented in Section 1.3. The objectives and the flowcharts of this study are presented in Section 1.4.

1.1. FAPAR Estimation Methods

FAPAR can be collected from field measurements at a point scale, but the monitoring network of ground measurements is not sufficient for global coverage (Li et al., 1995). Satellite sensors acquire land surface information at regional and global scales efficiently, and they represent new opportunities for monitoring biophysical

parameters (Asner et al., 1998). The remote sensing retrievals of FAPAR are often validated by the in situ measured FAPAR in order to improve the FAPAR estimates.

Estimating FAPAR from optical remote sensing can be based on physical models or empirical relationships (Liang, 2007). Statistical models build empirical relationships between FAPAR and observations or derivatives from observations without knowledge of the underlying physical mechanism in the radiative transfer process, and therefore simplicity is its primary advantage (Gobron et al., 1999). However, no unique relation between FAPAR and vegetation index is generally applicable everywhere, as canopy reflectance also depends on other factors, such as measurement geometry, spatial resolution, and land cover types (Asrar et al., 1992; Friedl, 1997). Moreover, the relation between FAPAR and vegetation index such as normalized difference vegetation index (NDVI) is quite sensitive to the reflectance of background material (Asrar et al., 1992). The relation may also suffer the saturation problem for dense vegetation. With regard to the sensitivity of the empirical relationships to the aforementioned factors, this study mainly focuses on FAPAR retrieval using physical models instead.

Physical models analyze the interactions between solar radiation and vegetation canopy and reveal cause-effect relations (Pinty et al., 2011; Widlowski et al., 2007). Canopy reflectance models for retrieving biophysical characteristics from reflected radiation can be divided into four classes (Liang, 2004): radiative transfer (RT), geometric-optical, hybrid, and Monte Carlo and other computer simulations. Radiative transfer models consider single and multiple scattering, and are especially applicable to continuous vegetation canopy, such as grass and tropical forests, which

are prevalent in moderate to high resolution images. Considering the characteristic of moderate spatial resolution of the MODIS, the Multi-angle Imaging SpectroRadiometer (MISR) and the Landsat data used in this study, a RT model is developed to calculate FAPAR. As an input for FAPAR, Leaf area index (LAI) is calculated using a hybrid geometric-optic radiative transfer model. The results are validated at the site scale and the method is applied at the regional scale.

1.2. The Accuracy of Existing FAPAR Products

The accuracy of the satellite FAPAR products directly influences estimates of ecosystem productivity and carbon stocks. A relative accuracy of 10%, or absolute accuracy of ±0.05, in FAPAR is considered acceptable in agronomical and other applications (GCOS, 2011). MODIS Collection 4 FAPAR product is validated with ground-based measurements in early studies (Baret et al., 2007; Fensholt et al., 2004; Huemmrich et al., 2005; Olofsson and Eklundh, 2007; Steinberg et al., 2006; Turner et al., 2005; Weiss et al., 2007; Yang et al., 2006). The improved performance of Collection 5 over Collection 4 LAI/FAPAR products is demonstrated before the public release by Shabanov et al. (2005). Recently, the MODIS Collection 5 FAPAR product is assessed or compared with other products and has been shown to improve accuracy over Collection 4 from 0.2 to 0.1 (Baret et al., 2013; Camacho et al., 2013; Martinez et al., 2013; McCallum et al., 2010; Pickett-Heaps et al., 2014). An intermediate MODIS FAPAR Collection 4.1 product fixes the bug that existed in Collection 4, and its performance is assessed to have improved over Collection 4 but not as good as Collection 5 (Seixas et al., 2009; Serbin et al., 2013). The MERIS FAPAR product has been assessed or compared with other FAPAR products and

validated to show an accuracy of 0.1 to 0.12 (D'Odorico et al., 2014; Gobron et al., 2008; Martinez et al., 2013; Pickett-Heaps et al., 2014; Seixas et al., 2009). The Sea-Viewing Wide Field-of-View Sensor (SeaWiFS) FAPAR product has been compared with other FAPAR products and evaluated to have an accuracy of 0.1 to 0.23 in the studies by Wang et al. (2001), Gobron et al. (2006), McCallum et al. (2010), Camacho et al. (2013), and Pickett-Heaps et al. (2014). The GEOV1 FAPAR is intercompared against MODIS Collection 5 and SeaWiFS products and validated to have the best performance with an accuracy of 0.08 (Baret et al., 2013; Camacho et al., 2013). However, few studies have evaluated the MISR FAPAR product (Hu et al., 2007). Currently, no intercomparison studies of MISR FAPAR product and other FAPAR products exist. The intercomparison of the products at various scales would help to understand and reduce large systematic biases among the magnitudes of existing products. In consideration of the need to evaluate current FAPAR products, Chapter 2 focuses on a comprehensive evaluation of the performances of MISR, MODIS, SeaWiFS, MERIS, and GEOV1 FAPAR products at the global scale.

1.3. Need for Improved FAPAR Estimates

Direct validation of satellite FAPAR products with ground measurements generates some encouraging results, especially when compared with previous versions of FAPAR products. The improvement could be a result of a new stochastic RT model, which captures well the 3D effects of foliage clumping and species mixtures of natural ecosystems (Kanniah et al., 2009). The MISR FAPAR product has a similar performance as the MODIS C5 FAPAR product. However, the MODIS and the MISR FAPAR products might overestimate at some sites. For example, Martinez et al.

(2013) point out that MODIS shows a tendency to provide high values in cultivated areas and the Mediterranean forest, such as Puechabon. The MODIS FAPAR product may also have a positive bias for very low FAPAR values. A similar overestimation problem is found in MISR FAPAR data, with a positive bias as large as 0.16 in broadleaf forests (Hu et al., 2007).

The determinants of FAPAR accuracy can be traced to the performance of retrieval models and the accuracy of input parameters, such as leaf area index (LAI), soil background reflectance, or fractional canopy cover. LAI is one of the most important parameters to determine FAPAR, and its accuracy directly influences the accuracy of FAPAR. A 10% change in tree LAI could account for a 55% change in FAPAR (Asner et al., 1998). The collection of soil background reflectance is important in guaranteeing that the simulated reflectance could cover the whole set of observed surface reflectance data (Fang et al., 2012; Knyazikhin et al., 1998b; Shabanov et al., 2005). Otherwise, a saturation problem may occur and very high FAPAR values are not reliable (Weiss et al., 2007). The correct estimation of FAPAR also relies on the correct estimation of fractional canopy cover, the underestimation of which might cause unrealistically high FAPAR values calculated from the observations of surface reflectance (Kanniah et al., 2009). Possible solutions to improve the FAPAR accuracy may include (1) developing new FAPAR retrieval models suitable for different land cover types, and (2) simultaneous improvement of the accuracy of model parameters such as LAI and soil background and leaf canopy albedos.

An alternative to developing new models to improve the accuracy of FAPAR estimation is to integrate multiple data products considering their characteristics and

accuracy. Data fusion could overcome the problems of single satellite products, such as the missing data problem when clouds contaminate the scene or the instrument malfunctions, and can combine the advantages of difference data sources. MODIS provides a long time-period coverage of moderate resolution data (from 2000 to present). MISR has its distinctive multi-angular information, and MERIS data have good smooth seasonality curves and are close to in situ measurements (Gobron et al., 2006). The fusion results from multiple data sets can provide continuous spatial and temporal coverage. The uncertainty of integrated data is expected to be lower than the uncertainties of individual products if the correct model is used and the statistics of the errors reflects the level of actual noise in the data accurately.

Various data fusion methods have been developed, such as optimal interpolation (OI), Markov random field method, multiple-resolution tree (MRT), empirical orthogonal function, and hierarchical Bayesian model (Chou, 1991; Gandin, 1965; He et al., 2014; Preisendorfer, 1988; Wang and Liang, 2011). OI estimates the observation-to-background error variance for the noise. It takes irregular inputs and employs spatiotemporal covariance to interpolate variables at non-measured points and reduce errors at measured points. The method is called “optimal”, because it yields a linear estimate with the least expected error when the estimated noise accurately reflects the level of actual noise in the data (Zubko et al., 2010). The disadvantage of OI is that it does not handle large volumes of data well. OI requires the inversion of the covariance matrix to consider the contributions from adjacent spatiotemporal observations, which can be very time consuming when applying it at the regional to global scales. One possible solution to improve computational efficiency at the

regional to global scales is to calculate the weights of the observations empirically instead of optimally inverting the covariance matrix (Fang et al., 2008). Because of its advantage of simplicity and optimal nature, OI is chosen to integrate FAPAR values from different sources at the site scale (Gu et al., 2006).

Another popular method for image analysis is the Markov random field method, which provides a rich structure for multidimensional modeling; however, it is still computationally intensive. Chou et al. (1994) and Fieguth et al. (1995) introduced a recursive estimator consisting of a multiscale Kalman filter and a smoother over a Markov tree data structure that accommodates multiple observations with differing resolutions. At each node in the tree, the multiple resolution tree method optimally blends the available observations with respect to the least mean squared error according to the Kalman gain and the error characteristics of each sensor type (Jhee et al., 2013). The two step Kalman filtering and smoothing method is referred as multiple-resolution tree (MRT), which considers data continuity at multiple scales and generates multi-scale data simultaneously and efficiently. The original MRT fills the void regions with the nearest estimated values from a coarser scale, resulting in a blocky effect. An overlapping multiple-resolution tree method is utilized in the Kalman smoothing process in this study to reduce the blocky effect.

1.4. Objectives and Flowcharts of the Study

Regarding the importance of FAPAR and its possible improvement methods, the questions to be addressed in this research are: What are the spatial and temporal patterns of existing individual FAPAR products? How accurate are they when

validated with field measurements? Can we improve the FAPAR accuracy by using a new algorithm or better input of parameters? Is it possible to obtain an integrated FAPAR from the original FAPAR values with highest accuracy and continuous spatial and temporal coverage? Correspondingly, the overall objective of this study is to assess and improve the estimation of FAPAR from multiple satellite data products to reduce its uncertainty as an input in ecosystem models. In particular, there are three specific objectives:

Objective 1: Assessing existing FAPAR products

Current FAPAR satellite products, including MODIS, MISR, SeaWiFS, GEOV1, and MERIS FAPAR will be assessed in the study considering their availability and close resolutions to each other. There are only a few studies attempting to intercompare results among available FAPAR datasets, and even fewer validation studies with field measurements. An intercomparison among all of these products will generate an extensive evaluation of their accuracy for better usage. The in situ measurements from some experiments, e.g. Ameriflux and VAlidation of Land European Remote sensing Instruments Sites (VALERI), are used as validation data for product evaluation.

Objective 2: Developing a new RT model for FAPAR estimation

The accuracy of satellite FAPAR products directly influences the estimation of ecosystem productivity and carbon stocks. The targeted accuracy of FAPAR products is 10%, or 0.05, for many applications; however, most of the current FAPAR products have not yet fulfilled the accuracy requirement, and further improvements

are needed. This study improves FAPAR accuracy through developing new FAPAR retrieval models suitable for different land cover types, and through simultaneous improvement of the accuracy of model parameters such as LAI and soil background and leaf canopy albedos.

Objective 3: Developing FAPAR fusion schemes

Data fusion could overcome the problem of single satellite products, e.g., the missing data when the scene is contaminated by clouds or the malfunctioning instruments. It will combine the advantages of difference sources of data. MODIS promises long time coverage from 2000 to present. MISR has its distinctive multi-angular information, and MERIS data have a good seasonality curve and are close to field measurement (Gobron et al., 2008). The fusion results from these data are expected to have continuous spatial and temporal coverage. The precision of integrated data is the sum of the precisions of individual products if the statistics of the errors reflects exactly the level of actual noise in the data. The optimal interpolation (OI) method is chosen to integrate FAPAR values at the site scale. The overlapping multiple-resolution tree (MRT) is used to integrate data across multiple scales. Although the two methods have been applied to remote sensing, they have not been applied to integrate FAPAR products. This study focuses on application of the data fusion methods on FAPAR products at both the temporal and spatial domains.

The flowcharts to achieve the three objectives are summarized in Fig. 1-1. Chapter 2 intercompares MODIS, MISR, MERIS, SeaWiFS, and GEOV1 FAPAR products and validates them with in situ measurements (a). Chapter 3 presents an RT model to

retrieve FAPAR from multiple surface reflectance data including MODIS, Landsat, and MISR reflectance data (b). Finally, the FAPAR values from MODIS, MISR, and MERIS products are integrated temporally together using OI technique. The estimated FAPAR from Landsat, MODIS, and MISR data at several scales are integrated spatially through overlapping MRT algorithm (c). The quality controlled FAPAR from objective 1 and the estimated FAPAR from objective 2 serve as input data for objective 3 (d). The study domain for all three objectives contains 28 sites distributed globally as indicated in (a). The FAPAR products, estimations and integrations are intercompared and validated with field measurements at these sites.

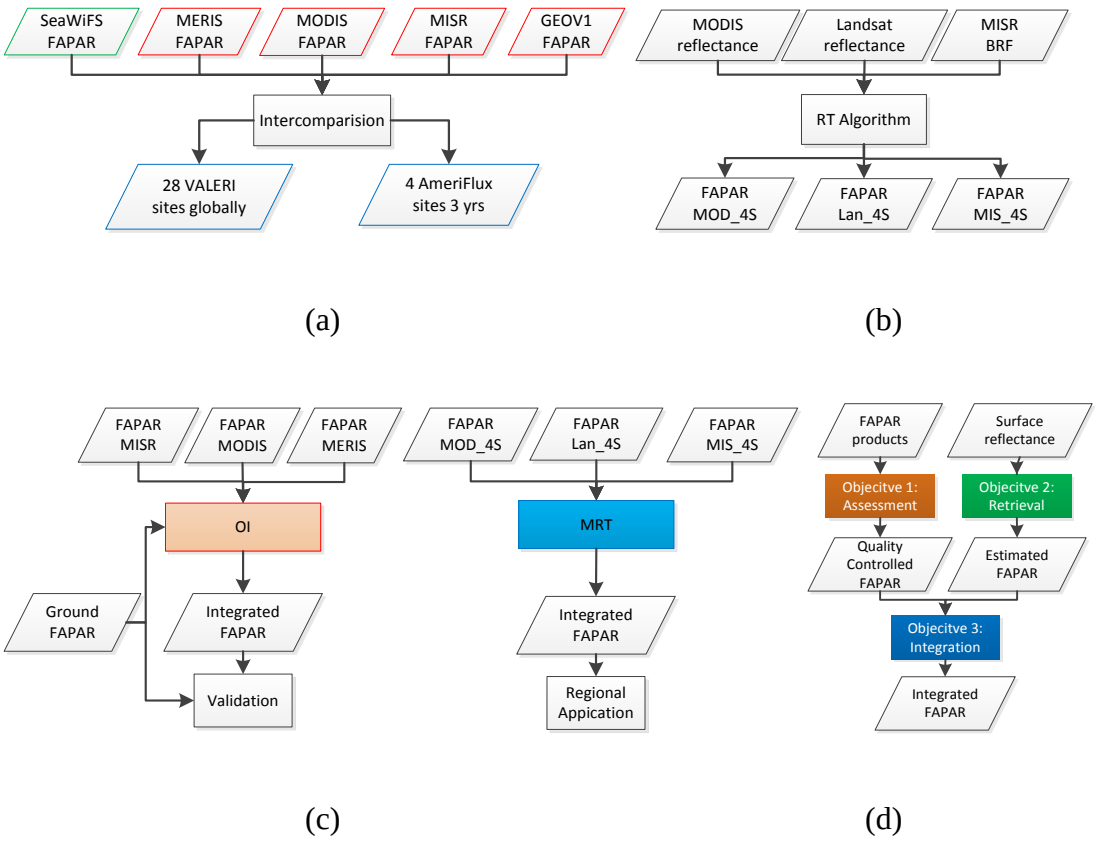

Fig. 1-1 Flowcharts of the study. (a) Objective 1: Assessment of existing products; (b) Objective 2: Developing a new RT model for FAPAR estimation; (c) Objective 3: Developing data fusion schemes; (d) The relationships among the three objectives.

Chapter 2 Assessment of five global satellite products of FAPAR

In this chapter, five global FAPAR products, namely MODIS, MISR, MERIS, SeaWiFS, and GEOV1 were intercompared over different land covers and directly validated with ground measurements at VAlidation of Land European Remote sensing Instruments (VALERI) and AmeriFlux sites. The remainder of this chapter is organized as follows. Section 2.1 presents the satellite FAPAR products and the validation data as well as the data processing and measurement methods. Section 2.2 intercompares FAPAR products globally and over different land cover types. Section 2.3 directly validates the FAPAR products with ground measurements. The findings are discussed Section 2.4.

2.1. Data and Methods

The data used in this chapter include satellite and in-situ FAPAR measurements. Satellite products include MISR, MODIS, SeaWiFS, MERIS, and GEOV1 FAPAR products. The FAPAR validation data are collected from two groups of experimental sites: VAlidation of Land European Remote sensing Instruments (VALERI, WWW1) and AmeriFlux (WWW2). The VALERI sites are widely distributed around the world and useful for spatial validation over different land covers (Camacho et al., 2013; Weiss et al., 2007). Three years of measurements at AmeriFlux sites are intended for validating FAPAR products for a long period of time in consideration of their continuous measurements of FAPAR. The land covers of the 27 VALERI and AmeriFlux sites include 9 forests (1 of Ameriflux and 8 of VALERI), 11 crops (3 of

Ameriflux and 8 of VALERI), 6 grass sites (of VALERI), and 1 shrubland site (of VALERI). Their distributions are shown in Fig. 2-1. The geolocation and land cover information of the AmeriFlux and the VALERI sites are listed in Table 2-1 for reference.

Four components are measured to compute FAPAR at AmeriFlux sites, including incoming and outgoing solar flux and flux from and to the ground. Incoming (outgoing) solar flux is measured with Li-Cor point quantum sensors aimed upward (downward), and placed at approximately 6 m above the ground. Flux transmitted through the canopy to the ground is measured with Li-Cor line quantum sensors placed at approximately 2 cm above the ground, pointing upward. Flux reflected by the ground is measured with Li-Cor line quantum sensors placed approximately 12 cm above the ground, pointing downward (Hanan et al., 2002). Hourly FAPAR is calculated as the ratio of absorbed photosynthetically active radiation and incoming solar flux. All the daytime radiation values are computed by integrating the hourly measurements during a day when incoming solar flux exceeded 1$\mu mol/m^2/s$, and daily FAPAR is then calculated. Digital hemispherical photos are used to calculate FAPAR at VALERI sites, which corresponds to the fraction of intercepted PAR. High spatial resolution remote sensing data are used as a bridge to obtain the FAPAR values in the medium resolution pixels. The differences in the interception and the absorptions are small (less than 5%), which are taken into account by adding error bar on the in-situ data in this study considering the limited FAPAR ground-based data (Serbin et al., 2013).

Satellite FAPAR products have some differences in the definition of their products in terms of the whole canopy or green leaves, direct radiation only or not, and the imaging time. The MISR FAPAR product is the total FAPAR at 10:30 am, considering both direct and diffuse radiation absorbed by the whole canopy. The MODIS FAPAR considers only direct radiation, which may result in a smaller value than the MISR FAPAR product. The imaging time of the SeaWiFS sensor is approximately 12:05 pm local time, and its FAPAR product corresponds to the black sky FAPAR (direct radiation only) by green elements. Similarly, the MERIS FAPAR product corresponds to the black sky FAPAR by green elements at 10 am local time. The GEOV1 FAPAR product corresponds to the instantaneous black-sky FAPAR by green parts around 10:15 am local time. The SeaWiFS, MERIS, and GEOV1 FAPAR products take into account only the absorption by green elements, which may result in lower FAPAR values than the MISR and MODIS FAPAR products, which include the absorption of both green and non-green elements. Overall, most of the satellite FAPAR products correspond to the instantaneous black-sky FAPAR around 10:15 am which is a close approximation of the daily integrated FAPAR value collected at AmeriFlux and VALERI sites so that the validation of satellite FAPAR products using these ground-based measurements would be reasonable.

The spatial and temporal resolutions and the temporal coverage information of the satellite FAPAR products used in this paper, as well as their retrieval algorithms, are listed in Table 2-2. The spatial resolutions of the FAPAR products vary from 1 km to 0.5 °, and the temporal resolutions vary from daily to 1 month. Spatial aggregation and temporal interpolation are necessary to intercompare the values across multiple

scales. The MODIS and GEOV1 FAPAR products are preprocessed to be at the same temporal and spatial resolution than other products. The four 8-day MODIS FAPAR images are composited to monthly product from the average value of the highest quality data, in consideration of the quality of the output data and the small number of 8-day input data in a month. Average value is used because of the small number of 8-day valid observations in a month (maximum of 4). In consideration of the quality of the output, we generate the average value from the highest quality data in a month. The monthly 1km product is resampled to 1/112° using nearest neighbor technique and then aggregated to 0.5 °spatial resolution using spatial average. Similarly, the 30-day composite GEOV1 FAPAR product with the highest quality is spatially aggregated to 0.5 °spatial resolution.

The different spatial scales between the FAPAR product pixels and the in-situ measurements can induce the scaling effect of FAPAR, which happens when the surface is heterogeneous and the retrieval algorithm is nonlinear (Tao et al., 2009; Xu et al., 2009). Because of the scale difference, the validation results at more homogeneous sites are expected to have a higher FAPAR accuracy. We evaluate the heterogeneity around the validation sites by calculating the standard deviation divided by the mean of the simple ratio between near infrared and red bands of the Landsat data in the 1 × 1 km extent around the sites corresponding to the most common resolution of the satellite FAPAR products used for direct validation. The FAPAR accuracy at different sites is analyzed and the impact of site heterogeneity on the FAPAR product accuracy is explored.

Table 2-1 The AmeriFlux and VALERI experimental sites used in this study.

Site	State, Country	Latitude (°)	Longitude (°)	Land Cover
Mead Irrigated	Nebraska, US	41.1651	−96.4766	crops
Mead Irrigated Rotation	Nebraska, US	41.1649	−96.4701	crops
Mead Rainfed	Nebraska, US	41.1797	−96.4396	crops
Bartlett	New Hampshire, US	44.0646	−71.2881	deciduous broadleaf forests
Laprida	Argentina	−36.9904	−60.5527	grass
Camerons	Australia	−32.5983	116.2542	evergreen broadleaf forests
Gnangara	Australia	−31.5339	115.8824	deciduous broadleaf forests
Sonian forest	Belgium	50.7682	4.4111	needleleaf forests
Donga	Benin	9.7701	1.7784	grass
Turco	Bolivia	−18.2395	−68.1933	shrubland
Larose	Canada	45.3805	−75.2170	needleleaf forests
Concepción	Chile	−37.4672	−73.4704	deciduous needleleaf

				forests
Zhang Bei	China	41.2787	114.6878	grass
Les Alpilles	France	43.8104	4.7146	crops
Larzac	France	43.9375	3.1230	grass
Nezer	France	44.5680	−1.0382	needleleaf forests
Plan-de-Dieu	France	44.1987	4.9481	crops
Puéchabon	France	43.7246	3.6519	mediterranean forests
Sud-Ouest	France	43.5063	1.2375	crops
Counami	French Guiana	5.3471	−53.2378	evergreen broadleaf forests
Demmin	Germany	53.8921	13.2072	crops
Gilching	Germany	48.0819	11.3205	crops
Hombori	Mali	15.3310	−1.4751	grass
Haouz	Morocco	31.6592	−7.6003	crops
Wankama	Niger	13.6450	2.6353	grass
Fundulea	Romania	44.4061	26.5831	crops
Barrax	Spain	39.0570	−2.1042	crops

The first four sites are AmeriFlux sites, others are VALERI sites.

Table 2-2 The characteristics of the satellite FAPAR products used in this study.

FAPAR Product	Temporal coverage	Temporal resolution	Spatial resolution	Projection	Algorithm
MODIS MOD15 (C5) (WWW3)	Feb 2000–	8 days	1 km	Sinusoidal	Look up table method built on 3D stochastic radiative transfer model for different biomes (Myneni et al., 2002).
MISR (L3/L2) (WWW4)	Feb 2000–	1 month / Equator: 9 days, Polar: 2 days	0.5 ?1 km	Plate-carr ée (geographic) / Space Oblique Mercator	Radiative transfer (RT) model with inputs of LAI and soil reflectance without assumptions on biomes (Knyazikhin et al., 1998a).
GEOV1 (WWW5)	Dec 1998–	10 days	l⁄112°	Plate-carr ée	Neural network to relate the fused products to the top of canopy SPOT/VEGETATION reflectance (Baret et al., 2013).
MERIS (L3/L2) (WWW6	Apr 2002–	1 month / daily	0.5 ?1 km	Plate-carr ée / sinusoidal	Polynomial formula based on 1D RT model (Gobron et al., 1999).

)					
SeaWiFS (L3/L2) (WWW7)	Sep 1997–	1 month / daily	0.5 ?1 km	Plate-carr ée / sinusoidal	Polynomial formula based on 1D RT model (Gobron et al., 2006; Gobron et al., 2000).

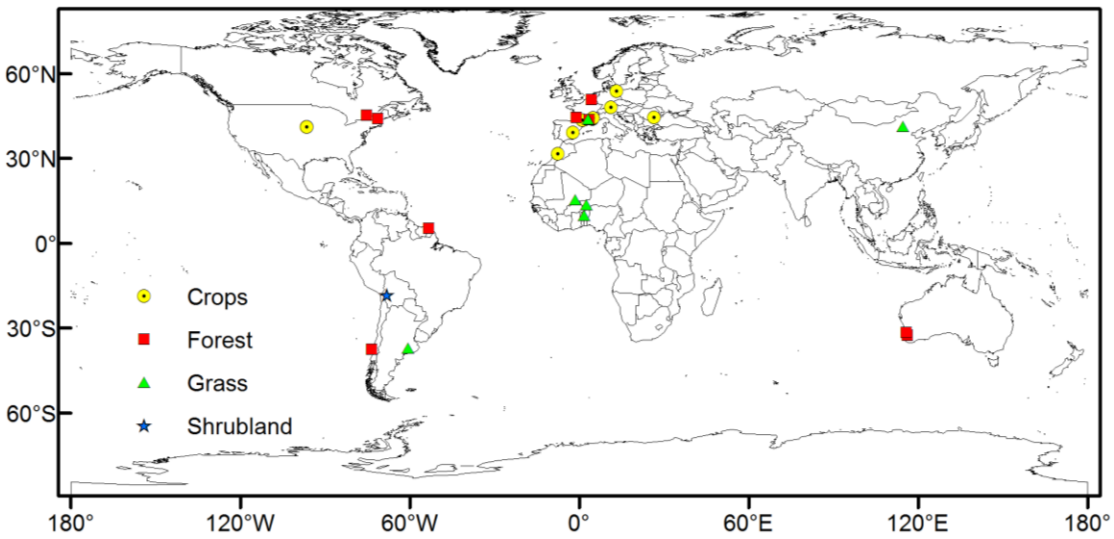

Fig. 2-1 The distribution of the 27 VALERI and AmeriFlux sites. There are 3 AmeriFlux and 3 VALERI sites close to each other, which may not be distinguishable from each other at a global scale here.

2.2. Intercomparison of Satellite FAPAR Products

The MODIS, MERIS, MISR, SeaWiFS, and GEOV1 satellite FAPAR products are intercompared globally and over different land cover types in a one year period. Specifically, the spatial and seasonal distributions of the five satellite FAPAR products are intercompared globally in Section 2.2.1. The performances of the five

satellite FAPAR products over different land cover types are intercompared in Section 2.2.2.

2.2.1. Intercomparisons over the globe

The spatial distribution of the five global FAPAR products during the period July 2005–June 2006 is depicted in Fig. 2-2. The MODIS global FAPAR product generally agrees well with the MISR and GEOV1 FAPAR product, while the MERIS and SeaWiFS FAPAR products agree well with each other. However, the difference between the group of MODIS, MISR, and GEOV1 FAPAR products and the group of MERIS and SeaWiFS FAPAR products is large (>0.1). The results are expected and the primary reason is that both the SeaWiFS and the MERIS FAPAR products correspond to absorbed fluxes for green leaf single scattering whereas the MODIS and MISR FAPAR products are based on a priori knowledge of leaf single scattering for each biome. The GEOV1 FAPAR correspond to a fused products which includes MODIS ones.

The seasonal distribution of the five preprocessed 0.5 °spatial resolution FAPAR products over the entire globe and the Northern and Southern Hemispheres with the same number of pixels are depicted in the panels of Fig. 2-3. The MODIS FAPAR values remain relatively stable globally from December to March, then increase at an accelerating rate from April to July, and finally decrease from August to the lowest values in December. The trend in the Northern Hemisphere is slightly different, where FAPAR remains relatively stable from January (instead of December globally) to March, then increases from April to July, and finally decreases from August to

January (instead of December globally, 1 month longer). The reason is an increase in vegetation FAPAR values from December in the Southern Hemisphere, so that global FAPAR would drop to the lowest value in December even if northern hemispheric FAPAR drops to the lowest value in January. The MERIS, MISR, SeaWiFS, and GEOV1 global FAPAR values have similar trends as the MODIS global FAPAR values. Therefore, satellite FAPAR products agree well both globally and in the Northern Hemisphere in terms of trends. The differences of the mean values of the MODIS, MISR, and GEOV1 FAPAR products at the global scale are very small (<0.05 generally). The difference of the standard deviations of MODIS and MISR are less than 0.02. The mean values of the MERIS and SeaWiFS FAPAR products differ within 0.05 and the standard deviations differ within 0.015. However, the MODIS, MISR, and GEOV1 global FAPAR values are 0.05–0.1 higher than the average of the five products; whereas the MERIS and SeaWiFS global FAPAR values are 0.05–0.1 lower than the average in terms of magnitudes. Absolute FAPAR values are on average in decreasing order from MISR to MODIS to GEOV1 to SeaWiFS and MERIS (McCallum et al., 2010).

The difference between the MODIS, MISR, and GEOV1 FAPAR products become greater in other seasons than in the vegetation growing season, with the mean values differing by approximately 0.05. The differences between the mean of the MERIS and SeaWiFS FAPAR products remain stable and do not depend on the vegetation growing season. The difference between the group of MODIS, MISR, and GEOV1 FAPAR products and the group of MERIS and SeaWiFS FAPAR products becomes greater in other seasons (~0.16). The differences in the standard deviations between 2

months were within 0.02 for any of the five global FAPAR products. Therefore, the standard deviation of global FAPAR is almost independent of the month for these FAPAR products.

Compared with the FAPAR trends in the Northern Hemisphere, opposite situations are found in the FAPAR trends in the Southern Hemisphere. The MODIS and GEOV1 southern hemispheric FAPAR remain relatively stable from August to November, then increase to the highest values in May, and finally drop to the lowest values in November. The MISR southern hemispheric FAPAR has similar trend as the MODIS and GEOV1 southern hemispheric one, except that it drops to the lowest values near September instead of November. The MERIS southern hemispheric FAPAR is slightly different from the MODIS and MISR one. It remains relatively stable from July to September, then increases to the highest values in February, and finally drops to the lowest values near August (3 months variation from MODIS). The SeaWiFS southern hemispheric FAPAR remains relatively stable from July to September, then increases to the highest values in April, and finally drops to the lowest values in September (same as MISR). Overall, southern hemispheric FAPAR remains relatively stable from August to November, then increases to the highest values in April or May, and finally drops to the lowest values between September and November. The increased disparity among products in the Southern Hemisphere is likely a result of fewer vegetation samples there, which is explored in detail for different land covers in Section 2.2.2.

The quality flags of MODIS FAPAR with non-fill values are analyzed to select maps in high quality month for further comparisons. The statistics of MODIS Collection 5

FAPAR quality control flags are depicted globally and in the Northern and Southern Hemispheres (Fig. 2-4). The percentage of the main algorithm retrievals increases in the middle of the growing season and reaches the highest value in September. The percentage of backup retrievals due to bad geometry increases in the winter as expected because of the larger solar zenith angle. This kind of backup retrieval related to bad geometry lasts 6 months, from October to March, both globally and in the Northern Hemisphere and approximately 3 months, from May to July, in the Southern Hemisphere. Overall, the analysis on the MODIS quality flags shows that the quality of satellite FAPAR products is better in the vegetation growing season than other season.

The difference maps between products in July was generated considering the good quality of FAPAR products in the vegetation growing season, and the results are shown in Fig. 2-5. The sea/land mask is applied and only pixels with high quality values from all of the five satellite FAPAR products are included in the difference maps. The MISR FAPAR product exhibits some higher FAPAR values than the MERIS and SeaWiFS FAPAR products at high latitudes, and some slightly lower FAPAR values in the tropical forests near the equator. The difference between the MERIS and SeaWiFS FAPAR products is very small, with a few pixels located along the boundaries of continents. The difference between the MISR and MODIS FAPAR products is quite small as well, with only a few scatters in the boreal forests of Asia and North America. The MISR and MODIS FAPAR products are close to the GEOV1 FAPAR product, except some boundary regions. However, the MODIS FAPAR values are apparently higher than the MERIS and SeaWiFS FAPAR values

over the boreal forests and savannahs. The GEOV1 FAPAR product is consistently higher than the MERIS and SeaWiFS FAPAR products over the tropical and boreal forests.

The five global FAPAR datasets were averaged per grid cell and then subtracted from each dataset to obtain the difference to the mean maps (Fig. 2-6). The MODIS, MISR, and GEOV1 FAPAR products have larger values than the average in the boreal and tropical forests and grasslands in the Northern Hemisphere. The GEOV1 FAPAR product is closest to the average of all the products. The MERIS and SeaWiFS FAPAR products have apparently lower than the average values in the forests, savannahs and grasslands. The differences to the mean maps are averaged across different latitudes (Fig. 2-7). Their differences are smaller at low and high latitudes but are larger at middle latitudes, especially in the southern hemisphere. The possible reason is the saturation of FAPAR values in the tropical forests and the scarcity of vegetation in the high latitudes so that the differences are smaller in these regions.

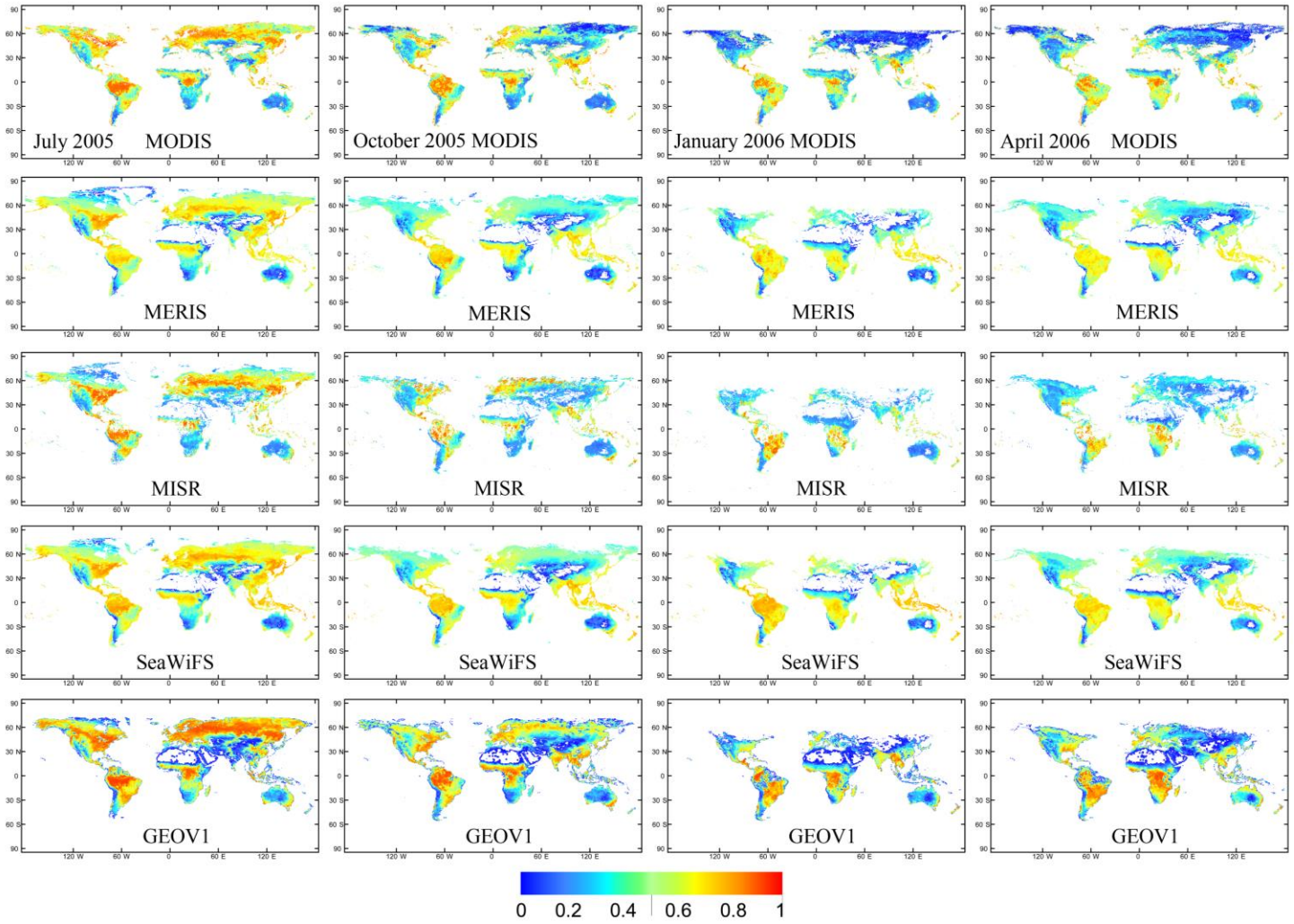

Fig. 2-2 The MODIS, MERIS, MISR, SeaWiFS, and GEOV1 global FAPAR distributions in Plate-carr é projection during the period July 2005–June 2006 (every 3 months). Note the agreements among the MODIS, MISR, and GEOV1 FAPAR products and between the MERIS and SeaWiFS FAPAR products. However, the MODIS, MISR, and GEOV1 FAPAR values were consistently higher than the MERIS and SeaWiFS FAPAR values.

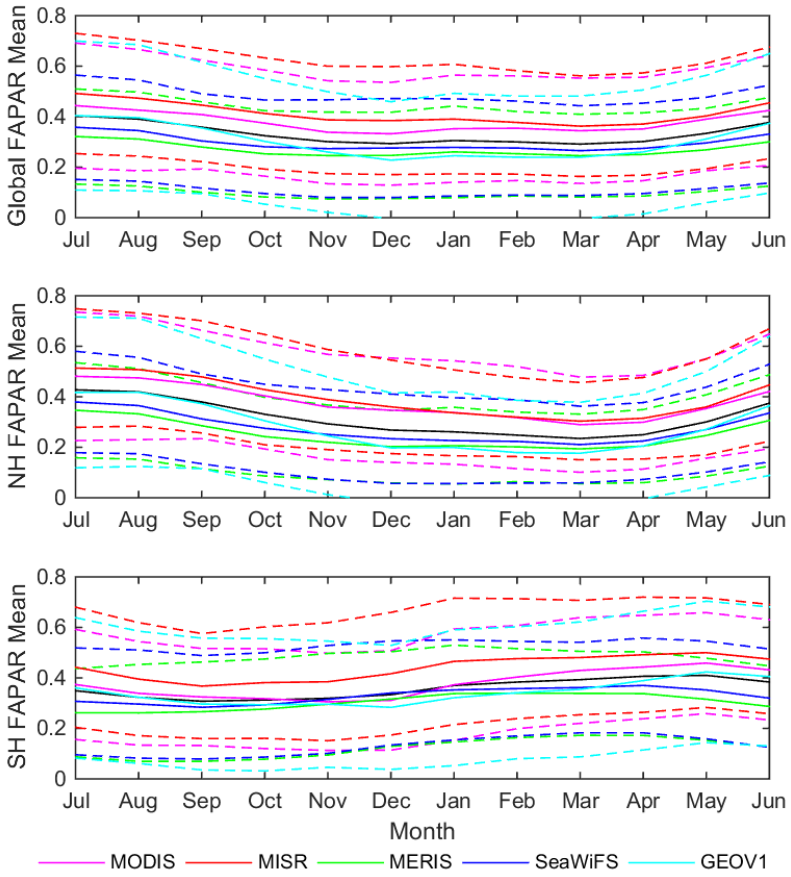

Fig. 2-3 The global, northern hemispheric, and southern hemispheric mean of quality controlled MODIS, MISR, MERIS, SeaWiFS, and GEOV1 FAPAR products during the period July 2005–June 2006. The black curve is all five products mean. The dashed curves correspond to the mean ± standard deviation of each product.

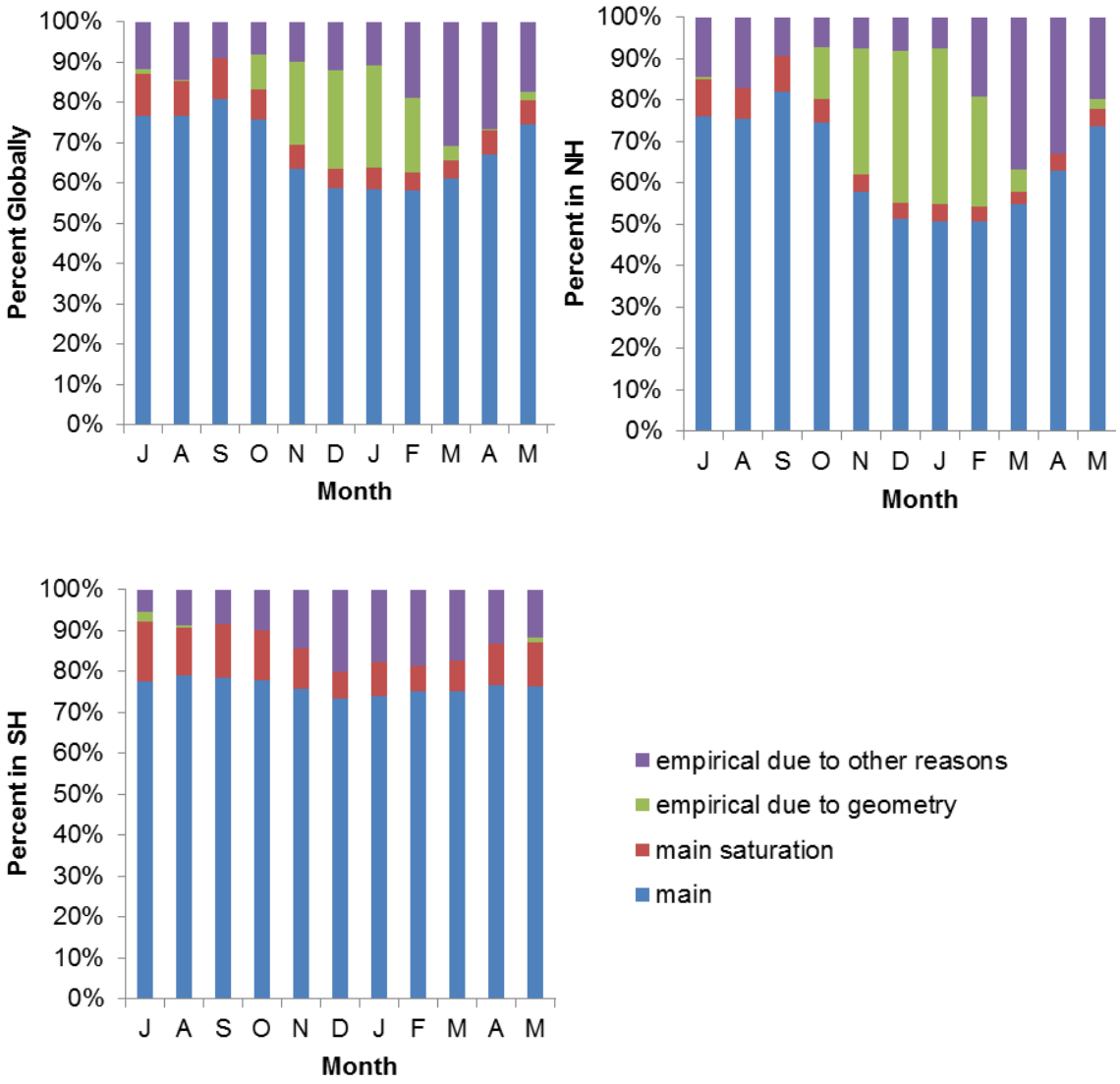

Fig. 2-4 MODIS collection 5 FAPAR QC statistics globally, in the Northern Hemisphere, and the Southern Hemisphere: the percentage of main algorithm retrievals (blue), the percentage of main algorithm under conditions of saturation (red), the percentage of backup (i.e. NDVI-based) retrievals associated with bad geometry (green), the percentage of pixels using the backup algorithm due to reasons other than geometry (purple). Note the overall increase in high quality (main algorithm) retrievals during the middle of the growing season.

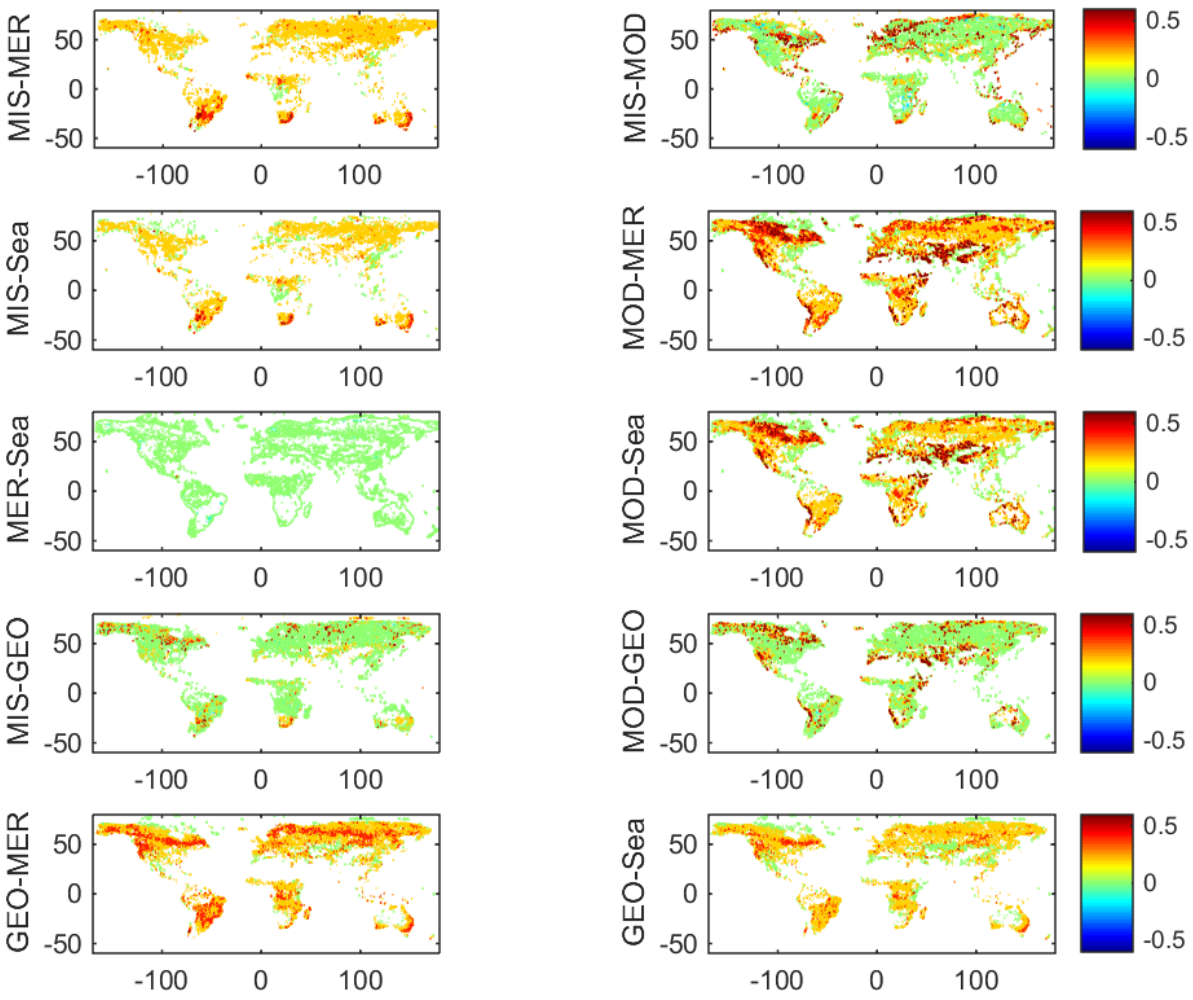

Fig. 2-5 Global FAPAR difference maps between the MODIS, MISR, GEOV1, MERIS and SeaWiFS products in July 2005 (MIS: MISR, MER: MERIS, MOD: MODIS, Sea: SeaWiFS, Geo: GEOV1).

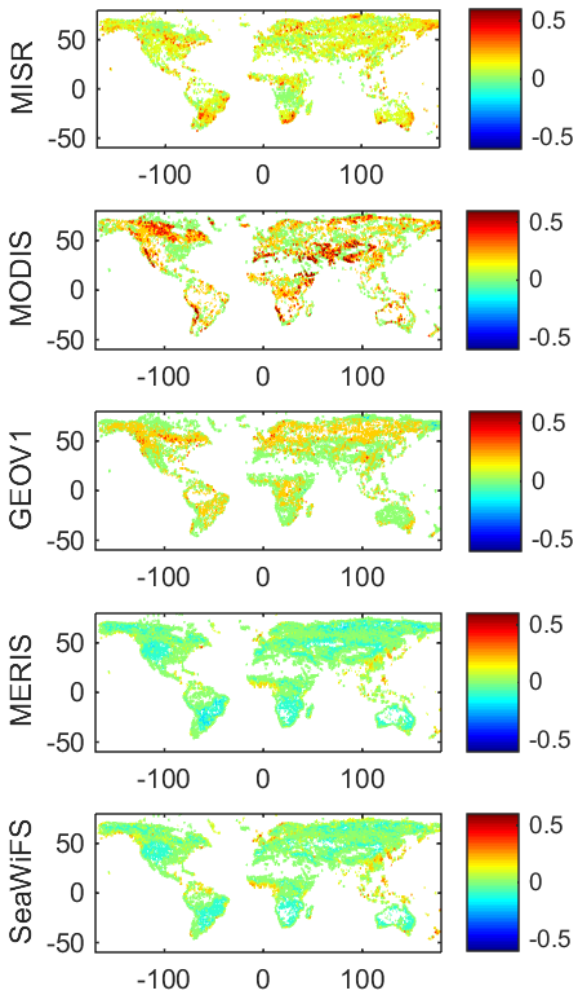

Fig. 2-6 Maps of the five global FAPAR datasets in July 2005, with the mean of all five products per grid-cell subtracted from each dataset.

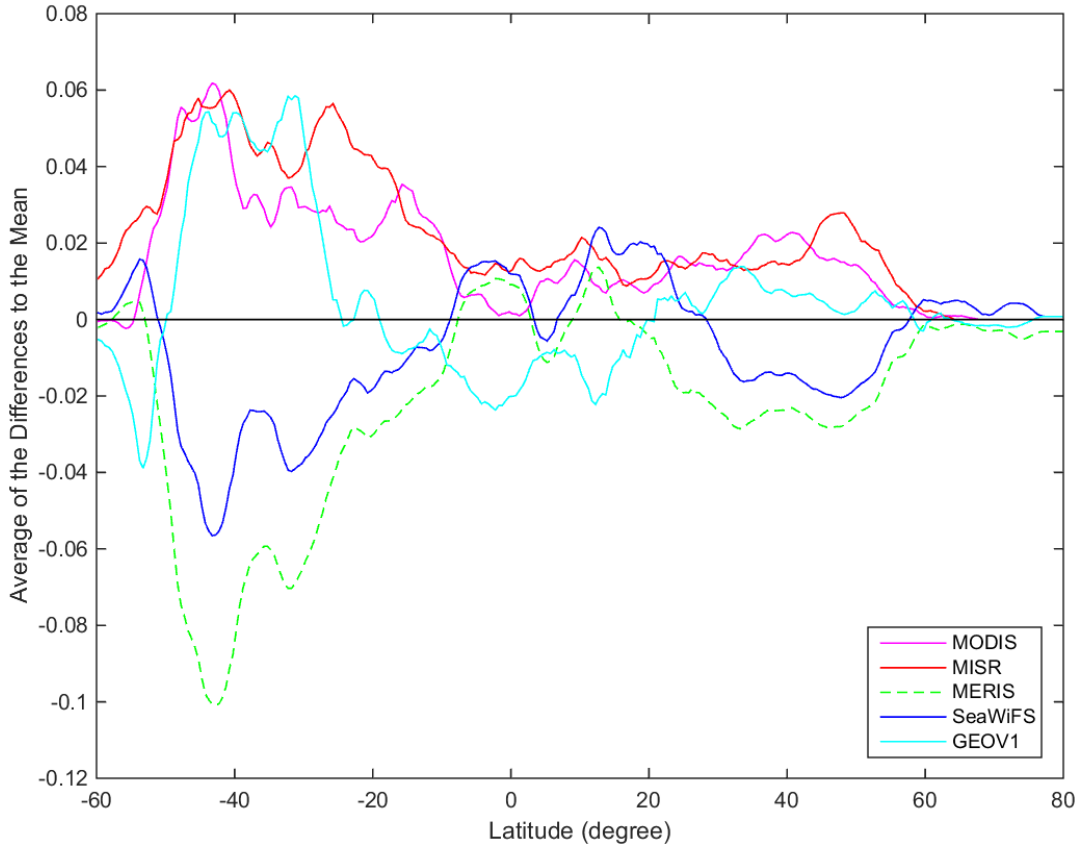

Fig. 2-7 The average of the difference to the mean of the five products at different latitudes in July 2005. The black line is for reference.

2.2.2. Intercomparisons over different land cover types

The MODIS global land cover map (MCD12) during the period July 2005–June 2006 is depicted in Fig. 2-8. The vegetated areas are classified by use of the MODIS-derived LAI/FAPAR scheme into eight land cover types: broadleaf evergreen forest, broadleaf deciduous forest, needleleaf evergreen forest, needleleaf deciduous forest, crop, grass, savannah, and shrubland (Myneni et al., 2002). The MCD12 land cover classification product was resampled into 0.5 °using the mode resampling method by selecting the value which appears most often of all the sampled points. Most of the

vegetated areas are located in the Northern Hemisphere. The only exception is the broadleaf evergreen forests, the majority of which are located in the Southern Hemisphere, including the northwest part of South America, part of Central Africa, and the southern part of Southeast Asia.

The histograms of the MODIS, MERIS, MISR, SeaWiFS, and GEOV1 FAPAR products over the entire globe, the Northern Hemisphere, and the Southern Hemisphere are depicted in Fig. 2-9, where the blue bars denote the number of pixels in the Northern Hemisphere, and the red bars denote the number of pixels in the Southern Hemisphere. The MODIS, the MISR, and the GEOV1 FAPAR agree well with each other over different land cover types, and so do the MERIS and the SeaWiFS FAPAR. The MODIS, MISR, and GEOV1 FAPAR are consistently higher than the MERIS and SeaWiFS FAPAR because the former ones detect much more pixels with FAPAR values over 0.8 than the latter, especially over tropical forests. The differences in the magnitudes could be attributed to the different composite algorithms. Both global MERIS and SeaWiFS monthly products correspond to median values in a month instead of average values as the MODIS, MISR, and GEOV1 FAPAR products. Consequently, there are fewer high FAPAR values in the MERIS and SeaWiFS FAPAR products than in other products. Absolute FAPAR values are on average in decreasing order from MISR to MODIS to GEOV1 to SeaWiFS and MERIS over almost all land cover types except needleleaf forests. The MODIS FAPAR is higher than the MISR FAPAR over needleleaf forests, because more pixels with high FAPAR values are detected over needleleaf forests in the MODIS FAPAR product than in the MISR FAPAR product. The GEOV1 FAPAR

product is very close to the MODIS FAPAR product, with slight deviations over broadleaf evergreen forests. Regarding the differences of the mean of the products over the Northern and Southern Hemispheres, the mean FAPAR is higher in the Northern Hemisphere than in the Southern Hemisphere over most of the land cover types except broadleaf evergreen forest for the five products during the northern hemispheric vegetation growing season. The mean FAPAR over broadleaf evergreen forest in the Southern Hemisphere is slightly higher (~0.02) than in the Northern Hemisphere. The mean of all five products is averaged globally and in the Northern and Southern Hemispheres during the period July 2005–June 2006 to show their seasonal patterns at the three scales (Fig. 2-10). The southern hemispheric FAPAR is constantly higher than the northern hemispheric FAPAR over broadleaf evergreen forests, regardless of season.

The trend of northern hemispheric FAPAR was similar to that of global FAPAR, with slight difference in the magnitudes (Fig. 2-10). The explanation is that the majority of the land cover is located in the Northern Hemisphere, resulting in the dominant influence of northern hemispheric FAPAR on global FAPAR. The exceptions are the FAPAR over savannah and broadleaf evergreen forest land covers. The global FAPAR mean over savannah remains almost constant throughout the year, but the northern hemispheric FAPAR mean is a sine curve, with the highest value in September and the lowest value between February and March. There is an opposite trend in the Southern Hemisphere, and the two trends cancel each other out globally. The global FAPAR mean over broadleaf evergreen forest is stabilized throughout the year, but the northern hemispheric FAPAR is a sine curve. In this case, the curve of

the global FAPAR mean is similar to the curve in the Southern Hemisphere, because the majority of broadleaf evergreen forests are located in the Southern Hemisphere as noted.

Compared with the trends of the northern hemispheric FAPAR mean, opposite trends are found in the southern hemispheric FAPAR mean. The opposite relations are very apparent globally, over crop, savannah, grass, broadleaf deciduous forest, and needleleaf evergreen forest. The opposite relations are not apparent over shrubland and broadleaf evergreen forest, where the southern hemispheric FAPAR is stable throughout the year, but the northern hemispheric FAPAR mean has a parabolic shape over shrubland and a sine curve over broadleaf evergreen forest. The global FAPAR curve overlaps with the northern hemispheric FAPAR curve over needleleaf evergreen forests, provided that only a few needleleaf evergreen forests are in the Southern Hemisphere. Barely any needleleaf deciduous forests are in the Southern Hemisphere. Both the northern hemispheric and the global FAPAR mean have bowl-like shapes over needleleaf deciduous forests throughout the year.

The time series of the mean of the MISR, MODIS, GEOV1, SeaWiFS, and MERIS FAPAR products over different land cover types during the period July 2005–June 2006 are depicted in Fig. 2-11, with the mean of all five products subtracted from each dataset. The MODIS and MISR FAPAR products are approximately 0.05–0.1 higher than the average of the five products, and the MERIS and SeaWiFS FAPAR products are approximately 0.05–0.1 lower than the average of the five products. The GEOV1 FAPAR product has very small difference (< 0.05) to the mean over grass, shrubland, crop and savannah. The deviations to the mean for the five products

remain stable over grass, shrubland, crops, savannah, and broadleaf evergreen forests throughout the year. However, a different situation occurs over broadleaf deciduous forests, where the deviations are largest in October and smallest in June and July. The deviations of the five products from the average over needleleaf evergreen and needleleaf deciduous forests are largest in September and October, and gradually decrease to the lowest values in March. The GEOV1 FAPAR product has large fluctuations over needleleaf evergreen and needleleaf deciduous forests because of its strong seasonal pattern over the needleleaf forests with a standard deviation of 0.21, compared with standard deviations around 0.11 for other FAPAR products. In such case, it fluctuates both above and below the average line, although it has similar seasonality as other products as shown in Fig. 2-3. The MISR FAPAR product has a drop in the value over needleleaf deciduous forest in December because of no data. Overall, the differences between the products are consistent throughout the year over most of the land cover types, except over the forests. The possible reason can be traced to the different assumptions in the retrieval algorithms over forests and the large differences between green and total FAPAR products due to tree trunks and branches absorption (Pickett-Heaps et al., 2014). Interestingly, the differences between the products do not fluctuate much in broadleaf evergreen forests over time, because FAPAR values remain relatively stable all year long and therefore the differences between the products are small and consistent over broadleaf evergreen forests.

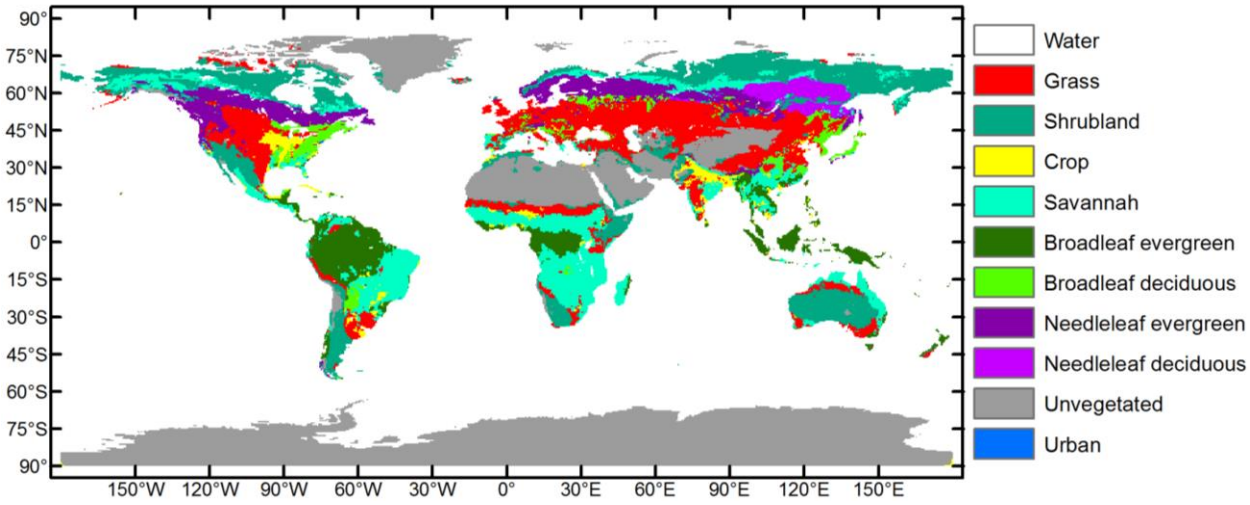

Fig. 2-8 The resampled MODIS global land cover map (MCD12) at 0.5 °during the period July 2005–June 2006. The vegetated areas are classified by use of the MODIS-derived LAI/FAPAR scheme into eight land cover types: broadleaf evergreen forest, broadleaf deciduous forest, needleleaf evergreen forest, needleleaf deciduous forest, crop, grass, savannah and shrubland. The map also includes the unvegetated, water, and urban area.

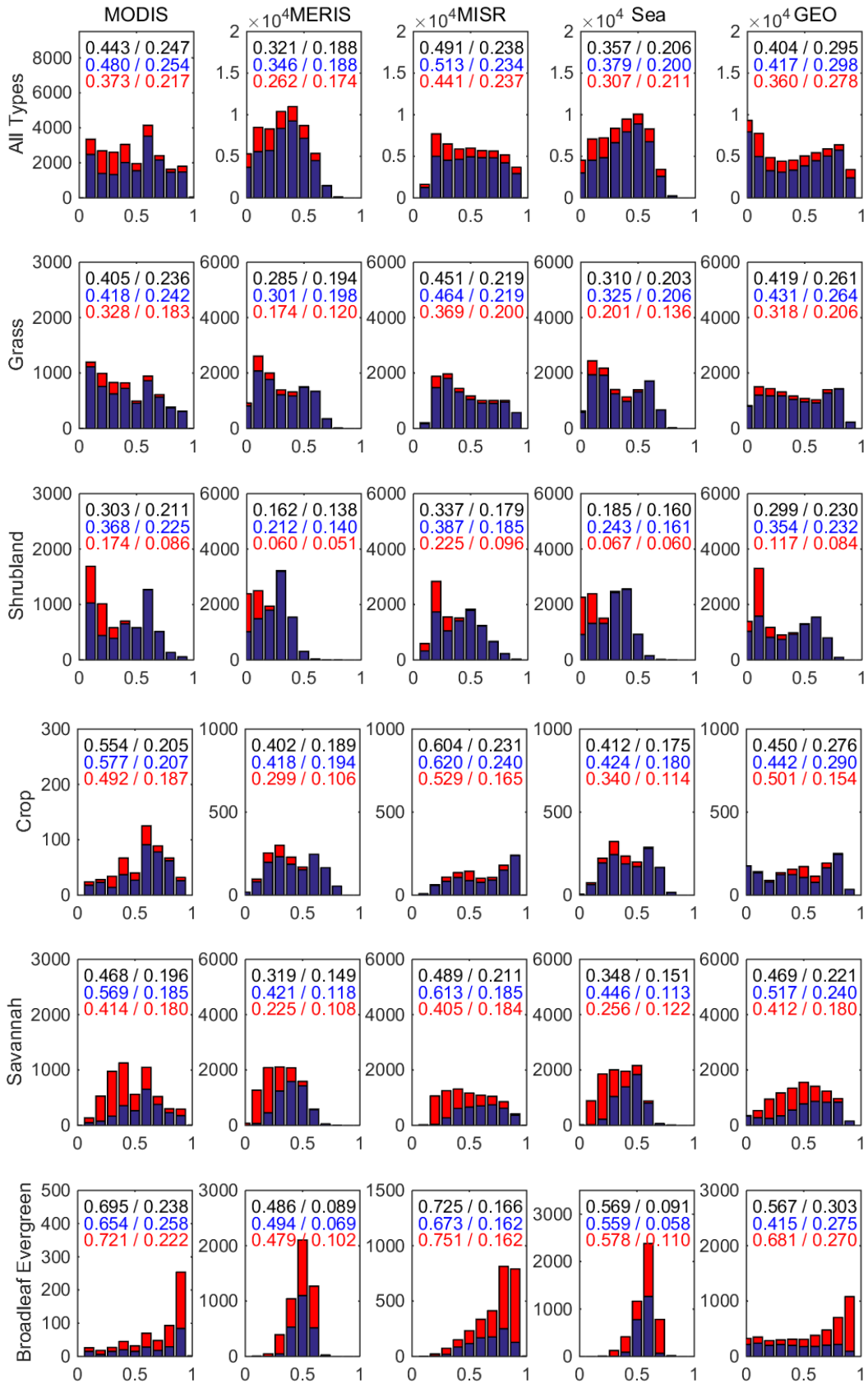
MODIS
×10^4MERIS
×10^4MISR
×10^4 Sea
×10^4 GEO
All Types
0.443 / 0.247
0.480 / 0.254
0.373 / 0.217
0.321 / 0.188
0.346 / 0.188
0.262 / 0.174
0.491 / 0.238
0.513 / 0.234
0.441 / 0.237
0.357 / 0.206
0.379 / 0.200
0.307 / 0.211
0.404 / 0.295
0.417 / 0.298
0.360 / 0.278
Grass
0.405 / 0.236
0.418 / 0.242
0.328 / 0.183
0.285 / 0.194
0.301 / 0.198
0.174 / 0.120
0.451 / 0.219
0.464 / 0.219
0.369 / 0.200
0.310 / 0.203
0.325 / 0.206
0.201 / 0.136
0.419 / 0.261
0.431 / 0.264
0.318 / 0.206
Shrubland
0.303 / 0.211
0.368 / 0.225
0.174 / 0.086
0.162 / 0.138
0.212 / 0.140
0.060 / 0.051
0.337 / 0.179
0.387 / 0.185
0.225 / 0.096
0.185 / 0.160
0.243 / 0.161
0.067 / 0.060
0.299 / 0.230
0.354 / 0.232
0.117 / 0.084
Crop
0.554 / 0.205
0.577 / 0.207
0.492 / 0.187
0.402 / 0.189
0.418 / 0.194
0.299 / 0.106
0.604 / 0.231
0.620 / 0.240
0.529 / 0.165
0.412 / 0.175
0.424 / 0.180
0.340 / 0.114
0.450 / 0.276
0.442 / 0.290
0.501 / 0.154
Savannah
0.468 / 0.196
0.569 / 0.185
0.414 / 0.180
0.319 / 0.149
0.421 / 0.118
0.225 / 0.108
0.489 / 0.211
0.613 / 0.185
0.405 / 0.184
0.348 / 0.151
0.446 / 0.113
0.256 / 0.122
0.469 / 0.221
0.517 / 0.240
0.412 / 0.180
Broadleaf Evergreen
0.695 / 0.238
0.654 / 0.258
0.721 / 0.222
0.486 / 0.089
0.494 / 0.069
0.479 / 0.102
0.725 / 0.166
0.673 / 0.162
0.751 / 0.162
0.569 / 0.091
0.559 / 0.058
0.578 / 0.110
0.567 / 0.303
0.415 / 0.275
0.681 / 0.270

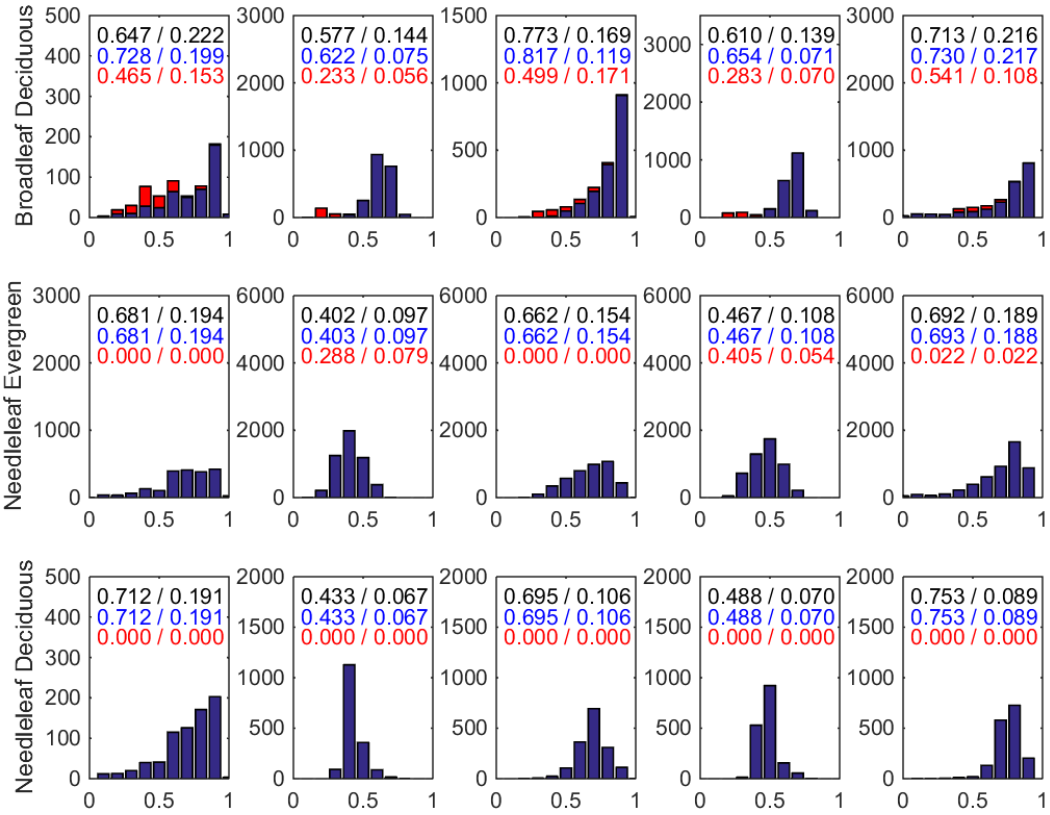

Fig. 2-9 Histograms of the quality controlled MODIS, the MERIS, the MISR, the SeaWiFS, and the GEOV1 FAPAR products over all or individual land cover types in the entire globe (black), the Northern Hemisphere (blue), and the Southern Hemisphere (red) in July 2005. The numbers are the mean and the standard deviations of FAPAR over the entire globe (black), the Northern Hemisphere (blue), and the Southern Hemisphere (red).

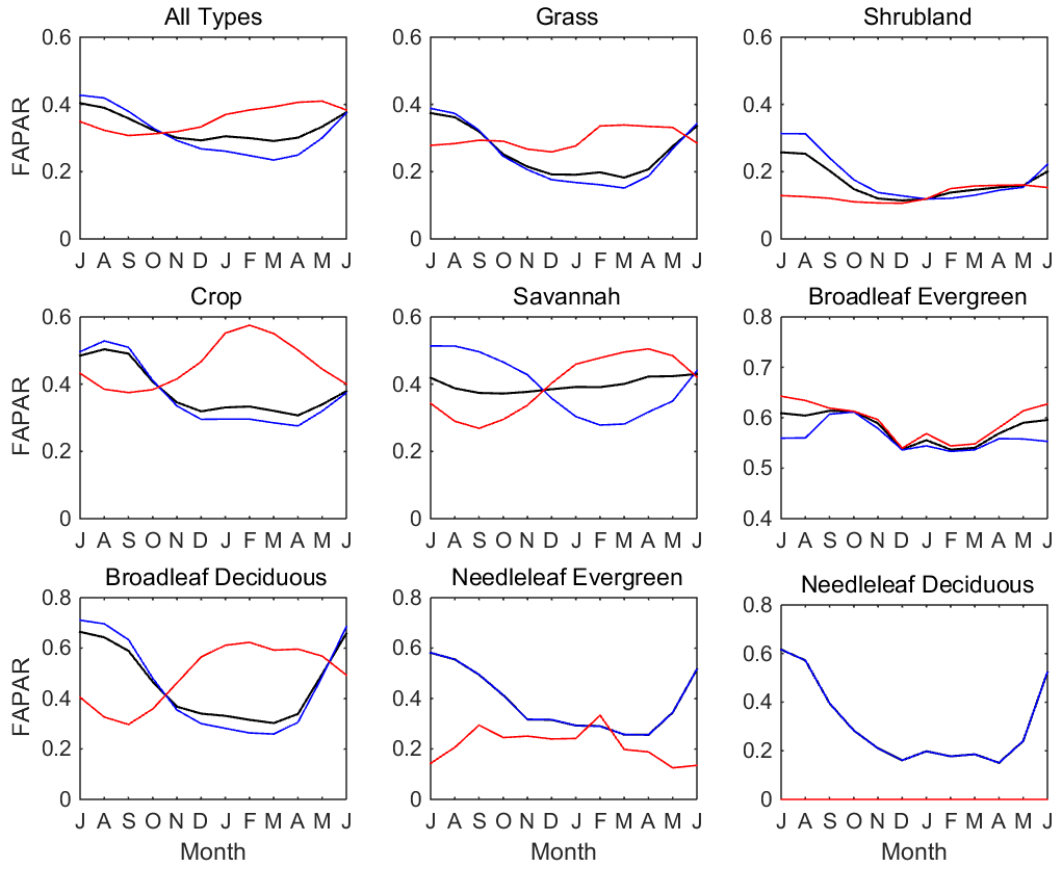

Fig. 2-10 The global (black), northern hemispheric (blue), and southern hemispheric (red) FAPAR mean of all five products over different land cover types during the period July 2005–June 2006.

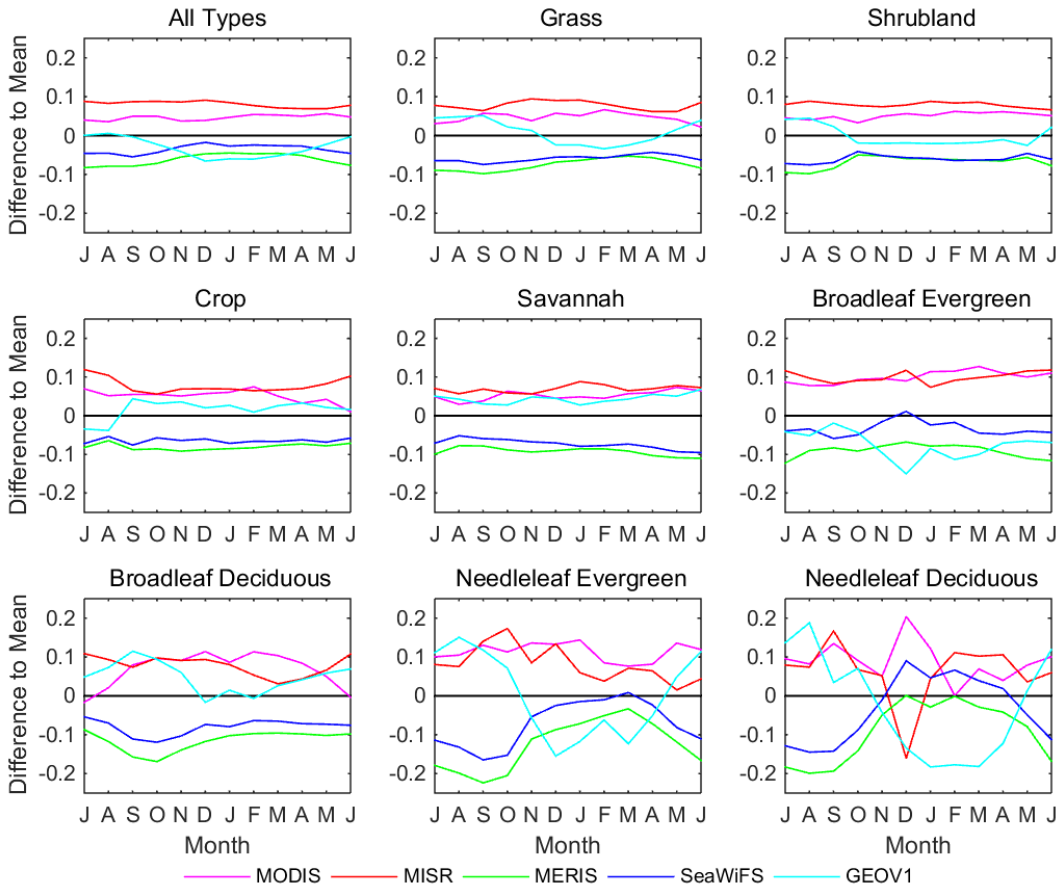

Fig. 2-11 The time series of the mean of quality controlled MODIS, MISR, MERIS, SeaWiFS, and GEOV1 FAPAR products over different land cover types during the period July 2005–June 2006, with the mean of all five products subtracted from each dataset. The black line is for reference.

2.3. Direct Validation of Satellite FAPAR Products

Satellite FAPAR products at 1 km are used for direct validation against 3 years of ground-based continuous measurements of FAPAR at 4 AmeriFlux sites. The validation results of the MERIS, MODIS, MISR, and GEOV1 FAPAR products with in-situ measurements at the AmeriFlux sites are shown in Fig. 2-12. The curves of the SeaWiFS FAPAR product are similar to those of the MERIS FAPAR product, so not

shown here for clarity. The MISR FAPAR values are higher than the MODIS, MERIS, and GEOV1 FAPAR values, especially in the middle of the vegetation growing season. The in-situ FAPAR proxy at Mead Irrigated, Mead Irrigated Rotation, and Mead Rainfed sites reach zero before early April and after middle November, which is the result of harvesting the crops there. Most satellite FAPAR product values around the two sites approach, but are not exactly, zero at the beginning and end of the year, which is caused by the contribution from inhomogeneous land cover, in addition to crops near the sites, or the limited soil reflectance database used by the algorithm (Tao et al., In review). The statistics of comparisons between ground-based and satellite FAPAR products are listed in Table 2-3. The MISR FAPAR product has the highest accuracy over the Mead Rainfed crop site. The GEOV1 FAPAR product has the best accuracy over other crop and forest sites. The MODIS, MISR, and GEOV1 FAPAR products agree better with in-situ measurements at the Bartlett experimental deciduous broadleaf forest site in magnitude than the MERIS FAPAR product does. The MERIS product has a good seasonality profile and little variation of random error caused by cloud contamination, but underestimates FAPAR by 0.12 overall. The underestimation is caused by the green leaf FAPAR estimated by MERIS versus the total FAPAR by ground-based measurements which include the absorptions of both leaf and non-leaf elements.

The validation results are improved when green FAPAR measurements are used as reference data, shown as a magenta line for the year 2006 in the first panel of Fig. 2-12. The improvement is significant for green FAPAR products, with the root mean square error (RMSE) reduced from an average of 0.15 to 0.08. Therefore, the

accuracy of satellite green FAPAR products is improved when validated using green FAPAR instead of total FAPAR measurements. The main reason is the senescence and yellow turning of the leaves at the end of the growing season, and the green FAPAR, estimated by a multispectral optical remote sensing approach, would naturally agree better with in-situ measured green FAPAR than a higher value of total FAPAR (Vina and Gitelson, 2005; Zhang et al., 2005). However, the RMSE error for the MISR total FAPAR product is increased from 0.14 to 0.15. This is understandable as the MISR FAPAR product is total FAPAR and would naturally agree better with total FAPAR measurements. The MODIS FAPAR product has a slightly increased accuracy validated with green FAPAR measurements because its inclusion of direct radiation absorption only, which has an offset from the ground-based FAPAR including both direct and diffuse radiation. Overall, the RMSE of all FAPAR products have been reduced from an average of 0.14 to 0.09. However, the calculation of green FAPAR requires additional simultaneous measurements of green LAI and total LAI to distinguish between green leaves and yellow leaves. The process is labor extensive, and thus green FAPAR measurements are not collected for all the years. Therefore, total FAPAR measurements are used as the main validation data in this study, considering its temporal continuity.

We evaluated the site homogeneity during the vegetation growing season and other seasons using Landsat images at 30 m high resolution. The satellite images within an extent of 1440 m by 1440 m around the sites are depicted in Fig. 2-13. We calculated the standard deviation divided by the mean of the simple ratio between near infrared and red bands in the three regions (the first region contains two sites: Mead Irrigated

and Mead Irrigated Rotation). The values for the Mead Irrigated region are 0.586 and 0.573 during the vegetation growing season and other seasons, respectively. The values for the Mead Rainfed region are 0.747 and 0.381, and the values for the Barlett region are 0.162 and 0.147, respectively. With a smaller ratio between the standard deviation and the mean of the simple ratio, the vegetation in the Barlett region is more homogeneous than in the two Mead regions, and therefore FAPAR is expected to have higher validation accuracy and lower RMSE than that in the other two regions (Table 2-3). The averages of the homogeneity index of the two Mead regions are very close, but the homogeneity index of the Mead Irrigated region remains relatively stable. Therefore, higher validation accuracy is expected in the Mead Irrigated region than in the Mead Rainfed region.

The MODIS, MERIS, MISR, and GEOV1 FAPAR products are compared with the ground-based measurements at the VALERI experimental sites, as shown in Fig. 2-14. Generally speaking, the MERIS, SeaWiFS, and GEOV1 FAPAR have higher accuracy than the MODIS and MISR FAPAR regarding R^2 and RMSE at these sites. There are missing or invalid MERIS FAPAR values at five sites, GEOV1 FAPAR values at four sites, and MISR FAPAR values at three sites; thus, the retrieval rates of the MERIS, GEOV1, and MISR FAPAR products are lower than that of the MODIS and SeaWiFS FAPAR products. The MERIS, SeaWiFS, and GEOV1 FAPAR products perform well at all of the four land cover types, although the MERIS and SeaWiFS FAPAR products slightly underestimate FAPAR compared with in-situ measurements. The MODIS FAPAR product performs well at crop sites. The MISR FAPAR product has better performance than the MODIS FAPAR product at grass

and forest sites. The MODIS and MISR FAPAR products do not rank high in terms of R^2 and RMSE, but has satisfactory biases close to zero values.

Table 2-3 Statistics of comparisons between ground-based and space products.

Site	Product	RMSE	Bias	R^2
Mead Irrigated	MERIS	0.182	−0.092	0.777
	MODIS	0.145	0.009	0.667
	MISR	0.142	0.072	0.761
	GEOV1	0.114	0.067	0.773
Mead Irrigated Rotation	MERIS	0.161	−0.036	0.751
	MODIS	0.159	0.098	0.546
	MISR	0.124	0.104	0.733
	GEOV1	0.113	0.106	0.752
Mead Rainfed	MERIS	0.186	−0.060	0.668
	MODIS	0.143	0.070	0.626
	MISR	0.125	0.043	0.638
	GEOV1	0.149	0.113	0.577
Bartlett	MERIS	0.127	−0.290	0.749
	MODIS	0.167	−0.085	0.642
	MISR	0.103	−0.086	0.842
	GEOV1	0.075	−0.039	0.800

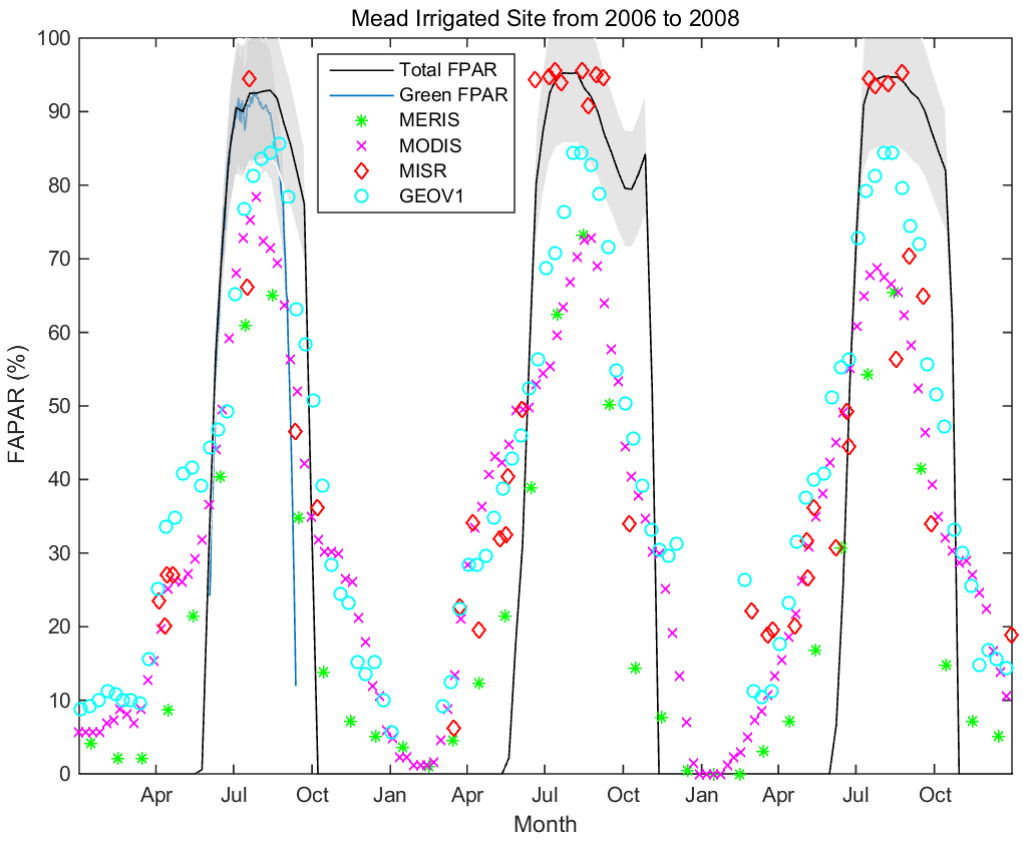
Mead Irrigated Site from 2006 to 2008
Total FPAR
Green FPAR
MERIS
MODIS
MISR
GEOV1
FAPAR (%)
Month
Apr
Jul
Oct
Jan
Apr
Jul
Oct
Jan
Apr
Jul
Oct

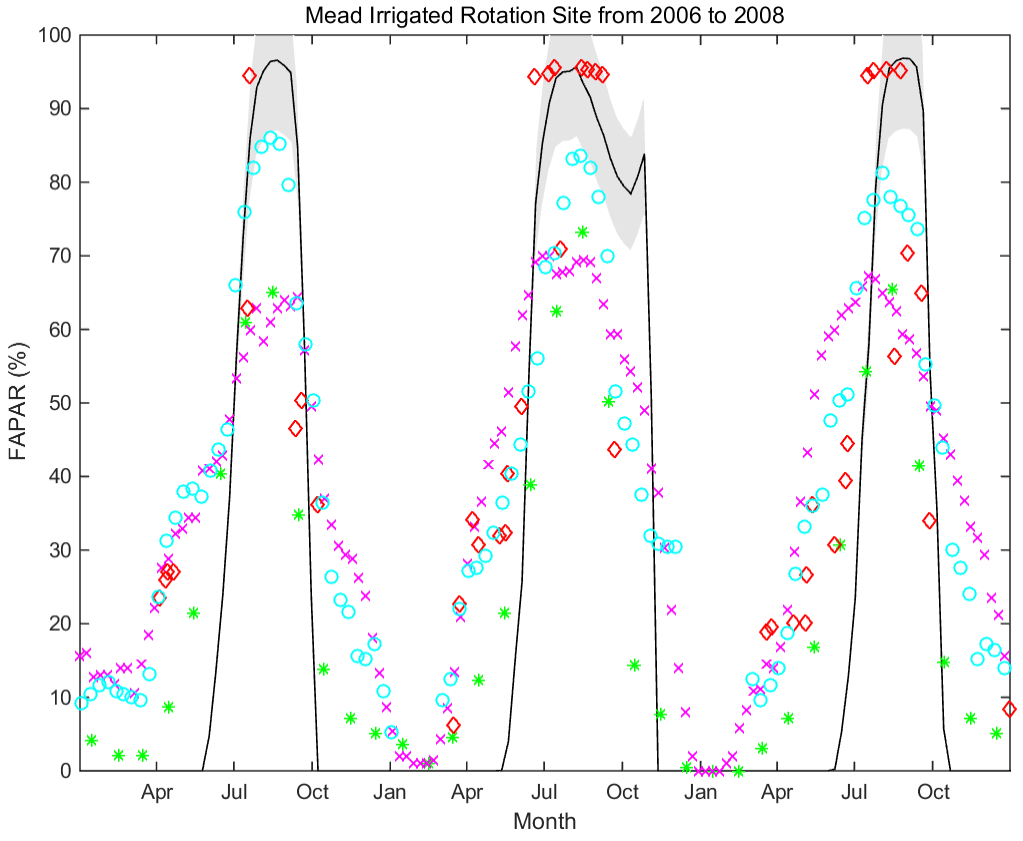
Mead Irrigated Rotation Site from 2006 to 2008
FAPAR (%)
Month
Apr
Jul
Oct
Jan
Apr
Jul
Oct
Jan
Apr
Jul
Oct

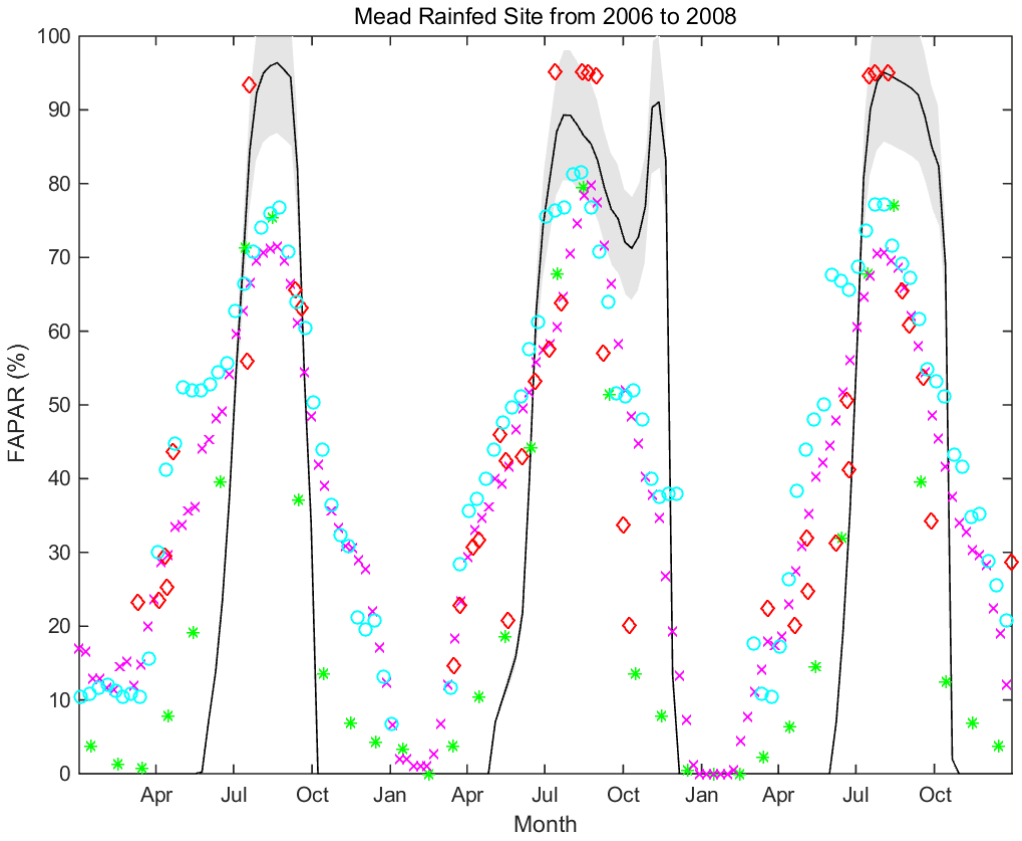
Mead Rainfed Site from 2006 to 2008
FAPAR (%)
Month
0
10
20
30
40
50
60
70
80
90
100
Apr
Jul
Oct
Jan
Apr
Jul
Oct
Jan
Apr
Jul
Oct

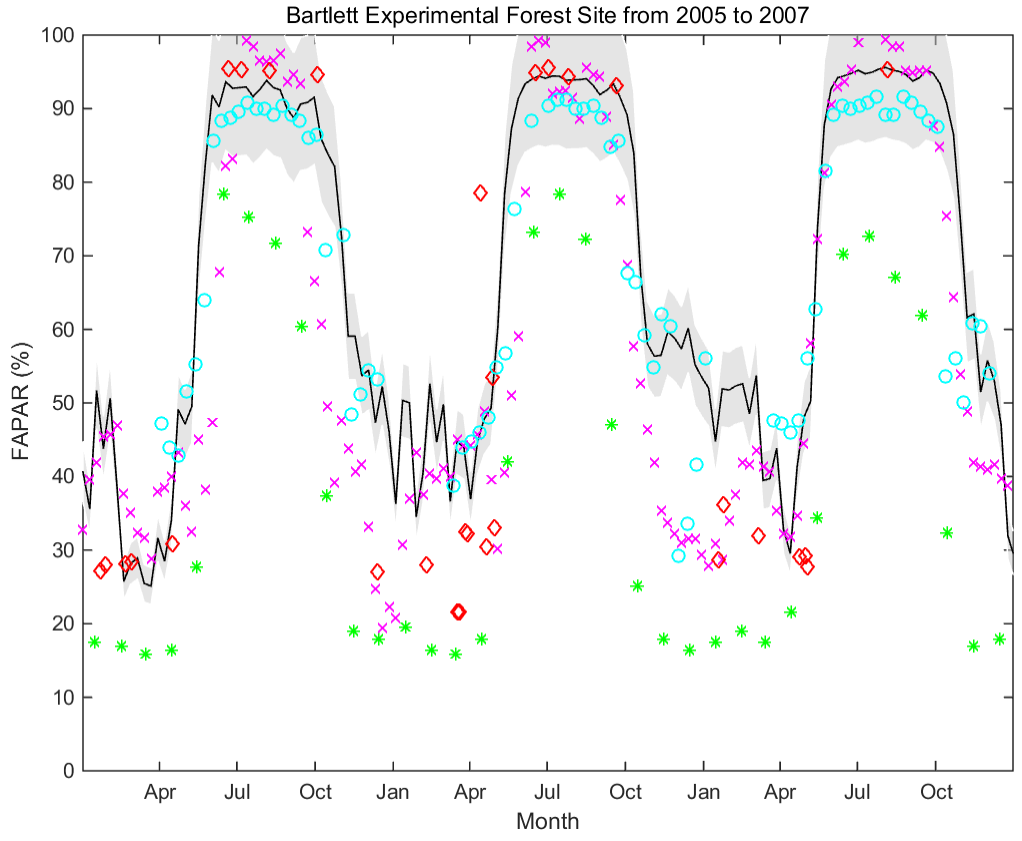
Bartlett Experimental Forest Site from 2005 to 2007
FAPAR (%)
Month
0
10
20
30
40
50
60
70
80
90
100
Apr
Jul
Oct
Jan
Apr
Jul
Oct
Jan
Apr
Jul
Oct

Fig. 2-12 The time series of in-situ FAPAR measurements and satellite products at four AmeriFlux sites. Green FAPAR measurements are depicted in blue line in the top left panel, and total FAPAR measurements are depicted in black line in all panels. The shaded area is the 10% accuracy requirement. The monthly MERIS, 8-day MODIS, 2–9 day MISR, and 10-day GEOV1 FAPAR products are depicted in asterisks, crosses, diamond, and circles, respectively.

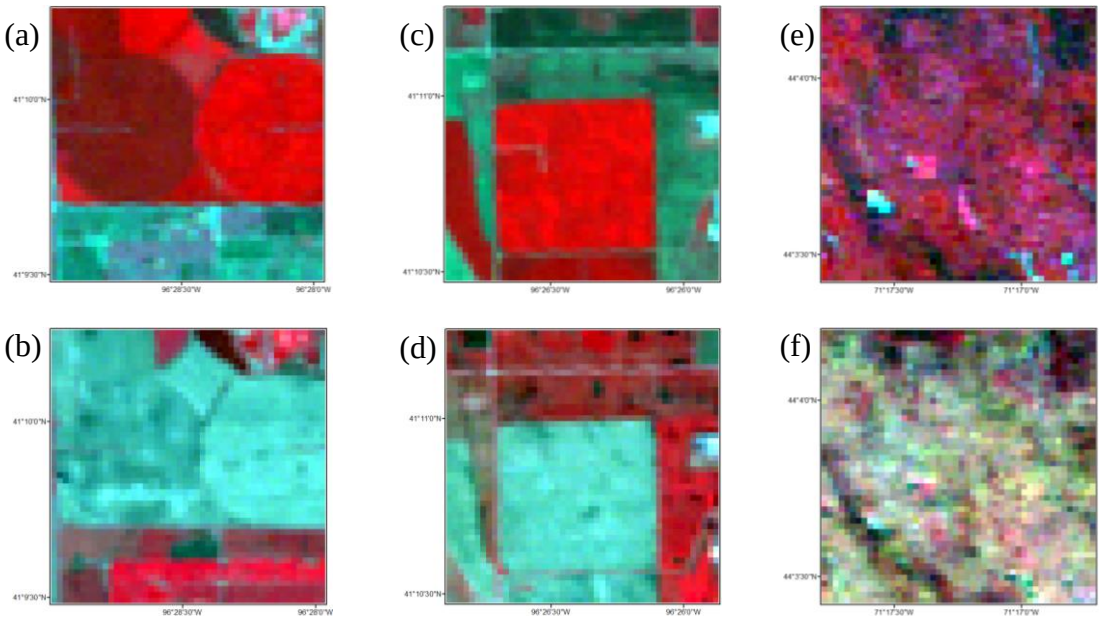

Fig. 2-13 Landsat images with an extent of 1440 m by 1440 m around Mead Irrigated and Mead Irrigated Rotation sites (a–b), Mead Rainfed site (c–d), and Bartlett site (e–f) during the vegetation growing season (a, c, e) and other seasons (b, d, f).

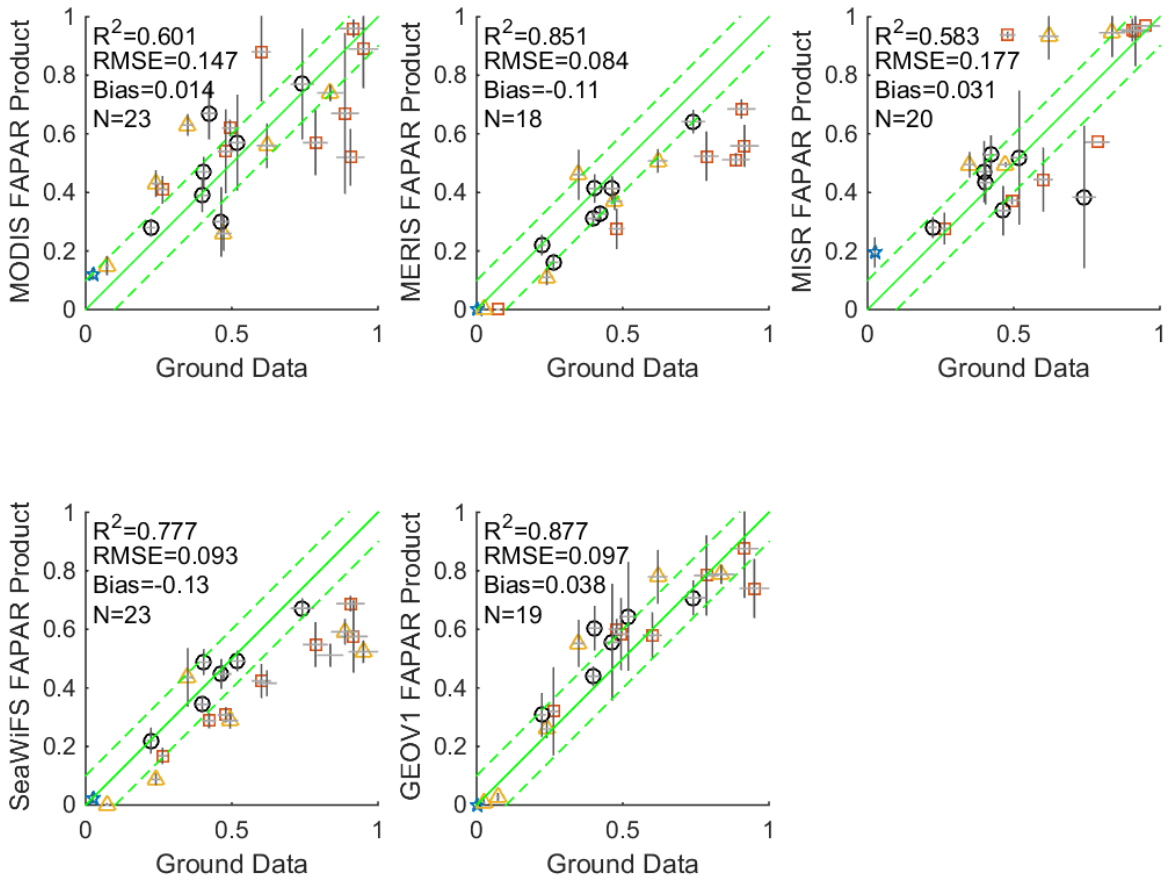

Fig. 2-14 The MODIS, MERIS, MISR, SeaWiFS, and GEOV1 FAPAR products validated with in-situ measurements of VALERI. The land cover of shrubland is represented by a pentagram (⋆), grass by triangle (△), forest by square (□), and crops by circle (○). Horizontal and vertical bars correspond to the uncertainties (±σ). The middle green line is y = x. The two other green lines are y = x ± 0.1, respectively.

2.4. Discussion

The intercomparison studies on the five satellite FAPAR products revealed some discrepancy among them. The FAPAR products have some general relations, in which the MISR FAPAR product often has the highest value, followed by the

MODIS, GEOV1, and SeaWiFS FAPAR products, and the MERIS FAPAR product provides the lowest value. The difference could be partly explained by the differences in the definitions of FAPAR among products. The SeaWiFS, MERIS, and GEOV1 FAPAR products take into account only the absorption by green elements, resulting in lower FAPAR values than the MISR and MODIS FAPAR products, which include the absorption of both green and non-green elements. The difference between the SeaWiFS and MERIS FAPAR products is small, and it can be attributed to the differences in the satellite overpass time and cloud masks (Gobron et al., 2008).

The intercomparison results of global FAPAR products over different land covers show that no noticeable global trend over savannah is observed, which is caused by the cancelling trends of the northern and southern hemispheric FAPAR. Therefore, the difference in the trends of the global FAPAR products over savannah is not significant and is likely to be caused by some random error because of the small magnitude of the trends. The Amazon broadleaf evergreen forests exhibit slightly different seasonal pattern in the Northern Hemisphere from that in the Southern Hemisphere, but the seasonality is weak compared with that over other land cover types. There is a debate on whether a seasonal pattern exists in the Amazon forests. Myneni et al. (2007) have observed a seasonal pattern in the southern hemispheric Amazon rainforest from MODIS data. However, Morton et al. (2014) find consistent canopy structure and greenness during the dry season in the Amazon forests using observations from LiDAR and MODIS (its bidirectional reflectance effect is further corrected). As shown in this study, there could be a weak seasonal pattern over broadleaf evergreen forests in the Southern Hemisphere. The different findings in the

two studies might be explained by the weak seasonal pattern and the large random error caused by the saturation problem of optical remote sensing over heavily leaved Amazon forests.

Regarding the performance of individual FAPAR products, the MERIS has high accuracy and a good seasonality profile, but might underestimate the FAPAR values by 0.05–0.15. Some other studies also find that the MERIS FAPAR product has an uncertainty or negative bias of 0.1(Pickett-Heaps et al., 2014). Martinez et al. (2013) calculate their FAPAR based on the MERIS MGVI algorithm, which turns out to be very low compared with hemispherical pictures based ground measurements, especially in some cultivated sites with bias around 0.16. Because the MERIS and SeaWiFS FAPAR products are very close to each other based on the difference map of the two products in Fig. 2-5 in Section 2.2, similar problems would exist in the SeaWiFS FAPAR product as well. Camacho et al. (2013) evaluate the performance of SeaWiFS FAPAR products at some VALERI sites, and find the bias of SeaWiFS to be 0.16 and RMSE to be 0.23, even higher than MERIS FAPAR product. The negative bias of the MERIS and SeaWiFS FAPAR products could be a result of their retrieval of green FAPAR value. Therefore, this study show that the validation accuracy of the MERIS and SeaWiFS FAPAR products is significantly improved from 0.15 to 0.08 when using in-situ green FAPAR instead of total FAPAR measurements.

The general performances of the MODIS, MISR, and GEOV1 FAPAR products are good when compared with in-situ measurements. The bias is generally less than 0.05. The RMSE is approximately 0.14 when validating with total FAPAR measurements.

However, the MODIS and MISR FAPAR products might overestimate at some sites. For example, Martinez et al. (2013) point out that MODIS shows a tendency to provide high values in cultivated areas and Mediterranean forest, such as Puechabon. The MODIS FAPAR product may also have positive bias for very low FAPAR values. A similar overestimation problem is found in MISR FAPAR data as well, with a positive bias as large as 0.16 in broadleaf forests (Hu et al., 2007). In addition, unrealistically strong temporal variations are found in MODIS data, possibly because of severe cloud contamination during the wet season (Camacho et al., 2013). The MODIS FAPAR product tends to be more consistent with in-situ measurements in the dry season, linked to the absence of significant understory green vegetation, leaving the overlying evergreen woody vegetation as the sole vegetation layer (Pickett-Heaps et al., 2014). Regardless, the latest versions of the FAPAR products have higher levels of consistency than their previous versions, thanks to the continuously improved pre-processing of the products, including better calibration, clouds masks, etc. (Serbin et al., 2013).

Chapter 3 New estimation of FAPAR from multiple satellite data

The targeted accuracy of FAPAR products is 10%, or 0.05, for many applications. However, most of the current FAPAR products have not fulfilled the accuracy requirement yet and thus further improvements are needed. In this chapter, a new FAPAR estimation model was developed based on the radiative transfer for horizontally homogeneous continuous canopy. A spatially explicit parameterization of leaf canopy and soil background reflectance was derived from a thirteen years of MODIS albedo database. The new algorithm requires the input of leaf area index (LAI), which was estimated by a hybrid geometric optic-radiative transfer model suitable for both continuous and discrete vegetation canopies in this study. The FAPAR estimates by the new model was intercompared with reference satellite FAPAR products and validated with field measurements at the VAlidation of Land European Remote sensing Instruments (VALERI) and AmeriFlux experimental sites.

The remainder of the chapter is organized as follows. Section 3.1 introduces data for FAPAR estimation and validation. Section 3.2 describes a new model for FAPAR retrieval. Section 3.3 compares the performance of this new model with those of FAPAR products by direct validation using in situ measurements at the site scale. The model was applied in multiple resolution images at the regional scale in Section 3.4. Section 3.5 discussed and concluded the findings.

3.1. Data

The data used in this chapter include satellite surface reflectance data, satellite FAPAR products including MODIS and MISR ones, and FAPAR in situ measurements from two groups of experimental sites.

3.1.1. Satellite surface reflectance

The MODIS, MISR, Landsat Thematic Mapper (TM), and Enhanced Thematic Mapper Plus (ETM+) reflectance data were used for FAPAR estimation. Satellite surface reflectance products for FAPAR retrieval are listed in Table 3-1. Different spatial resolutions of FAPAR estimates could induce the scaling effect of FAPAR, which happens when the surface is heterogeneous and the retrieval algorithm is nonlinear (Tao et al., 2009; Xu et al., 2009). Because of the scale difference, the validation results at more homogeneous sites are expected to have a higher FAPAR accuracy. We evaluate the heterogeneity around the validation sites in Chapter 2. The FAPAR accuracy at different sites is analyzed and the impact of site heterogeneity on the FAPAR accuracy is explored.

3.1.2. Satellite FAPAR products

The FAPAR estimates were compared with the MODIS and the MISR FAPAR products (Hu et al., 2003; Knyazikhin et al., 1998a; Myneni et al., 2002). Satellite FAPAR products have some differences in the definition of their products in terms of inclusion of diffuse radiation or not. The MISR FAPAR product is the total FAPAR at 10:30 am, considering both direct and diffuse radiation absorbed by the whole canopy. The MODIS FAPAR considers only direct radiation, which may result in a smaller value than the MISR FAPAR product (Hu et al., 2003; Tao et al.). Regardless

of the different definitions, differences among FAPAR products vary over different land covers and are larger than as expected by the differences in definitions. Poorest agreement in the magnitude of FAPAR among the datasets occurs within mixed and needleleaf forests. Agreement among datasets does not imply accuracy; however the more datasets agree over a particular area, the greater the likelihood that those datasets are capturing the variable correctly (McCallum et al., 2010).

Spatial and temporal resolutions and temporal coverage information of satellite FAPAR products, as well as their retrieval algorithms, are listed in Table 3-2. Spatial resolutions of satellite FAPAR products vary from 1 km to 9 km, and temporal resolutions vary from 8 days to 1 month. Spatial aggregation and temporal interpolation are necessary to intercompare their values across multiple scales. Considering the availability of continuous measurements of FAPAR, temporal values of FAPAR products were linearly interpolated to the highest temporal resolution to ensure enough data points validated with in situ measurements.

3.1.3. FAPAR in situ measurements

The FAPAR validation data were collected from two groups of experimental sites: VAlidation of Land European Remote sensing Instruments (VALERI, WWW1) and AmeriFlux (WWW2). The VALERI sites are widely distributed around the world and useful for spatial validation over different land covers (Camacho et al., 2013; Weiss et al., 2007). The AmeriFlux sites are intended for temporal validation of FAPAR estimates and products, in consideration of their continuous measurements of FAPAR. The land covers of the 27 VALERI and AmeriFlux sites include 9 forests (1 of

Ameriflux and 8 of VALERI), 11 crops (3 of Ameriflux and 8 of VALERI), 6 grass sites (of VALERI), and 1 shrubland site (of VALERI). Their distributions are shown in Fig. 2-1. The geolocation and land cover information of the AmeriFlux and the VALERI sites are listed in Table 2-1 for reference.

Table 3-1 The characteristics of satellite surface reflectance products used in this study.

Reflectance product	Temporal coverage	Temporal resolution	Spatial resolution	Projection
MODIS MOD09 (C5) (WWW3)	Feb 18, 2000–	8 days	500 m	Sinusoidal
MISR (L2) (WWW4)	Feb 24, 2000–	Equator: 9 days, Polar: 2 days	1100 m	Space Oblique Mercator
TM (WWW8)	Mar 1, 1984 –	16 days	30 m	Universal Transverse Mercator (UTM)
ETM+ (WWW8)	Apr 15, 1999–	16 days	30 m	UTM

Table 3-2 The characteristics of moderate-resolution satellite FAPAR products used in this study.

FAPAR product	Temporal coverage	Temporal resolution	Spatial resolution	Projection	Algorithm
MODIS MOD15 (C5) (WWW3)	Feb 18, 2000–	8 days	1000 m	Sinusoidal	Look up table method built on 3D stochastic radiative transfer model for different biomes (Myneni et al., 2002).
MISR (L2) (WWW4)	Feb 24, 2000–	Equator: 9 days, Polar: 2 days	1100 m	Space Oblique Mercator	Radiative transfer (RT) model with inputs of LAI and soil reflectance without assumptions on biomes (Knyazikhin et al., 1998a).

3.2. Methodology

In moderate resolution images, vegetation pixels are almost continuously distributed across large regions in the imagery. Therefore, we assumed the land cover was horizontally homogeneous within the targeted surface and developed a four-stream radiative transfer model of continuous canopy for FAPAR retrieval. Canopy absorptance along the direct and diffuse light penetrating paths were calculated separately and summed up using a ratio of scattering light. We denote T_0, T_f, and T_v as the canopy transmittance along the direct light penetrating, the diffuse light penetrating, and the observing paths, respectively; and denote $\rho_{v,\lambda}$, $\rho_{g,\lambda}$, and $\rho_{c,\lambda}$ as the hemispherical albedos of vegetation, soil background, and leaf canopy, respectively. FAPAR was calculated as the integral of canopy absorptance in the upper hemisphere from 400 to 700 nm, as follows:

$$\begin{aligned}\mathrm{FPAR} = (1-\beta)\int_{400}^{700}\int_{0}^{\frac{\pi}{2}}[\left(1-T_0-2\rho_{v,\lambda}(\theta)\right)+\left(1-T_v(\theta)-2\rho_{v,\lambda}(\theta)\right)\frac{T_0\rho_{g,\lambda}}{1-\rho_{g,\lambda}\rho_{v,\lambda}(\theta)}]\cos\theta\sin\theta d\theta d\lambda + \\ \beta\int_{400}^{700}\int_{0}^{\frac{\pi}{2}}[\left(1-T_f-2\rho_{v,\lambda}(\theta)\right)+\left(1-T_v(\theta)-2\rho_{v,\lambda}(\theta)\right)\frac{T_f\rho_{g,\lambda}}{1-\rho_{g,\lambda}\rho_{v,\lambda}(\theta)}]\cos\theta\sin\theta d\theta d\lambda\end{aligned} \quad (1)$$

where canopy transmittance along the direct light penetrating, the diffuse light penetrating, and the observing paths can be expressed as:

$$T_{0,f,v} = \exp(-\lambda_0 \frac{G_{s,f,v}}{\mu_{s,f,v}} LAI) \quad (2)$$

and hemispherical albedo of vegetation is:

$$\rho_{v,\lambda}(\theta) = \rho_{c,\lambda}\left[1-\exp\left(-\lambda_0 \frac{G_v}{\mu_v(\theta)}\Gamma(\phi)LAI\right)\right]+ \\ \beta\rho_{c,\lambda}\left[\exp\left(-\lambda_0 \frac{G_v}{\mu_v(\theta)}\Gamma(\phi)LAI\right)-\exp\left(-\lambda_0 \frac{G_v}{\mu_v(\theta)}LAI\right)\right] \quad (3)$$

In (2) and (3), λ_0 is a Nilson parameter accounting for vegetation clumping effect, μ_s and $\mu_v(\theta)$ are cosine values of solar (θ_s) and the viewing (θ) zenith angles, β is a ratio of scattering light, and G_s and G_v are the mean projection of a unit foliage area along the solar and viewing directions, respectively (Liang, 2004; Ross, 1981):

$$G_{s,v} = \frac{1}{2\pi}\int_{2\pi} g_L(\Omega_L)\left|\Omega_L \cdot \Omega_{s,v}\right| d\Omega_L \quad (4)$$

where $1/2\pi \cdot g_L(\Omega_L)$ is the probability density of a distribution of leaf normals with respect to the upper hemisphere, i.e., leaf angle distribution. An empirical function $\Gamma(\phi)$ describes hot-spot phenomenon, where a symbol ϕ accounts for sun-target-sensor position and depends on the angle between solar and viewing directions and leaf angle distribution of the canopy.

$$\Gamma(\phi) = \exp\left(\frac{-\phi}{180-\phi}\right) \quad (5)$$

Assume LAI is known for FAPAR estimation. A hybrid geometric optic-radiative transfer model for LAI retrieval has been developed earlier and is included in the Appendix for convenience (Tao et al., 2009; Xu et al., 2009).

Other important inputs for FAPAR estimation proposed in this study are soil background and leaf canopy albedos. Some typical soil background and leaf canopy

albedos could be used for simplicity, but they may deviate from local conditions. Taking into account the applicability of surface albedos at local conditions, we derived a database of soil background and leaf canopy albedos upon thirteen years of surface albedo time series (He et al., 2015). The multiyear mean soil background and leaf canopy albedo was generated using the 500 m spatial resolution MODIS surface anisotropy products (MCD43A) during the period 2000–2012. The "soil line" characteristics were used to separate vegetation and bare soil on a pixel basis over the United States. The leaf canopy albedo was generated from the vegetation albedo at the peak of the growing season. Therefore, the database provides locally pixel basis soil background and leaf canopy albedos as input for FAPAR estimation models. Fig. 3-1shows an example of the derived albedos of soil background and leaf canopy.

Overall, the FAPAR estimation model (1) – (5) includes reflective anisotropic characteristics caused by sun-target-sensor geometry, vegetation clumping effect, and hot-spot effect. In consideration of model simplicity and computational efficiency, it neglects reflective anisotropic characteristics caused by soil background and leaf canopy while retaining a high accuracy by using locally applicable soil background and leaf canopy albedos. The model is referred as "4S" model for simplicity in the remaining of this study.

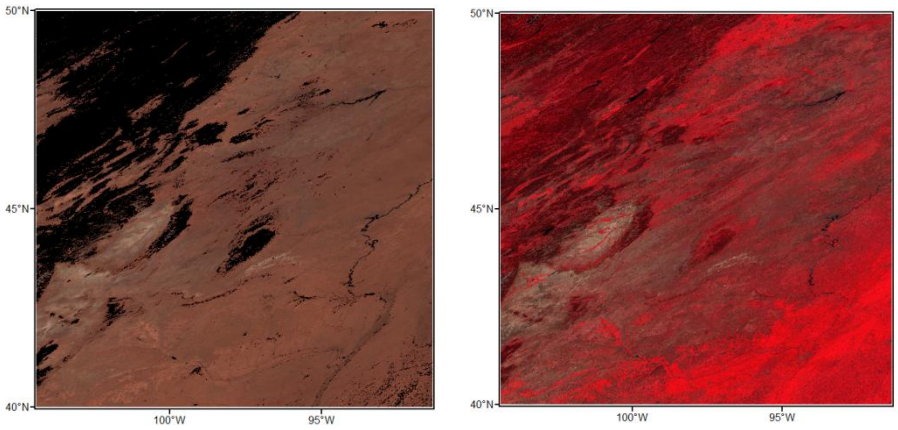

Fig. 3-1 The distributions of soil background (left) and leaf canopy (right) albedos on clear days in a thirteen-year surface albedo database within the extent of MODIS tile H10V04 (NIR-Red-Green false color composition).

3.3. Validation and Comparison with Some Reference FAPAR Products

The FAPAR estimated by the presented model were validated using in situ measurements at the site scale and the results were compared with some reference FAPAR products. Specifically, the FAPAR was estimated from MODIS surface reflectance data and the results were validated and compared with the MODIS reference FAPAR product in Section 3.3.1. The FAPAR was estimated from MISR surface directional reflectance data and the results were validated and compared with the MISR reference FAPAR product in Section 3.3.2. The FAPAR was estimated from Landsat reflectance data and the results were validated using in situ measurements in Section 3.3.3.

3.3.1. Validation and comparison with the MODIS official FAPAR product

The NASA MODIS surface reflectance data (MOD09) and land cover information were combined to estimate vegetation LAI and FAPAR values using the presented model, with input parameters of soil background and leaf canopy albedo from a database introduced in Section 3.2. The LAI was estimated first and then used as a parameter for FAPAR estimation. The LAI/FAPAR estimates were compared with the MODIS LAI/FAPAR products. The QA flags were used to select the high quality MODIS data with main algorithm retrievals. As control experiments, the FAPAR was estimated from the MODIS surface reflectance data directly (referred as MOD_4SH based FAPAR) or from the MODIS Official LAI product (referred as MOD_4SO based FAPAR). Fig. 3-2 shows scatterplots of both of the MODIS LAI and FAPAR products (d and e) and the LAI and the FAPAR estimates from this study (a and c) validated with field measurements of VALERI. Overall, the MODIS LAI product underestimated slightly at these sites. The MODIS FAPAR product performed better than the LAI product regarding bias, R^2, and RMSE (d and e). The MODIS LAI estimates from this study decreased the negative bias compared with in situ-measured LAI, but the correlation with field data was greatly improved compared with the MODIS LAI product (a). The MOD_4SO based FAPAR had slightly increased R^2 and decreased RMSE compared with the MODIS FAPAR product (b). Both of the MODIS FAPAR product and MOD_4SH based FAPAR had little or no bias, but the FAPAR estimates from this study had better correlation with in situ data and smaller RMSE than the MODIS FAPAR product did (c and e). The improvement of MOD_4SH based FAPAR over MOD_4SO based FAPAR infers that the

improvement of the FAPAR estimate was also a result of an improved LAI value as input. The MODIS FAPAR product performed well at shrubland and crop sites, but the deviations from in situ values were large at forest and grass sites. The FAPAR estimates from this study reduced the uncertainty at forest and grass sites from 0.155 to 0.094. The FAPAR estimates and products were lower than field measurements at some forest sites, which is understandable because field measured FAPAR included the absorption of tree trunks and branches (Fang et al., 2005).

The FAPAR estimates by the presented model were compared with the MODIS FAPAR product and validated at 4 AmeriFlux sites for 3 years (Fig. 3-3). Compared with the MODIS FAPAR product, the FAPAR estimates by the presented model increased R^2 for all of the four sites (Table 3-3). The improvement was most apparent at the Mead Irrigated Rotation and Bartlett experimental deciduous broadleaf forest site, where the R^2 were improved by around 20%. The MOD_4SH based FAPAR had similar RMSE as the MOD_4SO based FAPAR, but the R^2 was improved by about 8% on average. The FAPAR measurements at Mead Irrigated, Mead Irrigated Rotation, and Mead Rainfed sites reached zero before early April and after middle November, which was a result of harvesting the crops there. The values of the MODIS FAPAR product around the three Mead sites approached but were not exactly zero at the beginning and the end of the year, which could be caused by the contribution from inhomogeneous land cover inside the 1×1 km extent of the MODIS FAPAR pixel, or the limitations of the models and the inputs. The presented model estimated FAPAR (MOD_4SH based) from surface reflectance data at 500 m spatial resolution, so that the crops were homogeneous within this extent. Combined with locally

applicable soil background albedo data, the model detected vegetation growing season well and reduced the FAPAR uncertainty by 5%. Meanwhile, the FAPAR estimates from the MODIS Official LAI product (MOD_4SO based FAPAR) was very similar to the MODIS FAPAR product, but had a smoother curve over years. The improvement of the MOD_4SH based FAPAR over the MOD_4SO based FAPAR infers that the improvement of FAPAR estimate was also a result of an improved LAI value as input. The presented model had comparable performance as the MODIS FAPAR model when using the same LAI value as input.

The MOD_4SH based FAPAR agreed well with in situ measurements in the first half of the years. However, some underestimation occurred in the FAPAR estimates from this study in the three crop sites in the latter half of the years, or at the end of the growing season specifically, which was caused by the senescence and yellow turning of the leaves, and thus the FAPAR from remote sensing (green FAPAR) is different from measurements (total FAPAR) (Vina and Gitelson, 2005; Zhang et al., 2005). In this case, the accuracy of the MODIS FAPAR product was improved from 0.140 to 0.082 and the accuracy of MOD_4SH based FAPAR was improved from 0.139 to 0.069 when using green FAPAR measurements as validation data. The FAPAR estimates from this study and the MODIS FAPAR products were lower than field measurements at the end of the growing season at the Bartlett forest site. This is understandable because field measured FAPAR included the absorption of tree trunks and branches (Fang et al., 2005).

Table 3-3 The errors of the FAPAR products and the FAPAR estimates validated using in situ measurements.

Site	FAPAR	RMSE	Bias	R^2
Mead Irrigated	MOD_4SH based	0.139	−0.083	0.773
	MIS_4SH based	0.132	−0.012	0.889
	MOD_4SO based	0.116	0.024	0.687
	MIS_4SO based	0.136	0.135	0.789
	MODIS Official product	0.140	0.009	0.667
	MISR Official product	0.153	0.072	0.756
	Landsat_4SH based	0.224	−0.087	0.692
Mead Irrigated Rotation	MOD_4SH based	0.141	−0.051	0.809
	MIS_4SH based	0.181	0.034	0.774
	MOD_4SO based	0.136	0.116	0.569
	MIS_4SO based	0.139	0.083	0.736
	MODIS Official product	0.161	0.098	0.546
	MISR Official product	0.157	0.104	0.732
	Landsat_4SH based	0.170	−0.053	0.823
Mead Rainfed	MOD_4SH based	0.107	−0.069	0.632
	MIS_4SH based	0.157	0.063	0.778
	MOD_4SO based	0.127	0.086	0.625
	MIS_4SO based	0.149	0.107	0.637
	MODIS Official product	0.143	0.070	0.626

	MISR Official product	0.163	0.047	0.622
	Landsat_4SH based	0.217	−0.053	0.731
Bartlett	MOD_4SH based	0.124	−0.089	0.709
	MIS_4SH based	0.075	−0.083	0.898
	MOD_4SO based	0.106	0.031	0.708
	MIS_4SO based	0.097	−0.076	0.858
	MODIS Official product	0.203	−0.089	0.566
	MISR Official product	0.125	−0.086	0.842
	Landsat_4SH based	0.133	−0.078	0.790

MOD_4SH based FAPAR: the FAPAR estimates from the MODIS surface reflectance data from this study.

MIS_4SH based FAPAR: the FAPAR estimates from the MISR surface reflectance data from this study.

MOD_4SO based FAPAR: the FAPAR estimates using the MODIS Official LAI product.

MIS_4SO based FAPAR: the FAPAR estimates using the MISR Official LAI product.

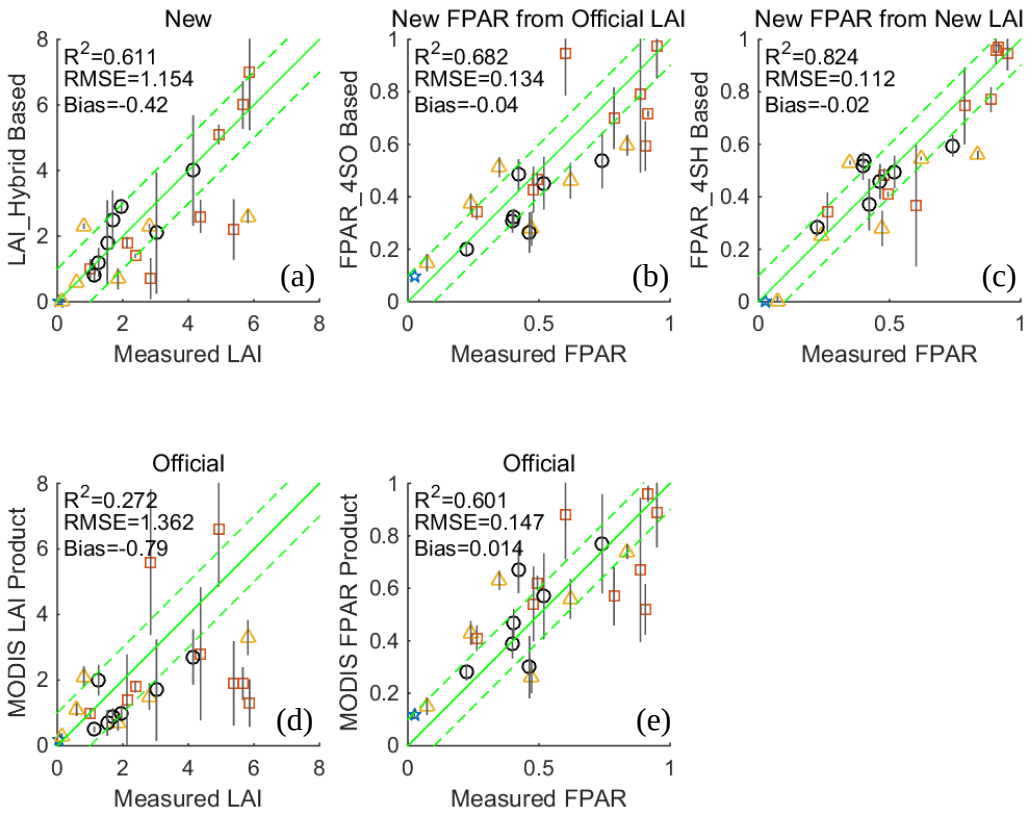

Fig. 3-2 Validation of the estimated LAI and the FAPAR estimates from this study (a–c) and the MODIS official products (d, e) using in situ measurements at VALERI sites. The land cover of shrubland is represented by a pentagram (⋆), grass by triangle (△), forest by square (□), and crops by circle (○). Vertical bars correspond to the uncertainties (±σ). The middle green line is y = x. The other green lines are y = x ± 1.0 (a, d) and y = x ± 0.1 (b, c, e), respectively.

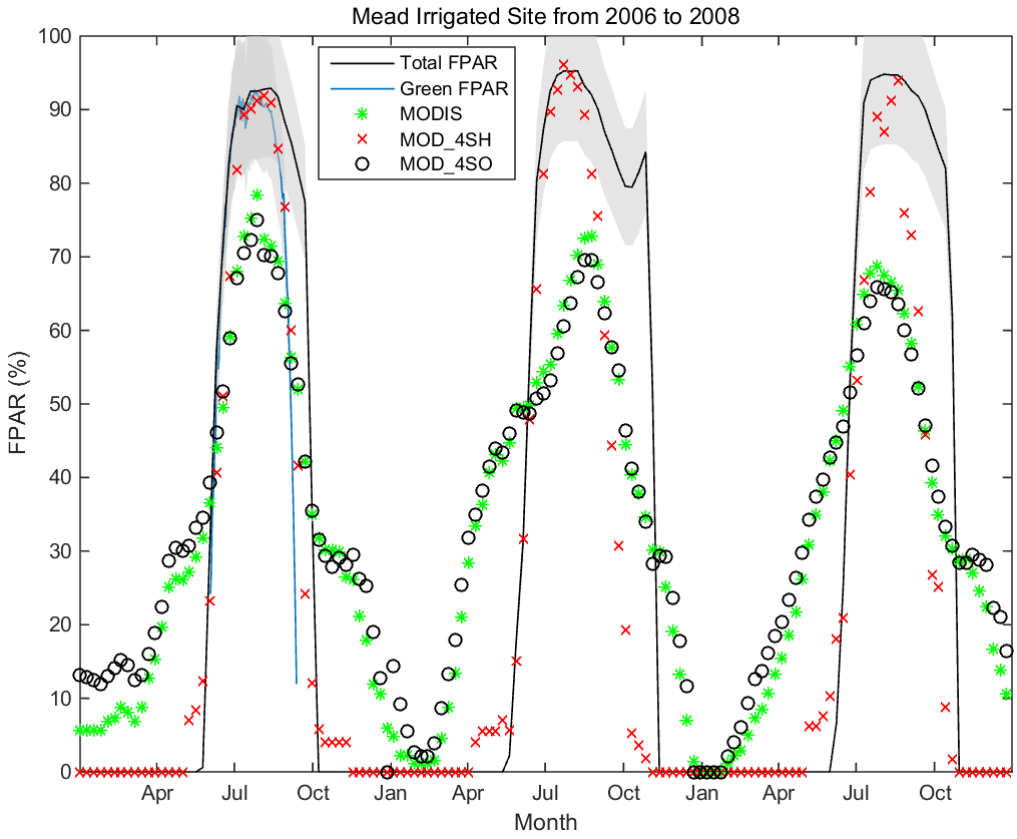
Mead Irrigated Site from 2006 to 2008
Total FPAR
Green FPAR
MODIS
MOD_4SH
MOD_4SO
FPAR (%)
Month
Apr
Jul
Oct
Jan
Apr
Jul
Oct
Jan
Apr
Jul
Oct

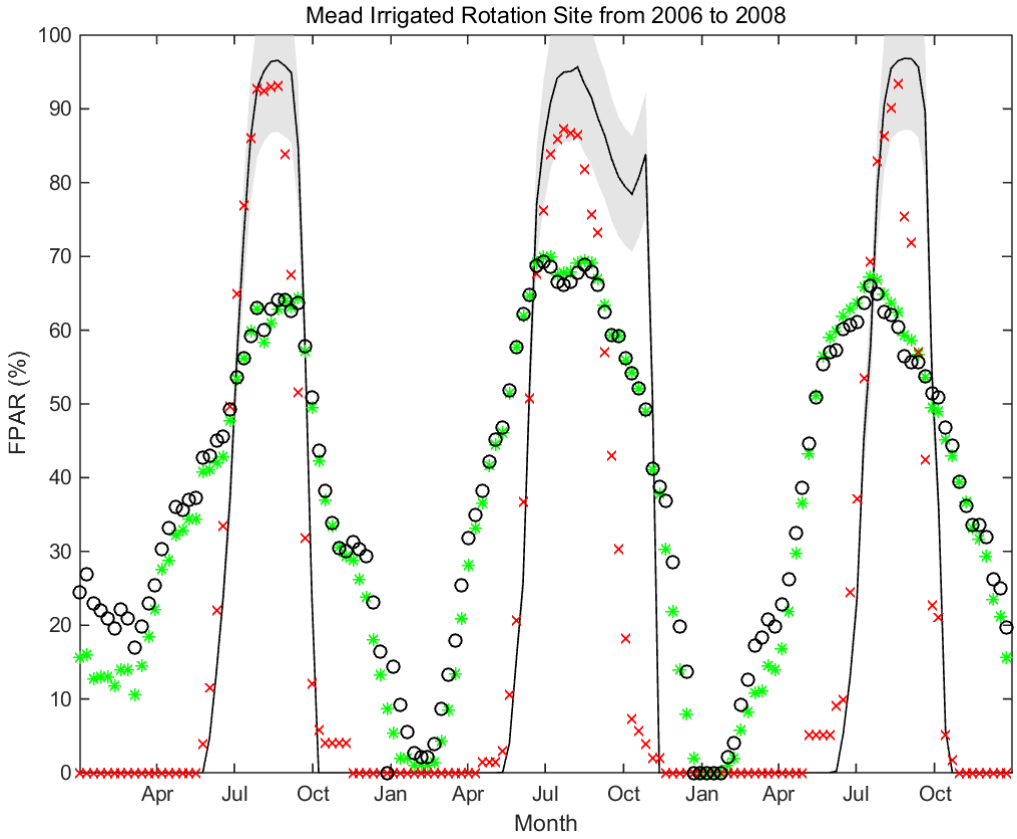
Mead Irrigated Rotation Site from 2006 to 2008
FPAR (%)
Month
Apr
Jul
Oct
Jan
Apr
Jul
Oct
Jan
Apr
Jul
Oct

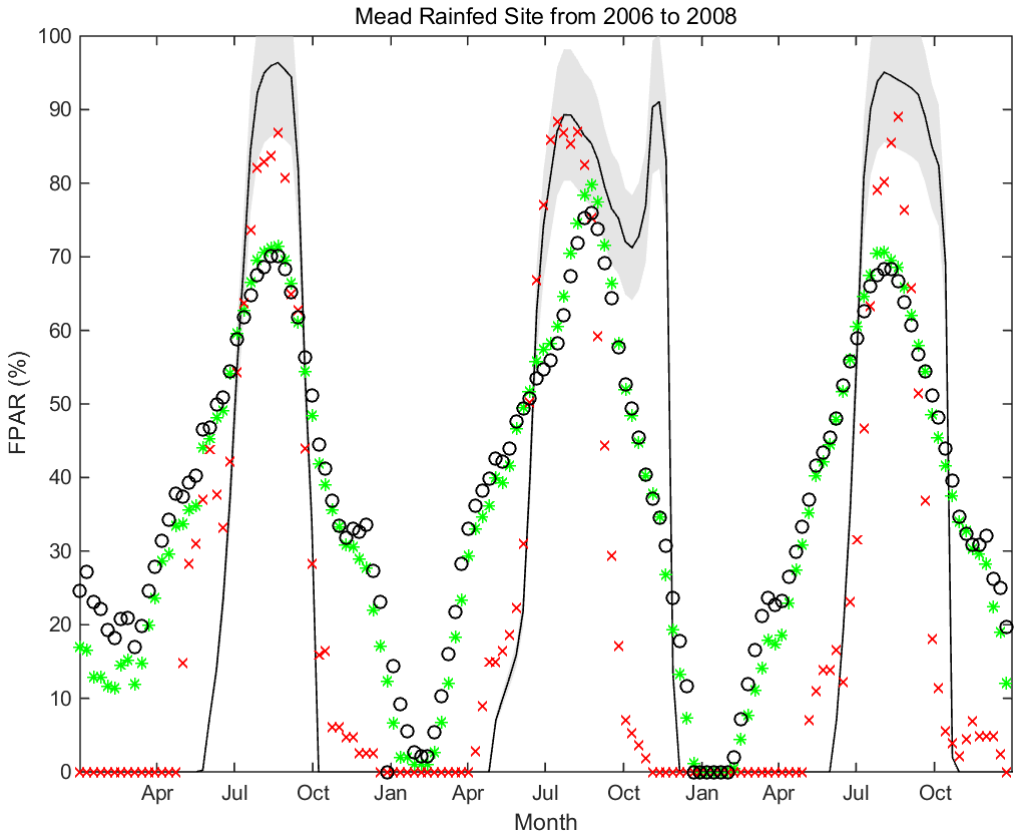
Mead Rainfed Site from 2006 to 2008
FPAR (%)
Month
0
10
20
30
40
50
60
70
80
90
100
Apr
Jul
Oct
Jan
Apr
Jul
Oct
Jan
Apr
Jul
Oct

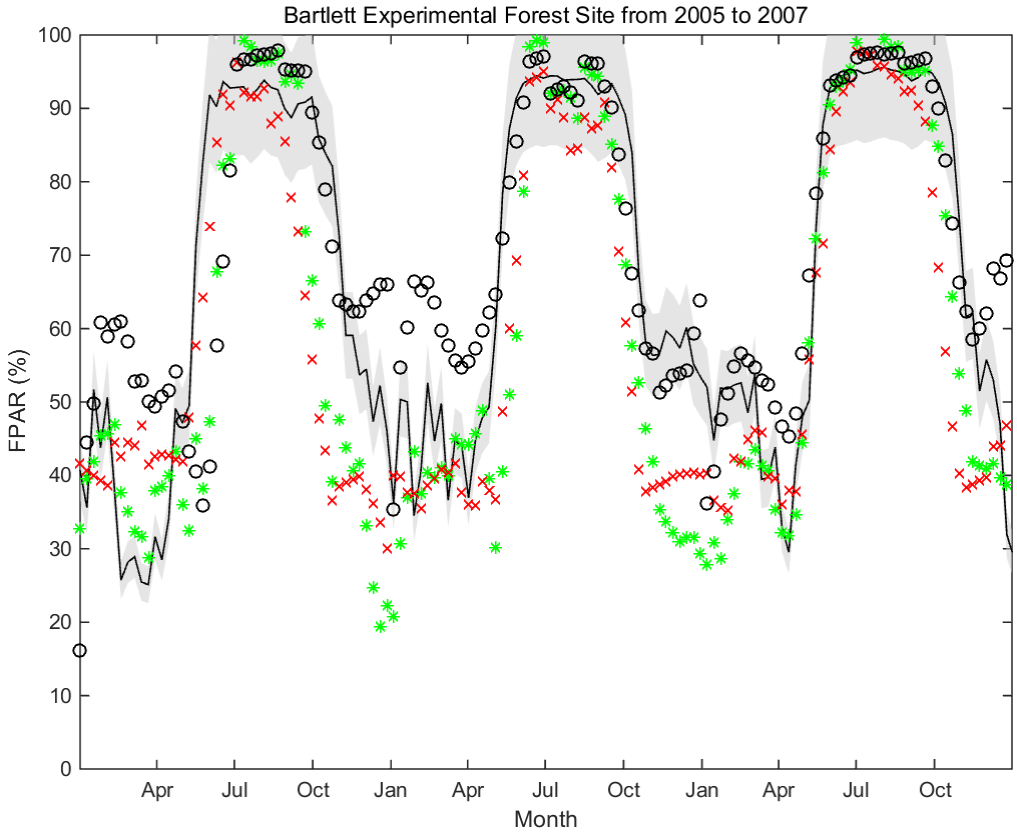
Bartlett Experimental Forest Site from 2005 to 2007
FPAR (%)
Month
0
10
20
30
40
50
60
70
80
90
100
Apr
Jul
Oct
Jan
Apr
Jul
Oct
Jan
Apr
Jul
Oct

Fig. 3-3 The time series of the in situ measurements and the MODIS FAPAR estimates from this study at four AmeriFlux sites. Green FAPAR measurements are depicted in blue line in the first panel, and total FAPAR measurements are depicted in black line in all panels. The shaded area is the 10% accuracy requirement. The "MODIS" represents the MODIS official FAPAR product, the MOD_4SH is the FAPAR estimate from the newly estimated LAI from this study, and MOD_4SO is the FAPAR estimate from the MODIS official LAI product.

3.3.2. Validation and comparison with the MISR official FAPAR product

The MISR surface directional reflectance data and land cover information were combined to estimate vegetation LAI and FAPAR values using the presented model. The LAI was estimated and then used as a parameter for FAPAR estimation. The LAI/FAPAR estimates were compared with the MISR LAI/FAPAR products. As control experiments, the FAPAR was estimated from the MISR surface directional reflectance data directly (referred as MIS_4SH based FAPAR) or from the MISR Official LAI product (referred as MIS_4SO based FAPAR). The MISR LAI and FAPAR products (d and e) and the LAI and the FAPAR estimates from MISR reflectance data by the presented model (a and c) were validated around VALERI sites, as shown in Fig. 3-4. The MISR LAI product underestimated at some forest and crop sites. The MISR FAPAR product performed better than the LAI product regarding bias, R^2, and RMSE (d and e). The MISR LAI estimates from this study overestimated slightly compared with in situ measured LAI, but its RMSE was slightly smaller than that of the MISR LAI product (a). The MIS_4SO based FAPAR

had improved R^2 and reduced RMSE values compared with the MISR FAPAR product (b). Both of the MISR FAPAR product and the MIS_4SH based FAPAR had little to almost no bias, but the latter had better correlation with in situ data and smaller RSME than the former (c and e). The improvement of the MIS_4SH over the MIS_4SO infers that the improvement of the FAPAR estimates was also a result of improved LAI values as input. Note that the RMSE of the MISR FAPAR estimates was slightly smaller than that of the MODIS FAPAR estimates from this study (0.105 compared with 0.112). Both of the MODIS and the MISR FAPAR estimates from this study performed well at grass and forest sites with an average accuracy of 0.104 (Fig. 3-2 c and Fig. 3-4 c). The MISR FAPAR estimates were improved at crop sites compared with the MODIS FAPAR estimates.

The FAPAR estimates were validated with 3 years continuous measurements at 4 AmeriFlux sites (Fig. 3-5). Because of only a few valid satellite observations over years, the MISR FAPAR product, the MIS_4SO based FAPAR, and MIS_4SH based FAPAR are depicted as green asterisks, black circles, and magenta triangles, respectively. Compared with the MODIS FAPAR product in Fig. 3-3, the MISR FAPAR product and the FAPAR estimates from this study had larger values, especially in the middle of vegetation growing season. The MIS_4SO based FAPAR was very similar to the MISR FAPAR product, but had a smoother trend over years. Compared with the MISR FAPAR product, the FAPAR estimates by the presented model increased R^2 for all of the four sites (Table 3-3). The improvement was most apparent at the Bartlett Experimental forest site, with a reduction of RMSE by 0.05. The improvement of the MIS_4SH based FAPAR over the MIS_4SO based FAPAR

infers that the improvement of FAPAR estimate was primarily a result of an improved LAI value as input. The presented model had comparable performance with the MISR FAPAR model when using the same LAI value as input.

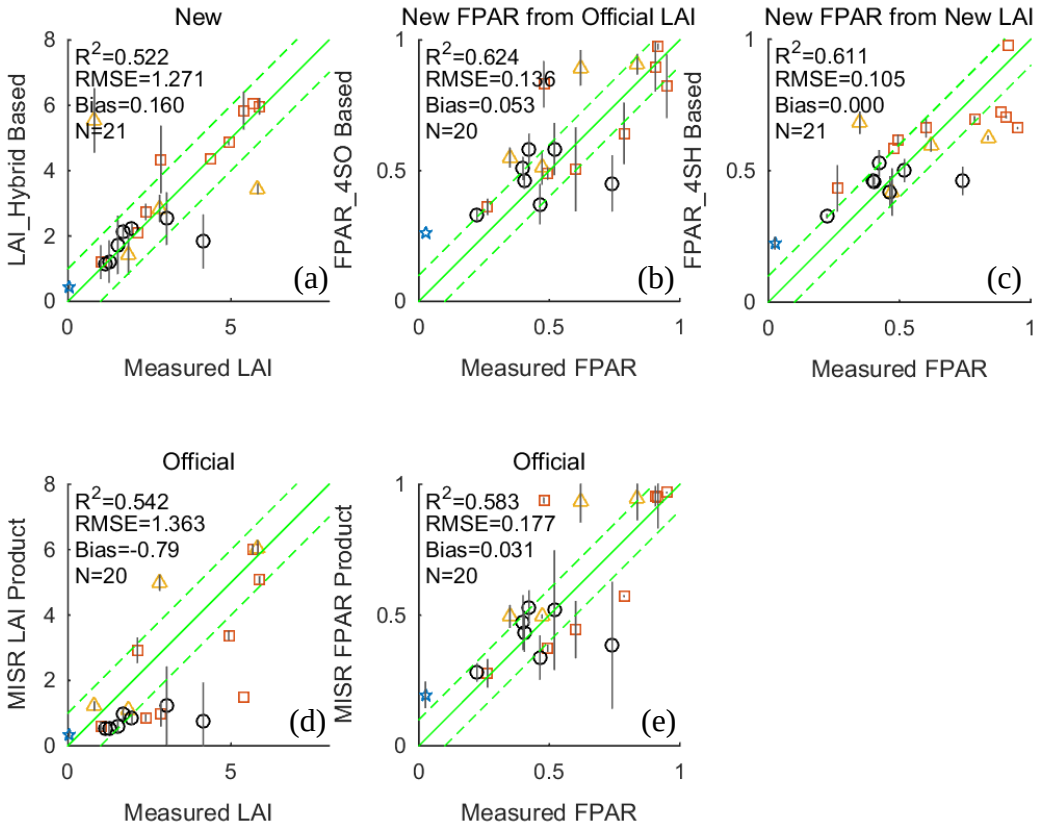

Fig. 3-4 Validation of the estimated LAI and the FAPAR estimates from this study (a–c) and the MISR official products (d-e) using in situ measurements at VALERI sites. The land cover of shrubland is represented by a pentagram (*), grass by triangle (△), forest by square (□), and crops by circle (○).Vertical bars correspond to the uncertainties (±σ). The middle green line is y = x. The other green lines are y = x ± 1.0 (a, d) and y = x ± 0.1 (b, c, e), respectively.

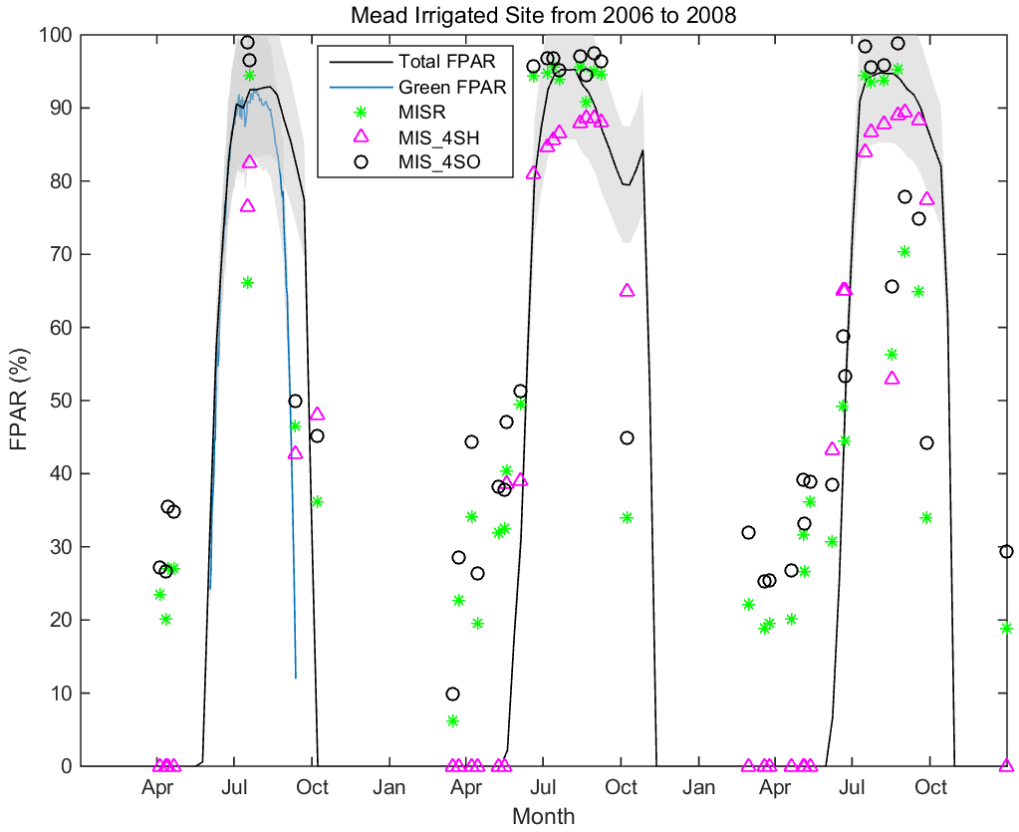
Mead Irrigated Site from 2006 to 2008
Total FPAR
Green FPAR
MISR
MIS_4SH
MIS_4SO
FPAR (%)
Month
Apr
Jul
Oct
Jan

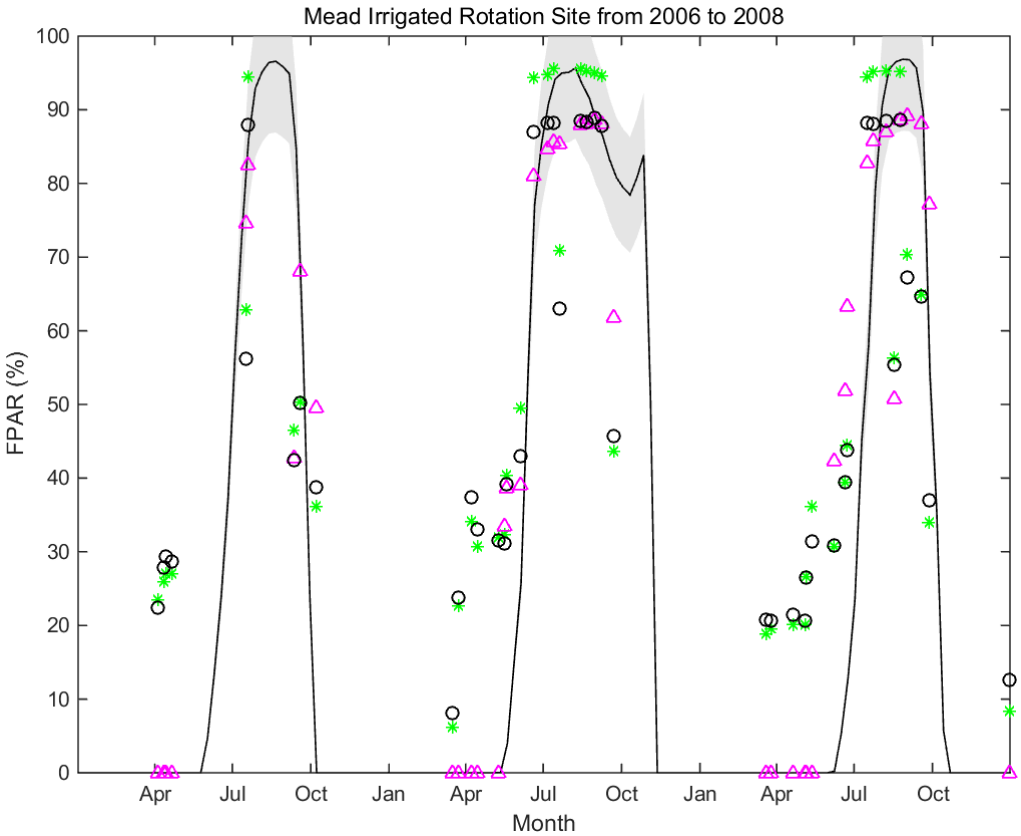
Mead Irrigated Rotation Site from 2006 to 2008
FPAR (%)
Month
Apr
Jul
Oct
Jan

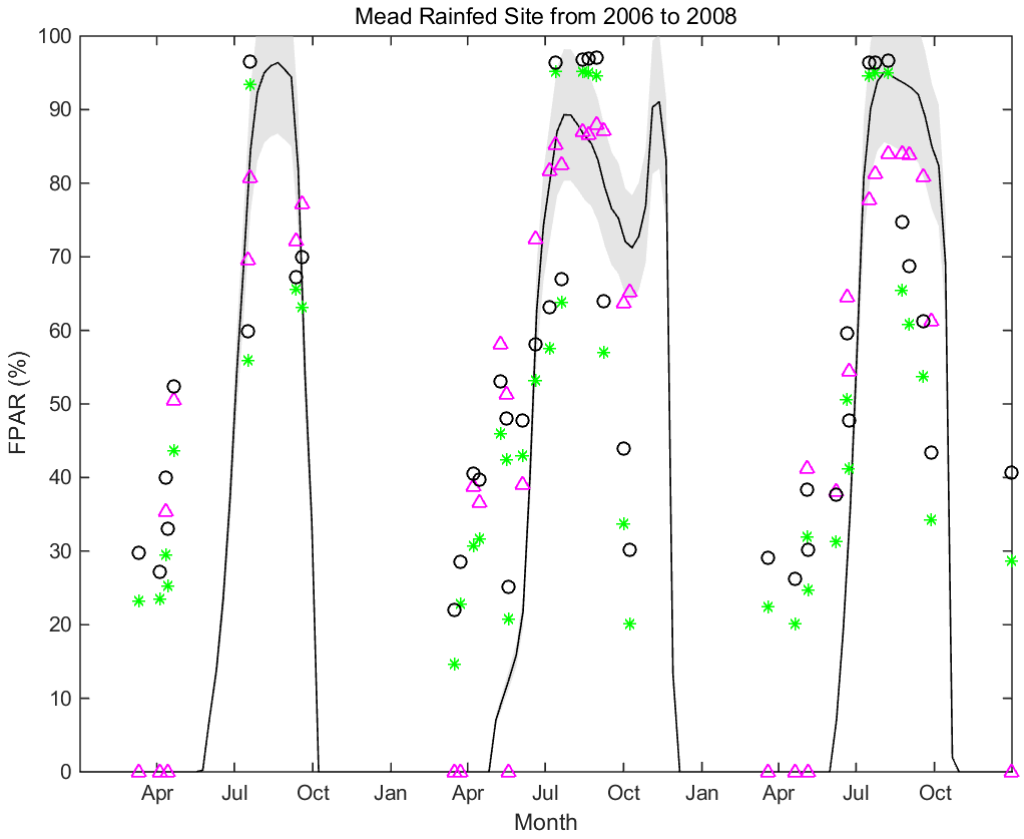
Mead Rainfed Site from 2006 to 2008
FPAR (%)
Month
Apr
Jul
Oct
Jan

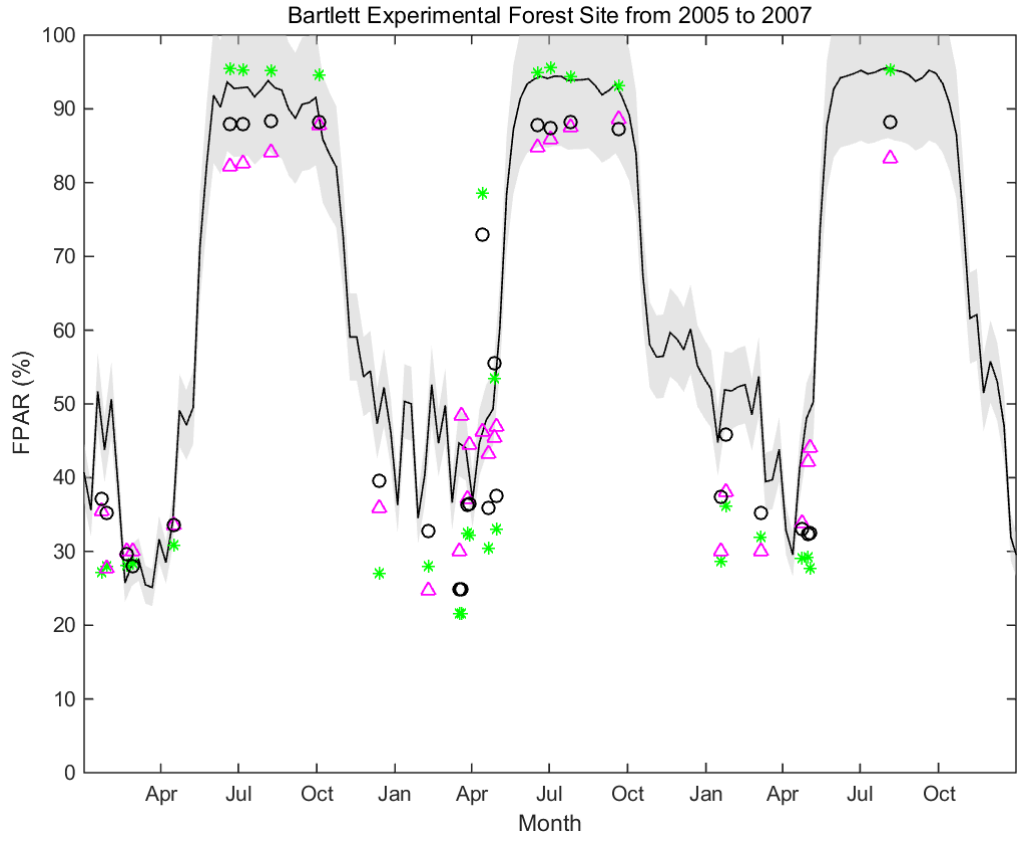
Bartlett Experimental Forest Site from 2005 to 2007
FPAR (%)
Month
Apr
Jul
Oct
Jan

Fig. 3-5 The time series of in situ measurements and the MISR FAPAR estimates from this study at four AmeriFlux sites. Green FAPAR measurements are depicted in blue line in the first panel, and total FAPAR measurements are depicted in black line in all panels. The shaded area is the 10% accuracy requirement. The "MISR" represents the MISR official FAPAR product, the MIS_4SH is the FAPAR estimate from the newly estimated LAI from this study, and MIS_4SO is the FAPAR estimate from the MISR official LAI product.

3.3.3. Validation of the FAPAR estimates from Landsat data

The Landsat surface reflectance data and land cover information were combined to estimate vegetation LAI and FAPAR values using the presented model. The LAI was estimated and then used as a parameter for FAPAR estimation. The LAI and the FAPAR estimates from the Landsat reflectance data by the presented model were validated at VALERI sites, as shown in Fig. 3-6. The Landsat LAI estimates from this study overestimated slightly compared with in situ measured LAI. The FAPAR estimates from this study had little to almost no bias and the RMSE was very low. Additionally, they had very high correlation with in situ data. It is worth to note that there were missing or invalid Landsat FAPAR values at 5 sites and MISR FAPAR values at 2 sites; thus, the retrieval rates of the Landsat FAPAR estimates was lower than that of MISR and much lower than that of MODIS with no missing values. Regarding the performances at different land covers, the Landsat FAPAR estimates performed well at grass, forest, and shrubland land cover types. However, the Landsat FAPAR estimates were not as good as the MODIS and the MISR FAPAR estimates at crop sites from this study.

The FAPAR estimates from the Landsat data were compared with the in situ measured FAPAR at four AmeriFlux sites, as shown in Fig. 3-7. The errors of the FAPAR estimates from the Landsat data validated with in situ measurements are listed in the last row of each site in Table 3-3. The Landsat FAPAR estimates had good performances at the Mead Irrigated Rotation and the Bartlett site, and comparable performance as the MODIS and MISR FAPAR products and the MODIS and MISR FAPAR estimates from this study at the Mead Irrigated and Mead Rainfed sites. The overall R^2 at these sites is 0.76 and the bias is small, proving the feasibility of the proposed method on the high resolution data.

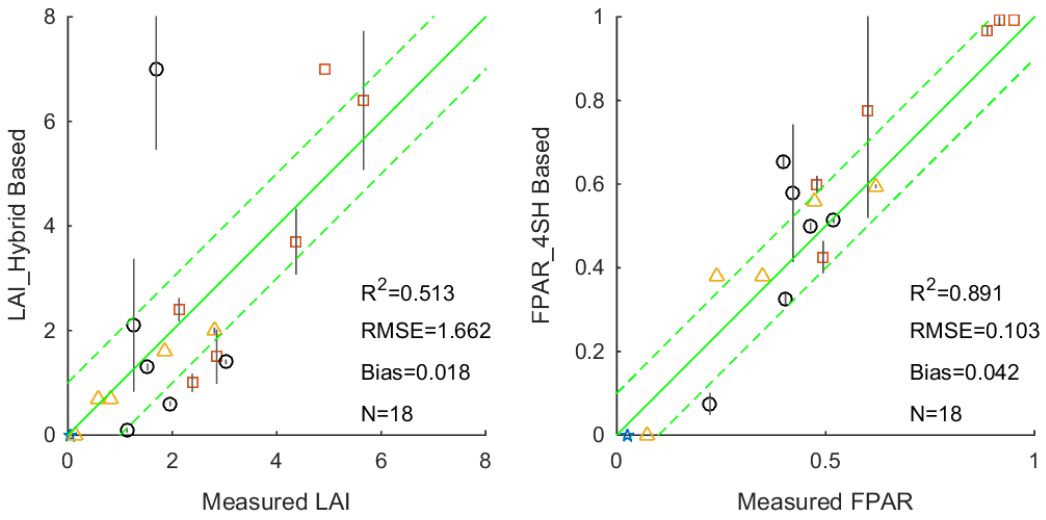

Fig. 3-6 Validation of the Landsat LAI and the FAPAR estimates from this study using in situ measurements at VALERI sites. The land cover of shrubland is represented by a pentagram (*), grass by triangle (△), forest by square (□), and crop by circle (○).Vertical bars correspond to the uncertainties (±σ). The middle green line is y = x. The other green lines are y = x ± 1.0 (left) and y = x ± 0.1 (right), respectively.

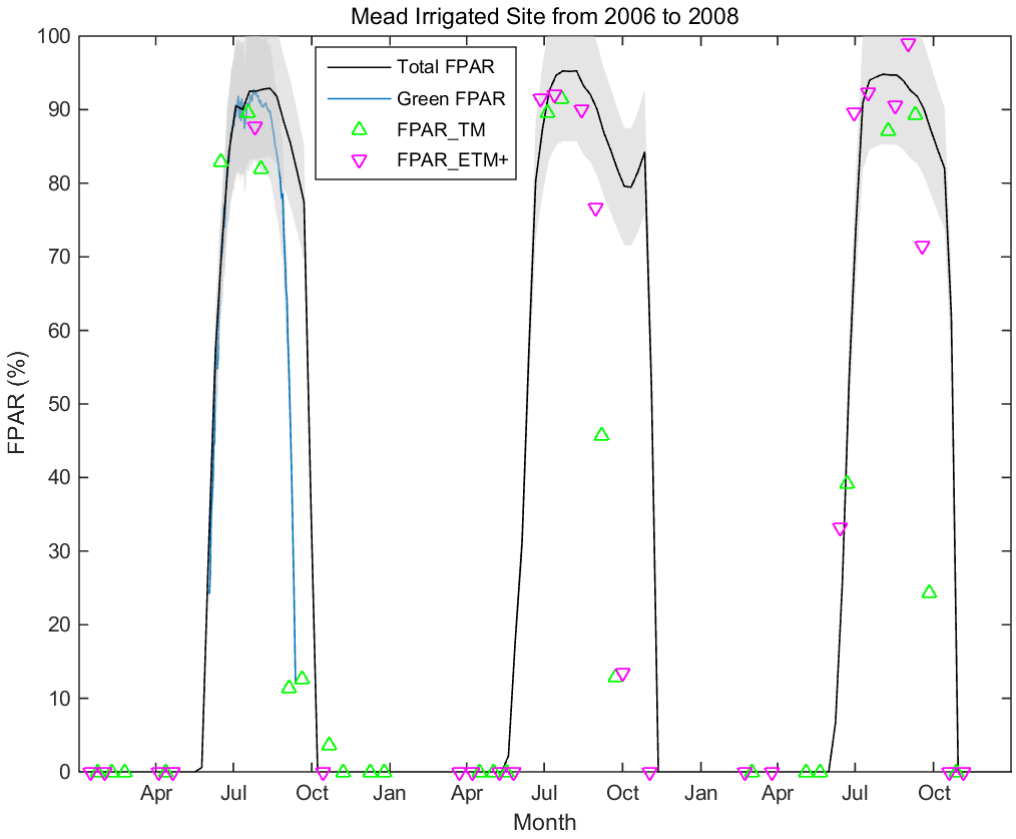
Mead Irrigated Site from 2006 to 2008
Total FPAR
Green FPAR
FPAR_TM
FPAR_ETM+
FPAR (%)
Month
Apr
Jul
Oct
Jan

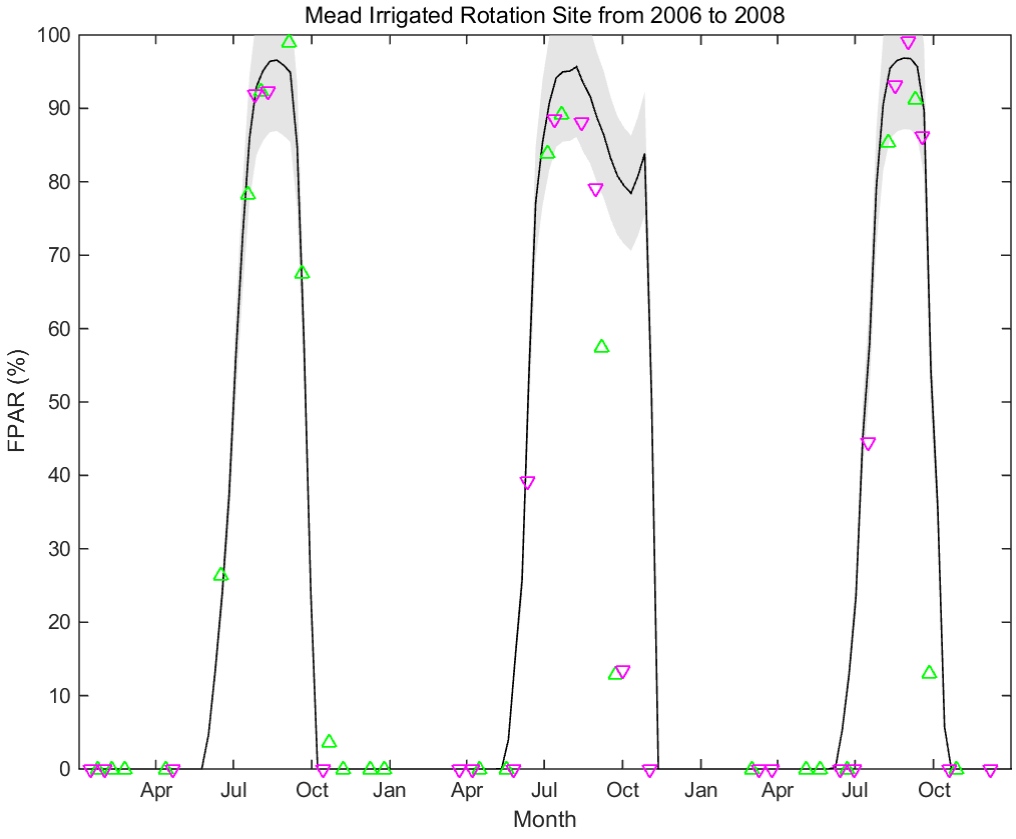
Mead Irrigated Rotation Site from 2006 to 2008
FPAR (%)
Month
Apr
Jul
Oct
Jan

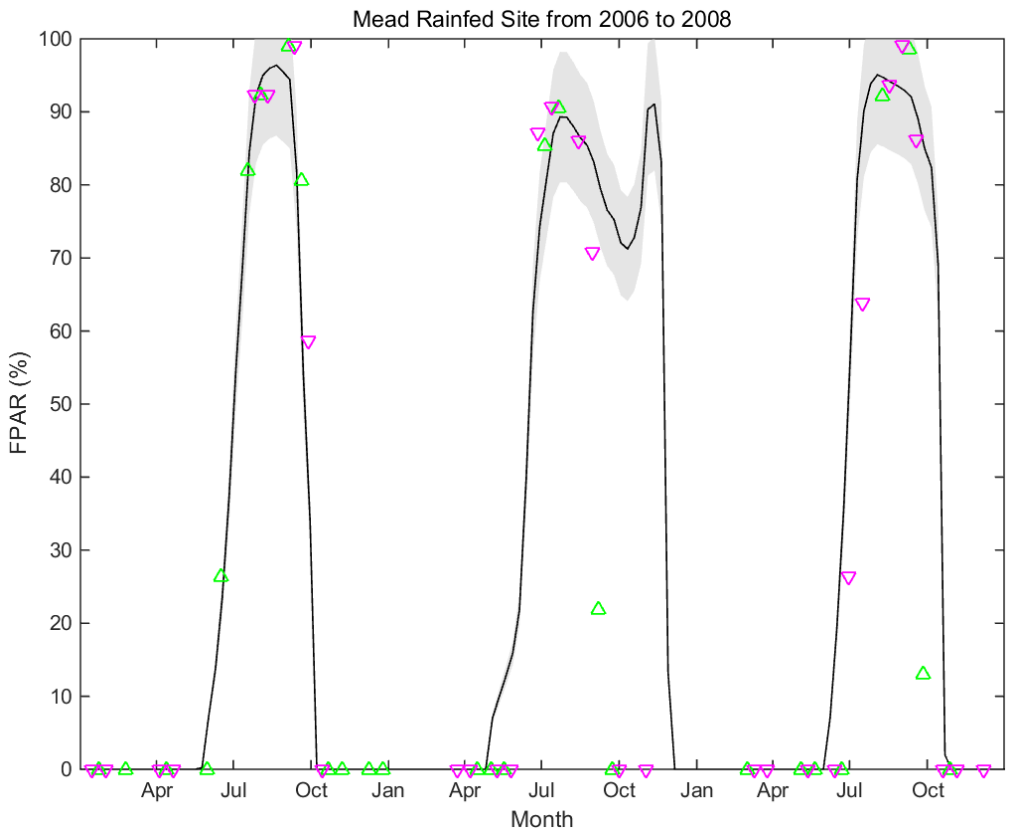
Mead Rainfed Site from 2006 to 2008
FPAR (%)
Month
0
10
20
30
40
50
60
70
80
90
100
Apr
Jul
Oct
Jan
Apr
Jul
Oct
Jan
Apr
Jul
Oct

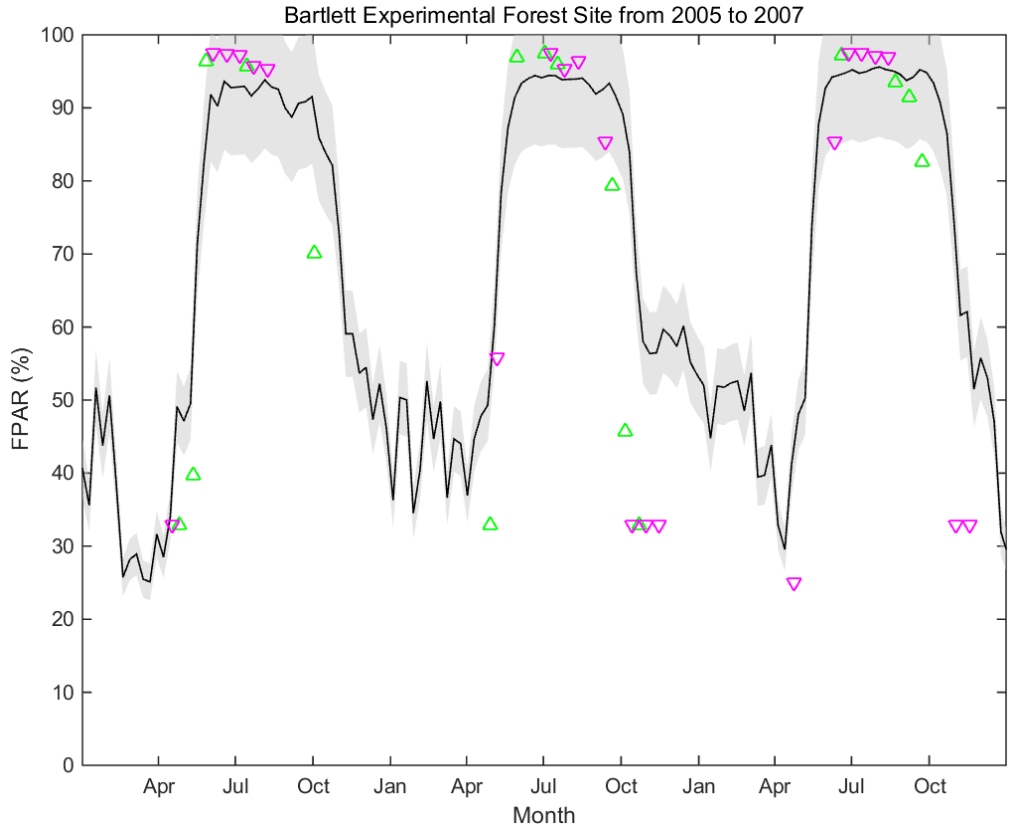
Bartlett Experimental Forest Site from 2005 to 2007
FPAR (%)
Month
0
10
20
30
40
50
60
70
80
90
100
Apr
Jul
Oct
Jan
Apr
Jul
Oct
Jan
Apr
Jul
Oct

Fig. 3-7 The time series of in situ measurements and the FAPAR estimates from Landsat at four AmeriFlux sites. Green FAPAR measurements are depicted in blue line in the first panel, and total FAPAR measurements are depicted in black line in all panels. The shaded area is the 10% accuracy requirement. The FAPAR_TM represents the FAPAR estimates from the Landsat TM sensor, and the FAPAR_ETM+ represents the FAPAR estimates from the Landsat ETM+ sensor.

3.4. Application at the regional scale

Section 3.3 assessed the FAPAR estimates from this study with some reference FAPAR prodcuts and in situ measured FAPAR at the site scale. This section applied the model to estimate FAPAR values from multiple satellite data with different spatial-resolutions, and compared the results with official FAPAR products at the regional scale to make a comprehensive analysis. Two study regions covering four AmeriFlux sites were selected and their geographic locations are shown in Fig. 3-8 (a). The specific MODIS tiles and MISR and Landsat orbits containing the two study regions are listed in Table 3-4. The temporal resolutions of the MISR, the MODIS, and the Landsat TM/ETM+ reflectance or FAPAR products are 2–9 days, 8 days, and 16 days, respectively. The MISR, the MODIS, and the Landsat scenes around the four AmeriFlux sites in the vegetation growing season were carefully selected so that they had closest imaging dates as well as high quality data without cloud contamination. It turned out that the imaging dates of the products in each case differed within 4 days (Table 3-4). We assumed that the vegetation remained almost unchanged within this

short period so that the intercomparison of FAPAR among different sensors was reliable.

The Landsat reflectance data were atmospherically corrected using Landsat Ecosystem Disturbance Adaptive Processing System (LEDAPS) preprocessing code. Missing scan lines in the ETM+ image were filled with values of nearest pixels. The 30 m spatial resolution Landsat TM and ETM+ surface reflectance scenes are illustrated in Fig. 3-8 (b) and (c), respectively. They were used for FAPAR estimation at 30 m spatial resolution. The MISR and MODIS surface reflectance products (MISR L2 and MOD09) were directly used for FAPAR estimation at 1100 m and 500 m spatial resolutions. The MISR and the MODIS FAPAR products (MISR L2 and MOD15) were intended for intercomparison with the FAPAR estimates from this study.

The MODIS FAPAR product uses MCD12 land cover product to distinguish among 13 land covers globally. The National Land Cover Database 2006 (NLCD 2006) uses a 16-class land cover classification scheme for Landsat images. A combined land cover classification scheme of the two was used considering the existing land covers in the two study regions. The MISR, MODIS, and Lansat images were classified into evergreen forest, deciduous forest, urban, grass, crops, barren soil, and water body. The classified images and surface reflectance images were combined to estimate vegetation LAI and FAPAR values using the presented model, with input parameters of soil background and leaf canopy albedo from a database introduced in Section 3.2. The LAI was estimated first and then used as a parameter for FAPAR estimation. Distributions of the LAI and the FAPAR estimates in the MISR, MODIS, and

Landsat images in Case 1 are shown in Fig. 3-9 (a–c) and Fig. 3-10 (a–c), respectively. As comparisons, the MISR and the MODIS LAI and FAPAR products are shown in Fig. 3-9 (d–e) and Fig. 3-10 (d–e), respectively. Distributions of the LAI and the FAPAR estimates in Cases 2 are shown in Fig. 3-12 (a–c) and Fig. 3-13 (a–c), respectively. As comparisons, the MISR and the MODIS LAI and FAPAR products are shown in Fig. 3-12 (d–e) and Fig. 3-13 (d–e), respectively. On the one hand, the MISR LAI and FAPAR products are consistently higher (> 2) than the MODIS in Case 1. The MODIS and the MISR LAI and FAPAR products agree well with each other in Case 2. On the other hand, the LAI and the FAPAR estimates from this study are consistent across different scales in both cases. They have similar distribution patterns across scales, where highest values are observed in evergreen forests, higher values in deciduous forests, and smaller values in crops, and close to zero values in rivers and central urban areas.

The frequency histograms of the MISR and the MODIS LAI and FAPAR products are shown in blue and red bars in Fig. 3-11 (c and d) and Fig. 3-14 (c and d) for Cases 1 and 2, respectively. The mean and the standard deviation of the MISR LAI product were approximately twice as large as those of the MODIS LAI product in Case 1, because of more pixels in the MISR image with values greater than 4. The MISR FAPAR product had a larger mean (> 0.15) and standard deviation than the MODIS FAPAR product in Case 1, but the relative difference between the MODIS and the MISR FAPAR products (19%) were smaller than the relative difference between the MODIS and the MISR LAI products (53%). The frequency histograms of the MISR and the MODIS LAI and FAPAR products agree well in Case 2. The difference

between the mean values of the MISR and the MODIS LAI products was slighter larger than 0.3. There is a difference of about 0.05 between the mean values of the MISR and the MODIS FAPAR products, although more pixels (> 50%) have values greater than 0.9 in the MISR FAPAR imagery than in the MODIS FAPAR imagery. The relative difference between the MISR and the MODIS FAPAR products (6%) was slightly smaller than the relative difference between the MODIS and the MISR LAI products (5%). The comparison results between the MISR and the MODIS LAI and FAPAR products in Cases 1 and 2 demonstrate that the MISR and MODIS FAPAR products agreed better with each other than the MISR and MODIS LAI products, regardless of the agreements between the MODIS and the MISR products were poor or good.

The frequency histograms of the LAI and the FAPAR estimates from the MODIS, the MISR, and the Landsat reflectance images are shown in blue, red, and green bars in Fig. 3-11 (a and b) and Fig. 3-14 (a and b) for Cases 1 and 2, respectively. Generally, the agreements among the MISR, the MODIS, and the Landsat LAI and FAPAR estimates were reasonably well. The mean values of the LAI estimates differed within 1, and corresponding standard deviations differed within 0.05 for both cases. The mean values of the FAPAR estimates differed within 0.1 and the standard deviations differed within 0.03 in both cases. Therefore, the LAI and the FAPAR estimates by the presented retrieval method had better performance than the MODIS and MISR products regarding consistency across scales. The comparable results between the estimates from this study and the products infer that the retrieval algorithms of LAI and FAPAR products could partially justify the differences in their data distributions,

so that the LAI and FAPAR values from different satellites would agree better with each other when using the same algorithm for retrieval (Seixas et al., 2009). The LAI and the FAPAR estimates from this study had comparable performance as the MODIS and the MISR FAPAR products in the study region of Case 2, where the two products had good agreements with each other. However, this study provided FAPAR estimates at multiple resolutions of 30 m, 500 m, and 1100 m, whereas the available MODIS and MISR FAPAR products are 1000 m and 1100 m, respectively.

Table 3-4 The spatial coverage and imaging date information of the MODIS, the MISR and the Landsat data used in the two cases.

Case	MODIS tile	MISR orbit	Landsat orbit	MODIS date	MISR date	Landsat date
Case 1	H10V04	P27B58	P28R31	Aug 5–12, 2006	Aug 4, 2006	Aug 3, 2006
Case 2	H12V04	P12B55	P12R29	Aug 5–12, 2005	Aug 8, 2005	Aug 8, 2005

Case 1 covers three sites: Mead Irrigated, Mead Irrigated Rotation, and Mead Rainfed. Case 2 covers Bartlett site. The “H” and “V” of MODIS tile means horizontal and vertical, respectively. The “P” and “B” of MISR orbit means path and block, respectively. The “P” and “R” of Landsat orbit means path and row, respectively.

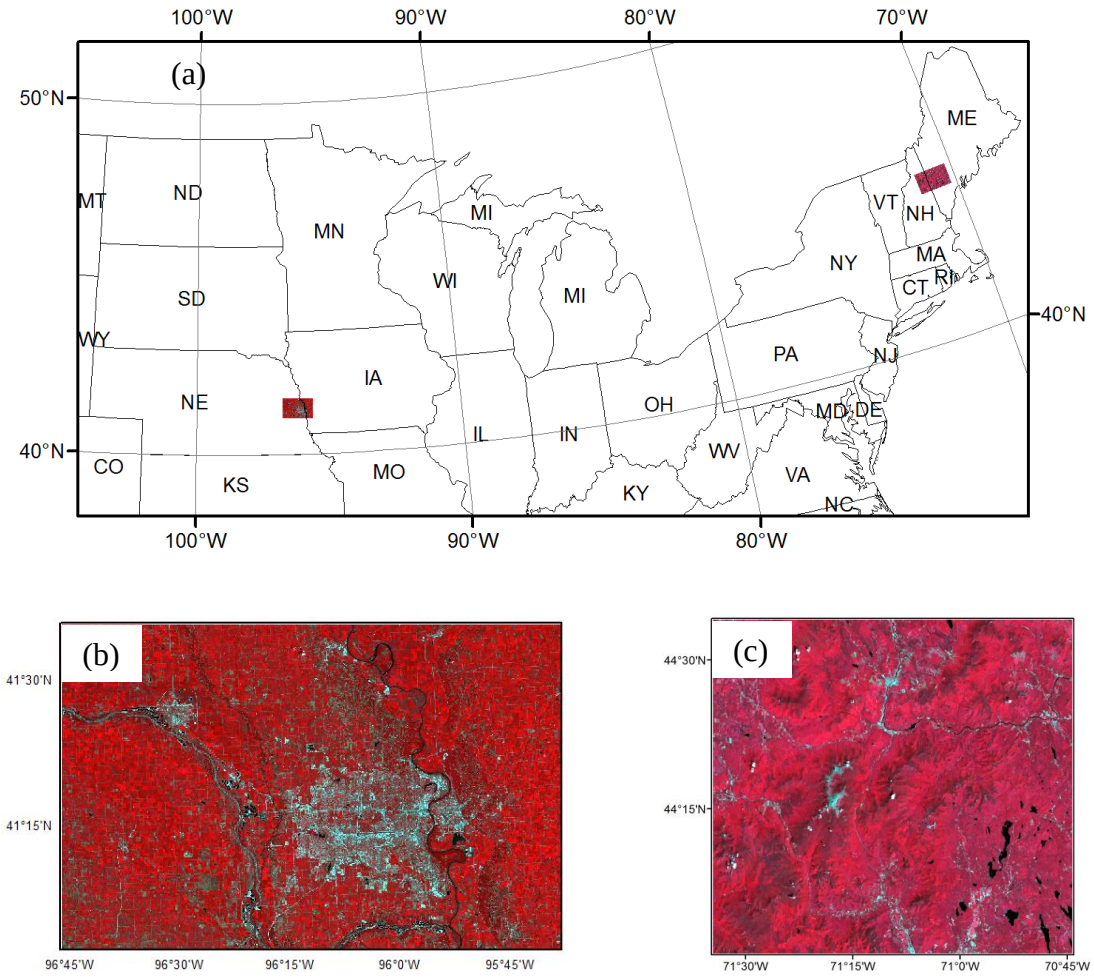

Fig. 3-8 (a) Geographic locations of the two study regions in Cases 1 and 2. The study region of Case 1 is the lower left red rectangle, and the study region of Case 2 is the upper right red rectangle. (b) The high resolution Landsat TM surface reflectance scene in Case 1 in NIR-Red-Green false color composition. (c) The high resolution Landsat ETM+ surface reflectance scene in Case 2 in NIR-Red-Green false color composition.

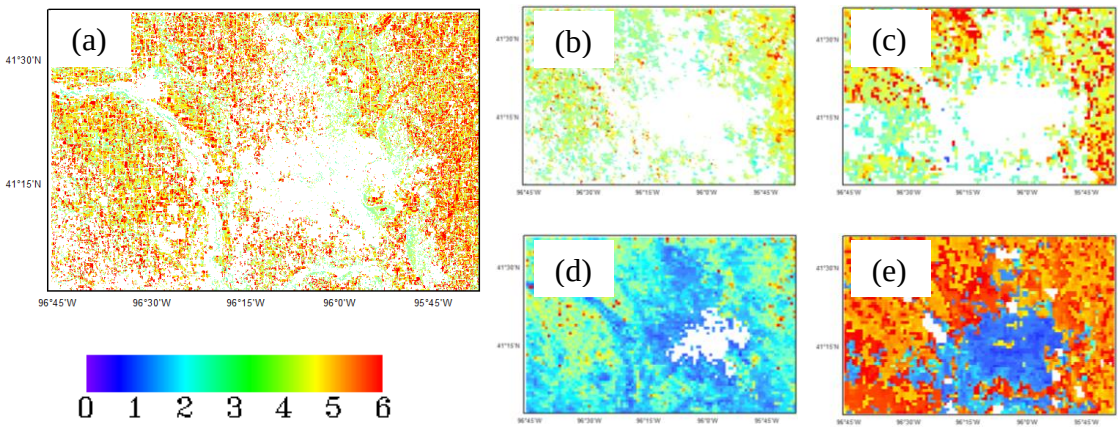

Fig. 3-9 The LAI distributions in the MISR, the MODIS, and the TM scenes in the Mead study region in Case 1. (a–c) show the TM, the MODIS, and the MISR LAI estimates from this study and (d, e) show the MODIS and the MISR LAI products.

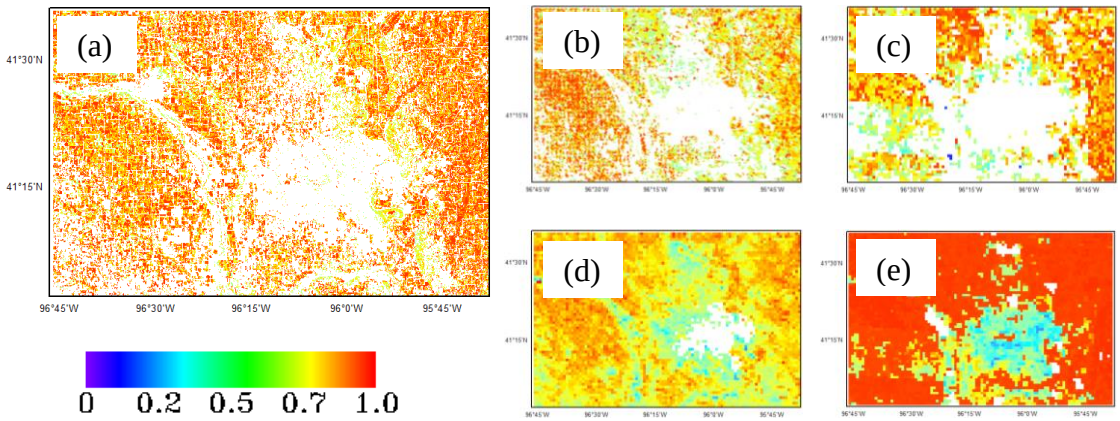

Fig. 3-10 The FAPAR distributions in the MISR, the MODIS, and the TM scenes in the Mead study region in Case 1. (a–c) show the TM, the MODIS, and the MISR FAPAR estimates from this study and (d, e) show the MODIS and the MISR FAPAR products.

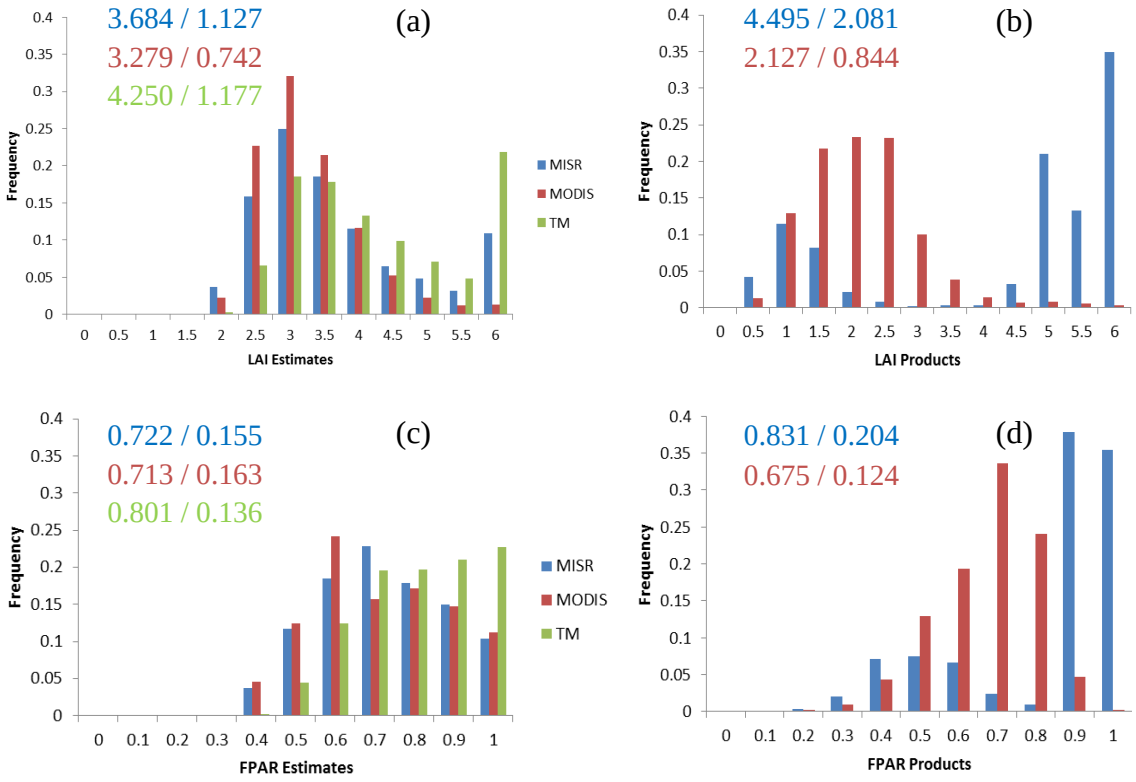

Fig. 3-11 The LAI and the FAPAR frequency histograms in the MISR, the MODIS, and the TM scenes in the Mead study region in Case 1. (a) The MISR, the MODIS, and the TM LAI estimates from this study. (b) The MISR and the MODIS LAI products. (c) The MISR, the MODIS, and the TM FAPAR estimates from this study. (d) The MISR and the MODIS FAPAR products. The numbers are the regional mean and standard deviation.

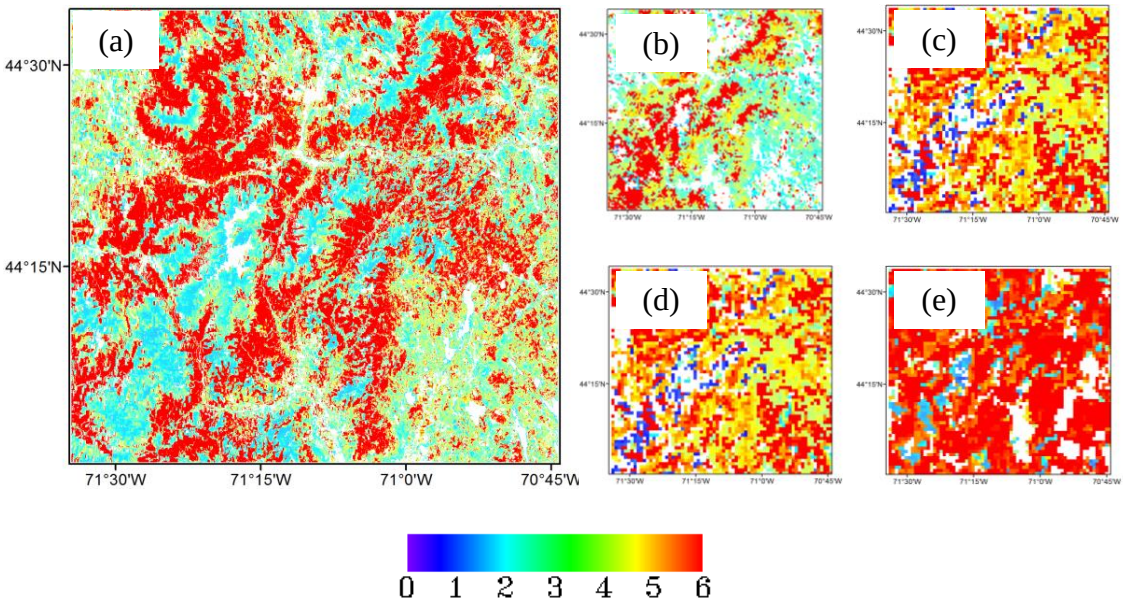

Fig. 3-12 The LAI distributions in the MISR, MODIS, and ETM+ scenes in the Bartlett region in Case 2. (a–c) show the ETM+, the MODIS, and the MISR LAI estimates from this study and (d, e) show the MODIS and the MISR LAI products.

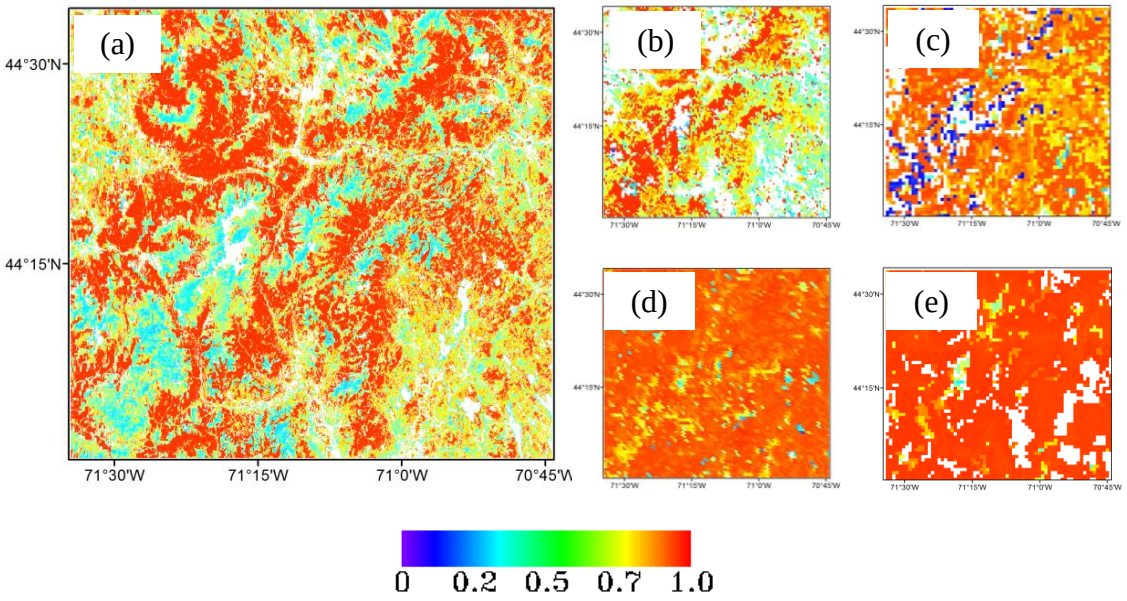

Fig. 3-13 The FAPAR distributions in the MISR, MODIS, and ETM+ scenes in the Bartlett region in Case 2. (a–c) show the ETM+, the MODIS, and the MISR FAPAR estimates from this study and (d, e) show the MODIS and the MISR FAPAR products.

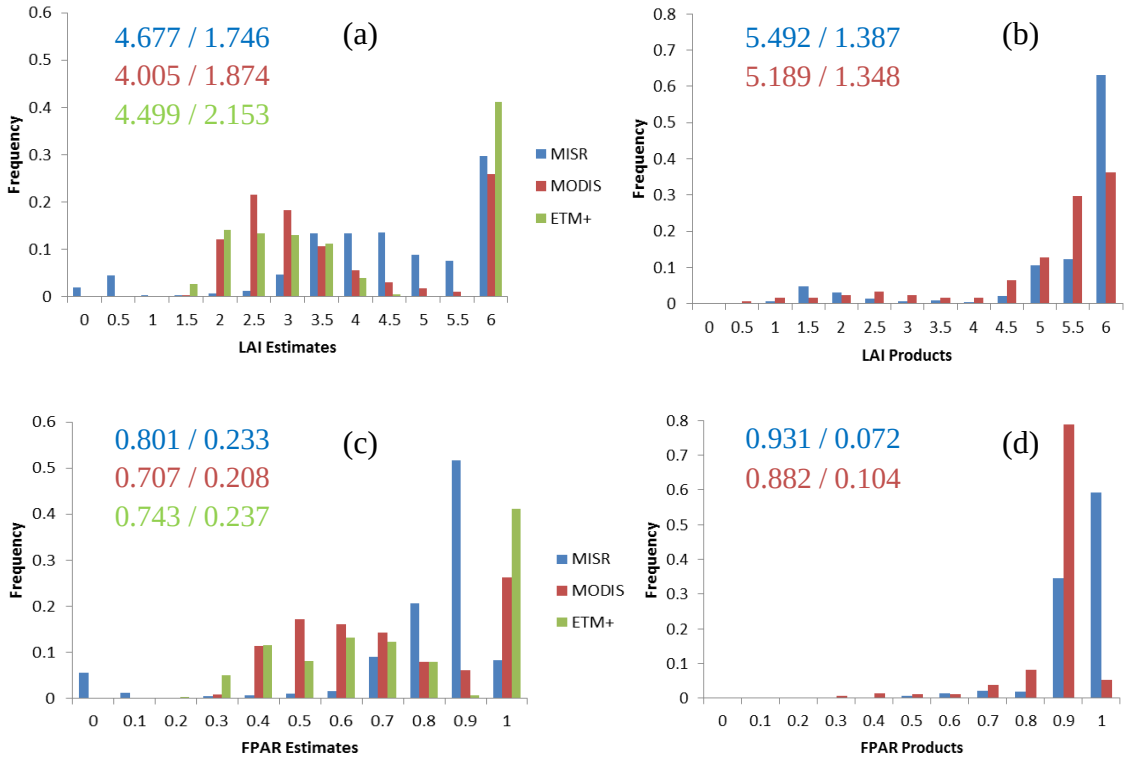

Fig. 3-14 The LAI and the FAPAR frequency histograms of the MISR, the MODIS, and the ETM+ scenes in the Mead study region in Case 1. (a) The MISR, the MODIS, and the ETM+ LAI estimates from this study. (b) The MISR and the MODIS LAI products. (c) The MISR, the MODIS, and the ETM+ FAPAR estimates from this study. (d) The MISR and the MODIS FAPAR products. The numbers are the regional mean and standard deviation.

3.5. Discussion and Conclusions

This study focuses on developing a new FAPAR model and its parameterizations to achieve an improved accuracy toward the requirement of 0.05. The FAPAR estimates by this model were compared with some reference satellite FAPAR products and validated with a comprehensive set of measurements from two field experiments, a requirement for Stage 2 of the validation (Morisette et al., 2006). Intercomparisons

and validations were conducted at site and regional scales. The site scale intercomparison and validation results demonstrated that the performances of the MODIS and MISR products varied over different land covers. Generally, the MODIS and the MISR FAPAR products performed well in shrubland and crop sites but were not that good over grass and forest land covers. This outcome was partially caused by the smaller range of in situ measured FAPAR values over crops and shrubland (a range between 0.22 and 0.74 for VALERI sites) compared with larger ranges of FAPAR values over grass (a range between 0.07 and 0.84) and forest (a range between 0.26 and 0.92). Larger ranges of FAPAR values allowed the FAPAR products to deviate greatly from the measured values used as truth data here. Additionally, the forests had a structure with the understory, the tree trunks, branches, and the leaves, resulting in complex interactions with the photons. Satellite FAPAR products had different assumptions when retrieving FAPAR over forests and thus their differences are large over forests. The finding resembles the conclusion from Pickett-Heaps et al. (2014) that FAPAR products disagree significantly with in situ values at forest sites, but have relatively high agreements at shrubland and crop sites.

The MISR and the MODIS FAPAR estimates by the new model in this study improved the performance at forest and grass sites. The growing season was successfully identified at crop sites and the time series of the FAPAR estimates was smooth over the year. The improvements were apparent at grass and forests. The RMSE was reduced from 0.16 to 0.11 for MODIS and from 0.18 to 0.1 for MISR. The improvements were attributed to both of a new model and improved inputs. The model presented is this study uses a Nilson parameter λ_0 to account for vegetation

clumping effect, but the empirical values of λ_0 had some uncertainty and could lead to inaccuracy. Forest and grass sites were generally more homogenous than the shrubland and crop sites, the latter of which may be covered by scattered natural vegetation and row crops. The Nilson parameter λ_0 for forests and grasses had lower uncertainty due to its homogeneity. Thus, the improvement on FAPAR accuracy by this model occurs generally at grass and forest land covers. As discussed, current FAPAR products did not performed well at grass and forest land covers and further improvements are needed. The model presented in this study satisfies the need to improve the performance at grass and forest land covers, and the overall accuracy was improved.

The presented model could achieve slightly better performances than the MODIS and the MISR FAPAR models when using their corresponding satellite LAI product as input, as shown in the control experiments. This study used a hybrid geometric-optic and radiative transfer model suitable for both continuous and discrete vegetation canopies to improve the LAI accuracy. The FAPAR accuracy was further improved when using these higher accuracy LAI values as input. Therefore, it is equally essential to develop new FAPAR models and improve the accuracy of model parameters, especially LAI, for improving the FAPAR accuracy.

The retrieval rate of the MODIS FAPAR estimates from this study was higher than the retrieval rate of the MISR FAPAR estimates, which was a result of more valid observations in MODIS than in MISR surface reflectance data for FAPAR retrieval. Therefore, it would be necessary to include the MODIS FAPAR estimates for a longer temporally continuous FAPAR time series analysis. However, taking into

account of multi-angular information, the accuracy of the MISR FAPAR estimates was generally better than the accuracy of the MODIS FAPAR estimates. A data fusion method could be a good solution to combine the temporal continuous advantage of the MODIS FAPAR estimates and the high accuracy advantage of the MISR FAPAR estimates given the multi-angular information.

Application of the presented model at a regional scale generated consistent FAPAR maps across multiple scales from the MODIS, the MISR and the Landsat data, with a mean difference within 0.1 and a standard deviation difference within 0.03. The MODIS and the MISR FAPAR estimates from this study had higher agreements with each other than the MODIS and the MISR FAPAR products in some study region. In addition, this study provided FAPAR estimates at three scales: 30 m, 500 m, and 1100 m, as a complement to the MODIS and the MISR FAPAR products at 1000 m and 1100 m, respectively.

Chapter 4 Integration of satellite FAPAR products

An alternative to developing new models to improve the accuracy of FAPAR estimation is to integrate multiple data products considering their characteristics and accuracy. In this chapter, two data fusion schemes were applied to integrate multiple satellite FAPAR products at two scales: optimal interpolation at the site scale and multiple resolution tree at the regional scale. The remainder of this chapter is organized as follows. Section 4.1 introduces the satellite FAPAR products and in situ measured FAPAR validation data. The principles of OI and overlapping MRT methods are briefly introduced in Section 4.2. Section 4.3 presents site-scale data fusion results using OI and regional-scale data fusion results using overlapping MRT. The discussion is presented in Section 4.4.

4.1. Data

The data used in this study include satellite FAPAR products including MODIS, MERIS, and MISR ones, satellite surface reflectance data, and in situ measured FAPAR.

4.1.1. Satellite FAPAR products

Satellite FAPAR products used include the MODIS, MISR, and MERIS FAPAR products in this study. Spatial and temporal resolutions and temporal coverage information of satellite FAPAR products, as well as their retrieval algorithms, are listed in Table 4-1. Spatial resolutions of satellite FAPAR products vary from 1 km to 9 km, and the temporal resolutions vary from 8 days to 1 month. Spatial aggregation

and temporal interpolation are necessary to compare and integrate their values across multiple scales. Considering the availability of continuous FAPAR measurements, temporal values of FAPAR products were linearly interpolated to the highest temporal resolution to ensure sufficient data points were validated with in situ measurements.

4.1.2. Satellite surface reflectance

The MODIS, MISR, Landsat Thematic Mapper (TM), and Enhanced Thematic Mapper Plus (ETM+) reflectance data were used for FAPAR estimation using the algorithm presented and validated in Tao et al. (In review). The satellite surface reflectance data for FAPAR retrieval listed in Table 3-1 were used to generate multiple-scale FAPAR maps. Different spatial resolutions of FAPAR estimates could induce the scaling effect of FAPAR, which happens when the surface is heterogeneous and the retrieval algorithm is nonlinear (Tao et al., 2009; Xu et al., 2009). Because of the scale difference, the validation results at more homogeneous sites are expected to have a higher FAPAR accuracy. We evaluate the heterogeneity around the validation sites in Chapter 2. The FAPAR accuracy at different sites is analyzed and the impact of site heterogeneity on the FAPAR accuracy is explored.

4.1.3. In situ measured FAPAR

The FAPAR validation data were collected from two groups of experimental sites: validation of land European remote sensing instruments (VALERI, WWW1) and AmeriFlux (WWW2) (Morisette et al., 2006). The VALERI sites are widely distributed around the world and are useful for spatial validation over different land

covers. The AmeriFlux sites are intended for temporal validation of FAPAR products and integrations, in view of their continuous measurements of FAPAR. The land covers of the 28 VALERI and AmeriFlux sites include 9 forests (1 of Ameriflux and 8 of VALERI), 12 crops (3 of Ameriflux and 9 of VALERI), 6 grass sites (of VALERI), and 1 shrubland site (of VALERI). Their distributions are shown in Fig. 2-1. The geolocation and land cover information of the AmeriFlux and the VALERI sites are listed in Table 2-1.

Table 4-1 The characteristics of moderate-resolution satellite FAPAR products used in this study.

FAPAR product	Temporal coverage	Temporal resolution	Spatial resolution	Projection	Algorithm
MODIS (MOD15 C5) (WWW3)	Feb 18, 2000–	8 days	1000 m	Sinusoidal	Look up table method built on 3D stochastic radiative transfer model for different biomes (Myneni et al., 2002).
MISR (L2) (WWW4)	Feb 24, 2000–	Equator: 9 days, Polar: 2 days	1100 m	Space Oblique Mercator	Radiative transfer (RT) model with inputs of LAI and soil reflectance

					without assumptions on biomes (Knyazikhin et al., 1998a).
MERIS (L3) (WWW6)	Apr 1, 2002–	1 month	9000 m	Sinusoidal	Polynomial formula based on 1D RT model (Gobron et al., 1999).

4.2. Methods

The satellite FAPAR products and the generated FAPAR estimates in Section 4.1 were integrated using two schemes to improve the FAPAR accuracy. Optimal interpolation was used to integrate the FAPAR products at the site scale, and the multiple resolution tree was used to integrate the FAPAR estimates at the regional scale. These two methods are introduced in Subsections 4.2.1 and 4.2.2, respectively.

4.2.1. Optimal Interpolation

The OI was chosen to integrate the FAPAR values from different sources because of its simplicity and ability to generate optimal estimates when the estimated noise accurately reflects the level of actual noise in the data (Gu et al., 2006). Denoting the individual satellite FAPAR product as F_i (i = 1,2,3) with error σ_i (i = 1,2,3) and the integrated FAPAR as F_a with error σ_a, the optimal integration was estimated from a linear combination of the individual products:

$$F_a = a_1F_1 + a_2F_2 + a_3F_3 \ , \ a_1 + a_2 + a_3 = 1 \tag{1}$$

Assuming the integration is unbiased: $\overline{F_a} = \overline{F_t}$. F_a is the best estimate of F_t, if the coefficients a_1, a_2, and a_3 are chosen to minimize the mean squared error of F_a:

$$\sigma_a^2 = \overline{(F_a - F_t)^2} = \overline{\left[a_1\left(F_1 - F_t\right) + a_2\left(F_2 - F_t\right) + \left(1 - a_1 - a_2\right)\left(F_3 - F_t\right)\right]^2} \tag{2}$$

The minimization of σ_a^2 with respect to a_1 gives:

$$\frac{\partial \sigma_a^2}{\partial a_1} = \overline{2\left[a_1\left(F_1 - F_t\right) + a_2\left(F_2 - F_t\right) + \left(1 - a_1 - a_2\right)\left(F_3 - F_t\right)\right]\left[\left(F_1 - F_t\right) - \left(F_3 - F_t\right)\right]} = 0$$

$$\Rightarrow a_1\sigma_1^2 - \left(1 - a_1 - a_2\right)\sigma_3^2 = 0 \tag{3}$$

Similarly, $a_2\sigma_2^2 - \left(1 - a_1 - a_2\right)\sigma_3^2 = 0$, combining with (3), we get $a_1 = \dfrac{\sigma_2^2\sigma_3^2}{\sigma_2^2\sigma_3^2 + \sigma_1^2\sigma_3^2 + \sigma_1^2\sigma_2^2}$ and $a_2 = \dfrac{\sigma_1^2\sigma_3^2}{\sigma_2^2\sigma_3^2 + \sigma_1^2\sigma_3^2 + \sigma_1^2\sigma_2^2}$, thus

$$FPAR_a = \frac{F_1/\sigma_1^2 + F_2/\sigma_2^2 + F_3/\sigma_3^2}{1/\sigma_1^2 + 1/\sigma_2^2 + 1/\sigma_3^2} \tag{4}$$

Replacing a_1 and a_2 back into (2), we get

$$\sigma_a^2 = a_1^2\sigma_1^2 + a_2^2\sigma_2^2 + \left(1 - a_1 - a_2\right)^2\sigma_3^2 = \frac{\sigma_1^2\sigma_2^2\sigma_3^2}{\sigma_2^2\sigma_3^2 + \sigma_1^2\sigma_3^2 + \sigma_1^2\sigma_2^2} < \sigma_1^2, \sigma_2^2, \sigma_3^2$$

$$\text{or, } \frac{1}{\sigma_a^2} = \frac{1}{\sigma_1^2} + \frac{1}{\sigma_2^2} + \frac{1}{\sigma_3^2} \tag{5}$$

The error of individual satellite FAPAR products can be determined from the root mean square error (RMSE) when comparing products with in situ measurements. The precision of the integrated FAPAR is the sum of the precisions of individual products if the statistics of the errors reflects the level of actual noise in the data accurately.

4.2.2. Multiple Resolution Tree

The MRT was used to integrate the data at the regional scale because of its computational efficiency compared with other fusion methods such as OI. MRT considers data continuity at multiple scales and generates multi-scale data simultaneously. It is useful for predicting optimally at multiple resolutions (Huang et al., 2002). Suppose that we want to predict **y** from observation **z**. **y** has several layers that have a hierarchical relation, such as parents, self, and children layers. The relation between self and parent layers and the relation between observation $\mathbf{z}_u$ and prediction $\mathbf{y}_u$ at node u of a directed tree are:

$$\begin{aligned} \mathbf{y}_u &= \mathbf{A}_u \mathbf{y}_{\mathrm{pa}(u)} + \mathbf{w}_u \\ \mathbf{z}_u &= \mathbf{C}_u \mathbf{y}_u + \boldsymbol{\varepsilon}_u \end{aligned} \tag{6}$$

where $\mathbf{A}_u$ is the state conversion matrix that estimates the variable at node u from its parent layer, and $\mathbf{C}_u$ is the observation matrix that coverts the variable of interest to the satellite data. Both the variable and the satellite data are FAPAR, and hence, the observation matrix $\mathbf{C}_u$ is set to be identity matrix. $\mathbf{w}_u$ and $\boldsymbol{\varepsilon}_u$ are independent, zero-mean Gaussian vectors with covariance matrices $\mathbf{W}_u$ and $\boldsymbol{\Phi}_u$. Covariance between any two nodes $\mathbf{y}_u$ and $\mathbf{y}_{u'}$ on the tree can be computed recursively along the paths from their common ancestor, $\mathrm{an}(u,u')$:

$$\operatorname{cov}\left(\mathbf{y}_u, \mathbf{y}_{u'}\right) = \mathbf{A}_{u_1}\mathbf{A}_{u_2}\ldots\mathbf{A}_u \operatorname{var}\left(\mathbf{y}_{\operatorname{an}(u,u')}\right)\left(\mathbf{A}_{u_1'}\mathbf{A}_{u_2'}\ldots\mathbf{A}_{u'}\right)' \tag{7}$$

where $\left(\operatorname{an}\left(u,u'\right),u_1,u_2,\ldots,u\right)$ and $\left(\operatorname{an}\left(u,u'\right),u_1',u_2'\ldots,u'\right)$ are two paths from $\operatorname{an}\left(u,u'\right)$ to u and u', respectively. The variance of $\mathbf{y}_u$ is:

$$\mathbf{V}_u = \operatorname{var}(\mathbf{y}_u) = \mathbf{A}_u\mathbf{V}_{\operatorname{pa}(u)}\mathbf{A}_u' + \mathbf{W}_u \tag{8}$$

Note that the variance of $\mathbf{y}_u$ can be calculated recursively as well. Generally, MRT involves two steps: leaf-to-root Kalman filtering and root-to-leaf Kalman smoothing. In the leaf-to-root filtering step, using Bayes' theorem for multivariate Gaussian prior and data processes, we have:

$$\begin{aligned}\mathbf{y}_{u|u} &= \mathbf{V}_u\mathbf{C}_u'\left(\mathbf{C}_u\mathbf{V}_u\mathbf{C}_u' + \mathbf{\Phi}_u\right)^{-1}\mathbf{z}_u \\ \mathbf{\Gamma}_{u|u} &= \mathbf{V}_u - \mathbf{V}_u\mathbf{C}_u'\left(\mathbf{C}_u\mathbf{V}_u\mathbf{C}_u' + \mathbf{\Phi}_u\right)^{-1}\mathbf{C}_u\mathbf{V}_u\end{aligned} \tag{9}$$

The root-to-leaf smoothing step moves from the root to the leaves in the direction of the edges. Finally, the prediction **y** is calculated as:

$$\begin{aligned}\mathbf{y}_u &= \mathbf{y}_{u|u} + \mathbf{\Gamma}_{u|u}\mathbf{B}_u'\mathbf{\Gamma}^{-1}_{\operatorname{pa}(u)|u}\left(\mathbf{y}_{\operatorname{pa}(u)} - \mathbf{y}_{\operatorname{pa}(u)|u}\right) \\ \mathbf{B}_u &= \mathbf{V}_{\operatorname{pa}(u)}\mathbf{A}_u'\mathbf{V}_u^{-1}\end{aligned} \tag{10}$$

The concept of overlapping trees is applied on the Kalman smoothing process to generate smooth estimates (Irving et al., 1997). The overlapping regions have averaged values of the neighboring pixels with gradually changed weights. Suppose there are two layers P and Q at two adjacent scales, and it is desired to interpolate pixel values from layer P to layer Q. The overlapping regions for two pixels P (*m*,*n*)

and P (m,n+1) in layer P correspond to an extent of, e.g., 4 pixels in layer Q, which are expected to a take on a transitional role. The values of the transitional pixels are associated with the gradually decreased contribution weight of the left pixel P (m,n), e.g., from 0.8, 0.6, 0.4, to 0.2, and the gradually increased weight of the right pixel P (m,n+1), e.g., from 0.2, 0.4, 0.6, to 0.8. Therefore, the pixel values in the vertically overlapping region in layer Q for pixels P (m,n) and P (m+1,n) in layer P can be calculated from its parent layer P as:

$$\mathrm{Q}_j = s_j \mathrm{P}(m,n) \; + \; (1-s_j)\mathrm{P}(m,n+1) \tag{11}$$

where s_j has a decreasing trend of values when j increases. The pixel values in the horizontally overlapping regions, e.g. for pixels P (m,n) and P (m+1,n), can be determined similarly. For the pixels in both the horizontal and vertical overlapping regions, such as the grids in layer Q in Fig. 4-1, their values are calculated as the weighted average of four pixels, P (m,n), P (m,n+1), P (m+1,n) and P (m+1,n+1), in its parent layer P. The weights are decided by multiplying the horizontal and vertical weights. Suppose the horizontal weight is denoted as s_j and the vertical weight is denoted as l_i, the value of pixel Q (i,j) is calculated as:

$$\mathrm{Q}_{ij} = s_j l_i \mathrm{P}(m,n) \; + \; (1-s_j) l_i \mathrm{P}(m,n+1) \; + s_j (1-l_i)\mathrm{P}(m,n+1) \; + (1-s_j)(1-l_i)\mathrm{P}(m+1,n+1) \tag{12}$$

where s_j has a decreasing trend with j, as does l_i with i.

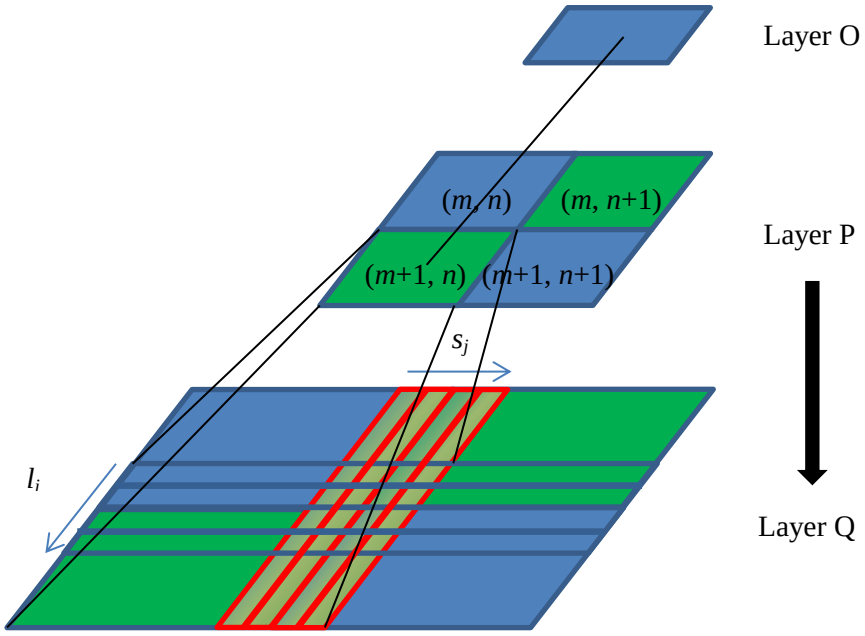

Fig. 4-1 Overlapping regions when interpolating values from layer P to layer Q at two adjacent scales.

4.3. Results

This section presents the application of the data fusion methods presented in Section 4.2 to the satellite FAPAR products and the generated FAPAR estimates in Section 4.1. First, satellite FAPAR values around the field experimental sites were extracted from satellite FAPAR products and validated with in situ measurements from VALERI and AmeriFlux sites to evaluate their accuracy. The quality controlled FAPAR values were then integrated using the presented fusion methods and validated with in situ measurements. Satellite FAPAR products were assessed with in situ measurements and the results are presented in Subsection 4.3.1. The integration results at the site and regional scale are presented in Subsections 4.3.2 and 4.3.3, respectively.

4.3.1. Assessment of FAPAR products

The quality control flags of FAPAR products if any were analyzed before validation with the in situ measured FAPAR over the VALERI and the four AmeriFlux sites. The statistics of the MODIS Collection 5 FAPAR quality control flags over the four sites are shown in Fig. 4-2. The MODIS FAPAR product had similar qualities over the three Mead sites as a result of the sites' proximity. There were more main algorithm FAPAR retrievals over the three Mead sites than over the Bartlett site. There were about 20% main algorithm retrievals under conditions of saturation over the Bartlett site and 8.7% over the VALERI sites, but no such problem existed over the Mead sites. The reason is the smaller FAPAR values over the crop sites than the forest sites.

The MODIS, MERIS and MISR FAPAR products were validated at the VALERI experimental sites, as shown in Fig. 4-3. The MERIS FAPAR product had a higher accuracy than the MODIS and MISR FAPAR products, with respect to the R^2 and RMSE at these sites. There were missing or invalid MERIS FAPAR values at five sites and MISR FAPAR values at three sites; thus, the retrieval rates of the MERIS (78.3%) and MISR FAPAR products (87.0%) were lower than that of the MODIS FAPAR product (100.0%). The MERIS FAPAR product performed well around all of the four land cover types, although it underestimated the values slightly as compared with the in situ measurements. The MODIS FAPAR products performed well at the 3crop sites. The MISR FAPAR product improved the performance at the grass and forest sites as compared with the MODIS FAPAR product. The MODIS and the

MISR FAPAR products did not rank high in terms of R^2 and RMSE, but had satisfactory biases close to zero.

The MERIS, MISR, and MODIS FAPAR products with the highest quality were used for validation with the in situ measurements at the four AmeriFlux sites (Fig. 4-4). The MISR FAPAR values were higher than the MODIS and MERIS FAPAR values, especially in the middle of the vegetation growth season. The FAPAR at the Mead Irrigated, Mead Irrigated Rotation, and Mead Rainfed sites reached zero before early April and after middle November, as a result of crop harvesting at these sites. Most satellite product values of FAPAR around the two sites approached, but were not exactly, zero at the beginning and end of the year, which may have been caused by the contribution from inhomogeneous land cover, in addition to crops near the sites, or the limited soil reflectance database used by the algorithm (Tao et al., In review). The statistics of comparisons between ground-based and space products are listed in Table 4-2. The MISR FAPAR product had the highest accuracy at the three crop sites. The MODIS and the MISR FAPAR products agreed better with the in situ measurements at the Bartlett experimental deciduous broadleaf forest site with respect to the magnitude than the MERIS FAPAR product. The MODIS FAPAR product had the lowest mean error at this site. The MERIS product has a good seasonality profile and little variation of random error caused by cloud contamination, but underestimates FAPAR by 0.12 overall. The underestimation is caused by the green leaf FAPAR estimated by MERIS versus the total FAPAR by ground-based measurements which include the absorptions of both leaf and non-leaf elements.

Table 4-2 Statistics of comparisons between ground-based and space FAPAR products at the four AmeriFlux sites.

Site	Product	RMSE	Bias	R^2
Mead Irrigated	MERIS	0.182	−0.092	0.777
	MODIS	0.145	0.009	0.667
	MISR	0.142	0.072	0.761
Mead Irrigated Rotation	MERIS	0.161	−0.036	0.751
	MODIS	0.159	0.098	0.546
	MISR	0.124	0.104	0.733
Mead Rainfed	MERIS	0.186	−0.060	0.668
	MODIS	0.143	0.070	0.626
	MISR	0.125	0.043	0.638
Bartlett	MERIS	0.127	−0.290	0.749
	MODIS	0.167	−0.085	0.642
	MISR	0.103	−0.086	0.842

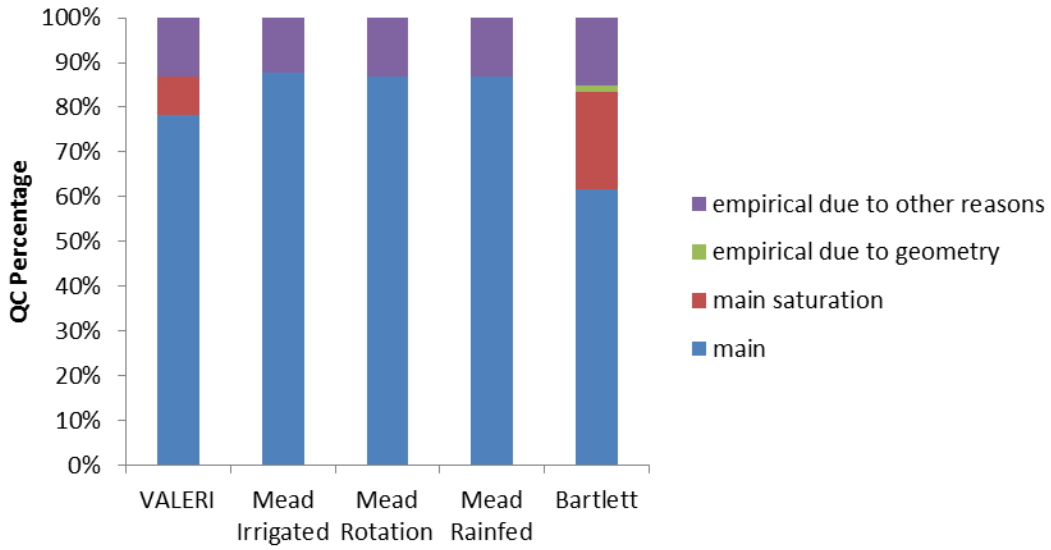

Fig. 4-2 MODIS collection 5 FAPAR QC statistics over the VALERI and the 4 AmeriFlux sites in 3 years: the percentage of main algorithm retrievals (blue), the percentage of main algorithm under conditions of saturation (red), the percentage of backup (i.e. NDVI-based) retrievals associated with bad geometry (green), the percentage of pixels using the backup algorithm due to reasons other than geometry (purple).

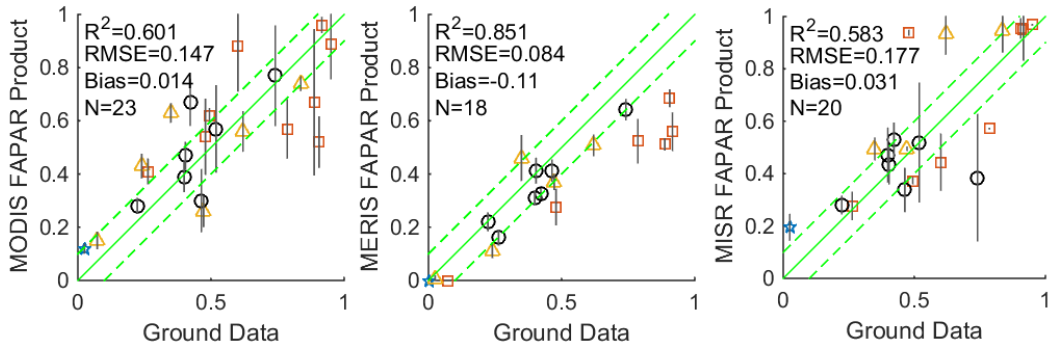

Fig. 4-3 The MODIS, the MERIS, and the MISR FAPAR products validated with in situ measurements of VALERI. The land cover of shrubland is represented by a pentagram (*), grass by triangle (Δ), forest by square (□), and crops by circle (○). Vertical bars correspond to the uncertainties (±σ). The middle black line is y = x. Two other black lines are y = x ± 0.1, respectively.

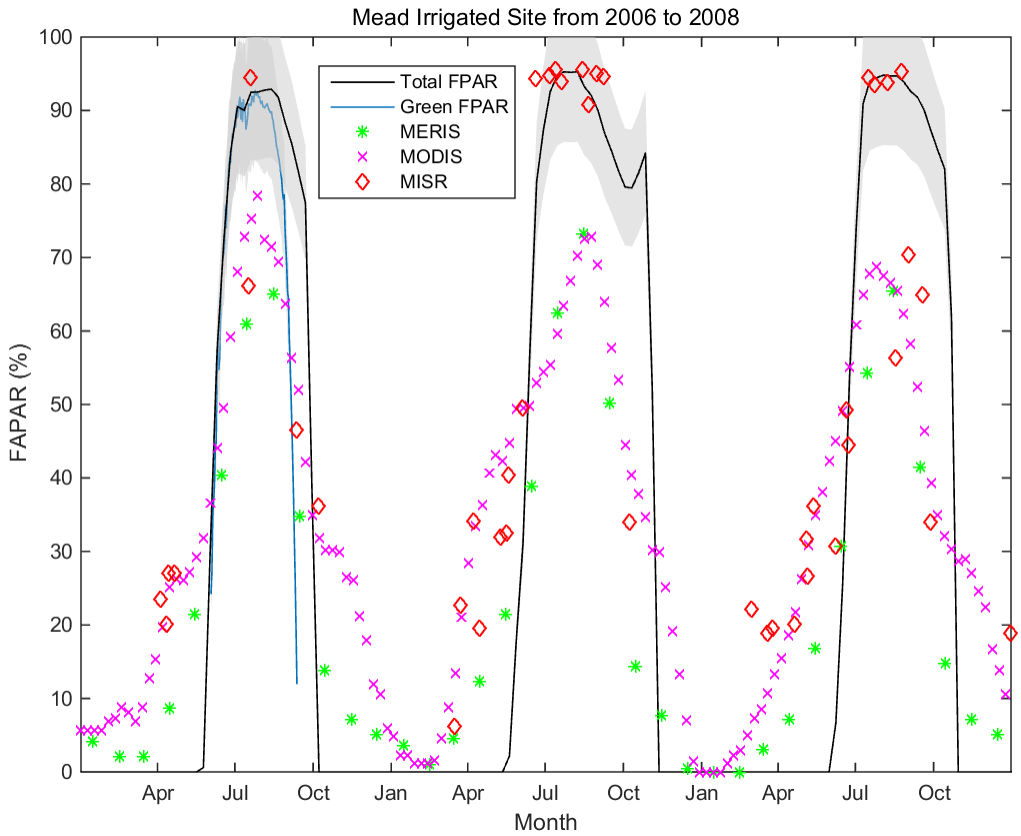

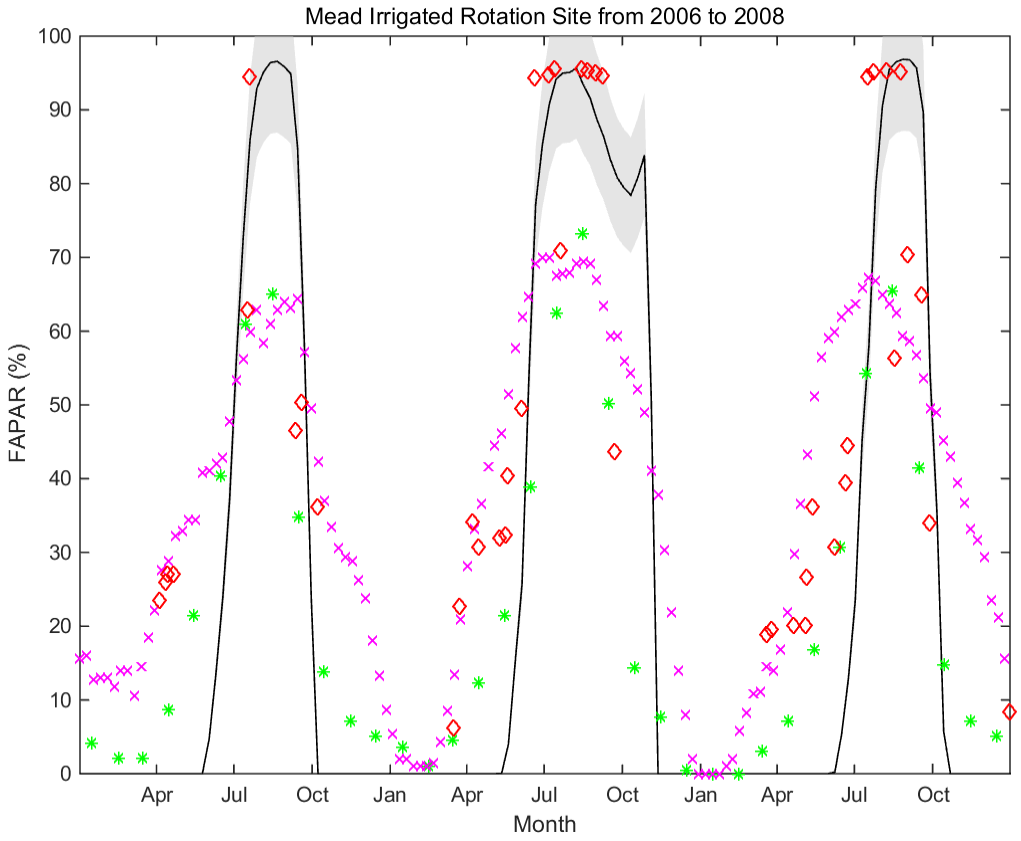
Mead Irrigated Rotation Site from 2006 to 2008
FAPAR (%)
Month
0
10
20
30
40
50
60
70
80
90
100
Apr
Jul
Oct
Jan
Apr
Jul
Oct
Jan
Apr
Jul
Oct

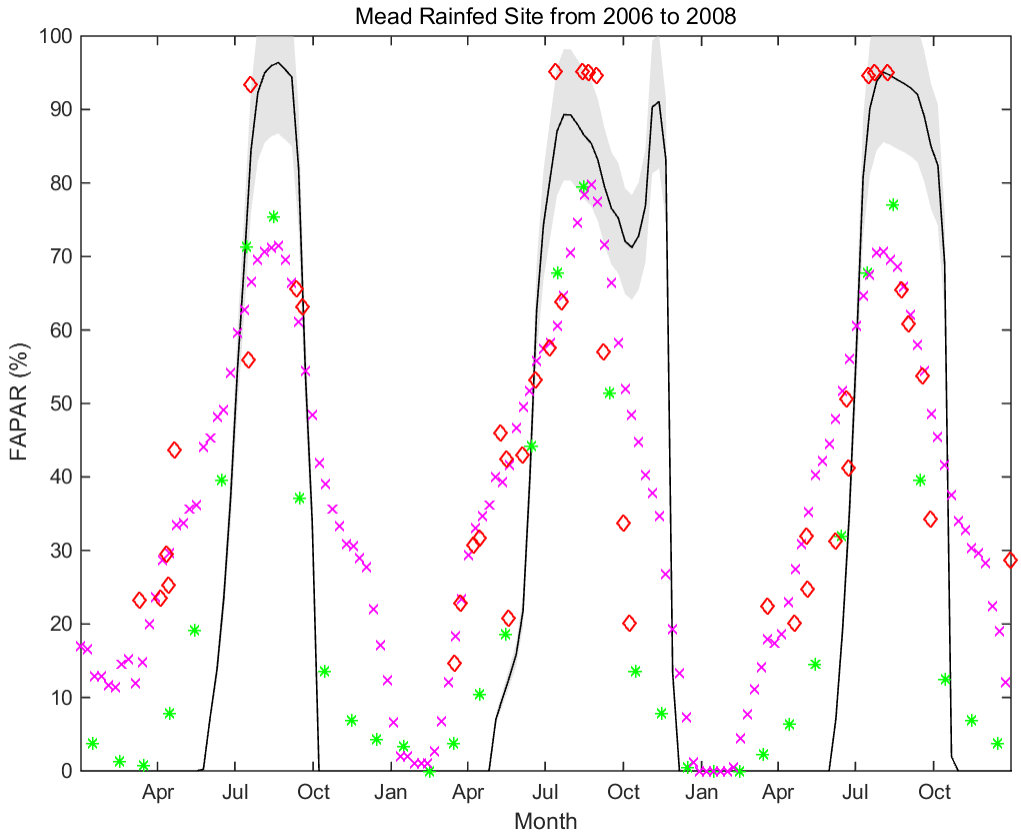
Mead Rainfed Site from 2006 to 2008
FAPAR (%)
Month
0
10
20
30
40
50
60
70
80
90
100
Apr
Jul
Oct
Jan
Apr
Jul
Oct
Jan
Apr
Jul
Oct

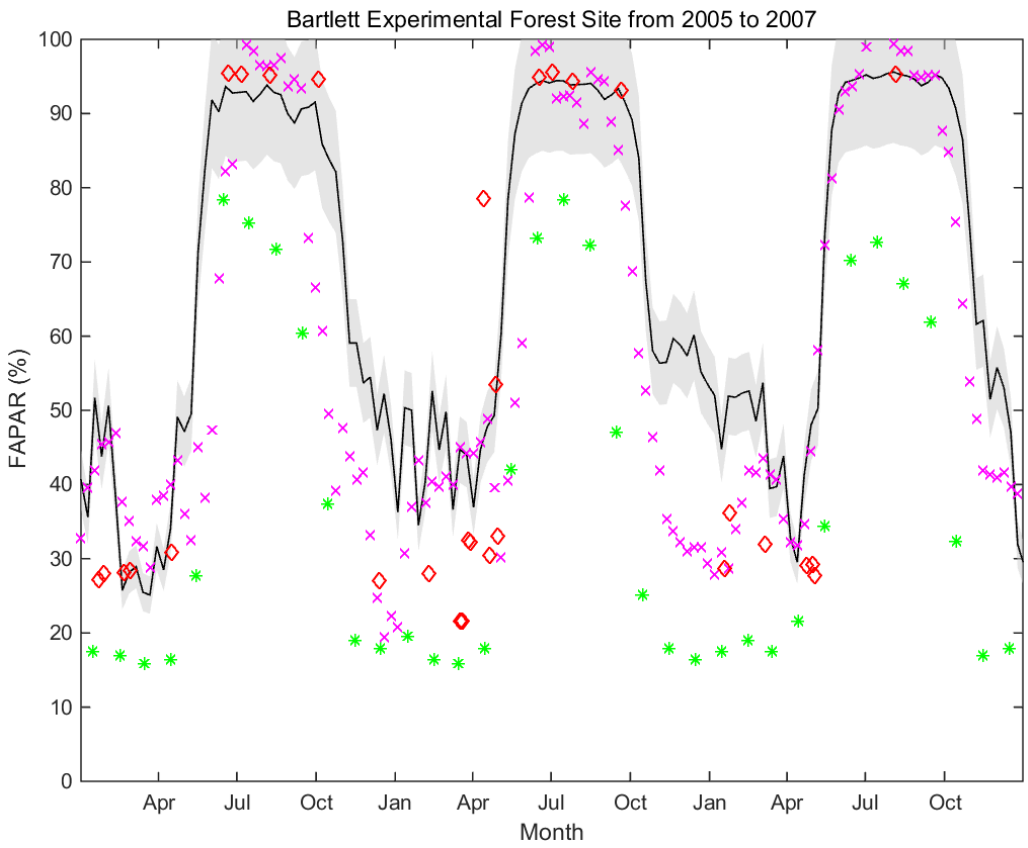

Fig. 4-4 The time series of in-situ FAPAR measurements and satellite products at four AmeriFlux sites. Green FAPAR measurements are depicted in blue line in the first panel, and total FAPAR measurements are depicted in black line in all panels. The shaded area is the 10% accuracy requirement. The monthly MERIS, 8-day MODIS, and 2–9 day MISR FAPAR products are depicted in asterisks, crosses, and diamonds, respectively.

4.3.2. Site scale fusion

The intercomparison and validation experiments discussed in Subsection 4.3.1 demonstrate that the FAPAR products performed differently for different land covers, and it is hard to draw a simple conclusion about which product was the best overall.

A fusion of various products is expected to improve the result if the statistics of the errors reflects the level of actual noise in the data accurately as noted in Section 4.2.1. The FAPAR products were integrated at the site scale using the OI method and the results are discussed in this subsection. The integration at the regional scale is presented in Subsection 4.3.3.

The values of the MODIS FAPAR product were valid at all VALERI sites, while the MERIS or the MISR FAPAR products had missing values. The valid FAPAR values of products at each site were used for integration. The biases of individual products were removed before integration. Fig. 4-5 shows a scatterplot between the integrated FAPAR using the OI method and the in situ measured FAPAR. The integrated FAPAR have no bias. The R^2 improved to around 0.9, and the RMSE was lower than those of the individual FAPAR products. The integrated FAPAR improved the accuracy of the MODIS and the MISR FAPAR products at the forest sites, overcame the underestimation problem of the MERIS FAPAR product, and had the highest accuracy among all the products as compared with the in situ measurements.

The MODIS, MISR, and MERIS FAPAR products were integrated at the four AmeriFlux sites and the integrated FAPAR was validated using the in situ measurements. The integration coefficients of the individual products were obtained from the data for the first year and then applied to other years. The comparisons of the time series curves of the integrated FAPAR and in situ measurements at the four sites are shown in Fig. 4-6. The curves of the integrated FAPAR maintained a good seasonal profile, similar to the MERIS FAPAR product, and showed the ability to detect high FAPAR values during the vegetation growing season, similar to the MISR

FAPAR product. The mean error was reduced to around 0.1 for all the four sites. The biases were reduced to less than 0.05 for the three crop sites and were removed for the Bartlett site (Table 4-3). The R^2 was improved to around 0.8 for all the four sites. It is evident that the integrated FAPAR agreed best with the in situ measurements, especially for the first half of the year.

Table 4-3 Statistics of comparisons between ground-based and integrated FAPAR at the four AmeriFlux sites.

Site	RMSE	Bias	R^2
Mead Irrigated	0.149	−0.056	0.846
Mead Irrigated Rotation	0.134	−0.053	0.860
Mead Rainfed	0.146	0.002	0.828
Bartlett	0.075	0.000	0.887

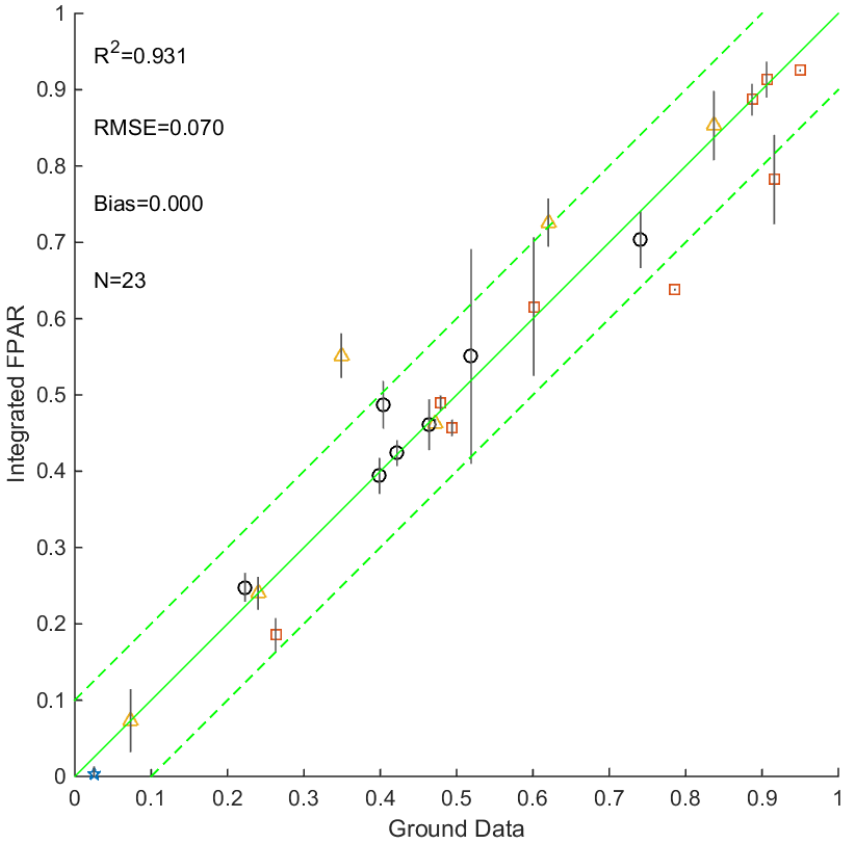

Fig. 4-5 The integrated FAPAR validated with in situ measurements of VALERI. The land cover of shrubland is represented by a pentagram (*), grass by triangle (△), forest by square (□), and crops by circle (○). Vertical bars correspond to the uncertainties (±σ). The middle green line is y = x. The two other green lines are y = x ± 0.1, respectively.

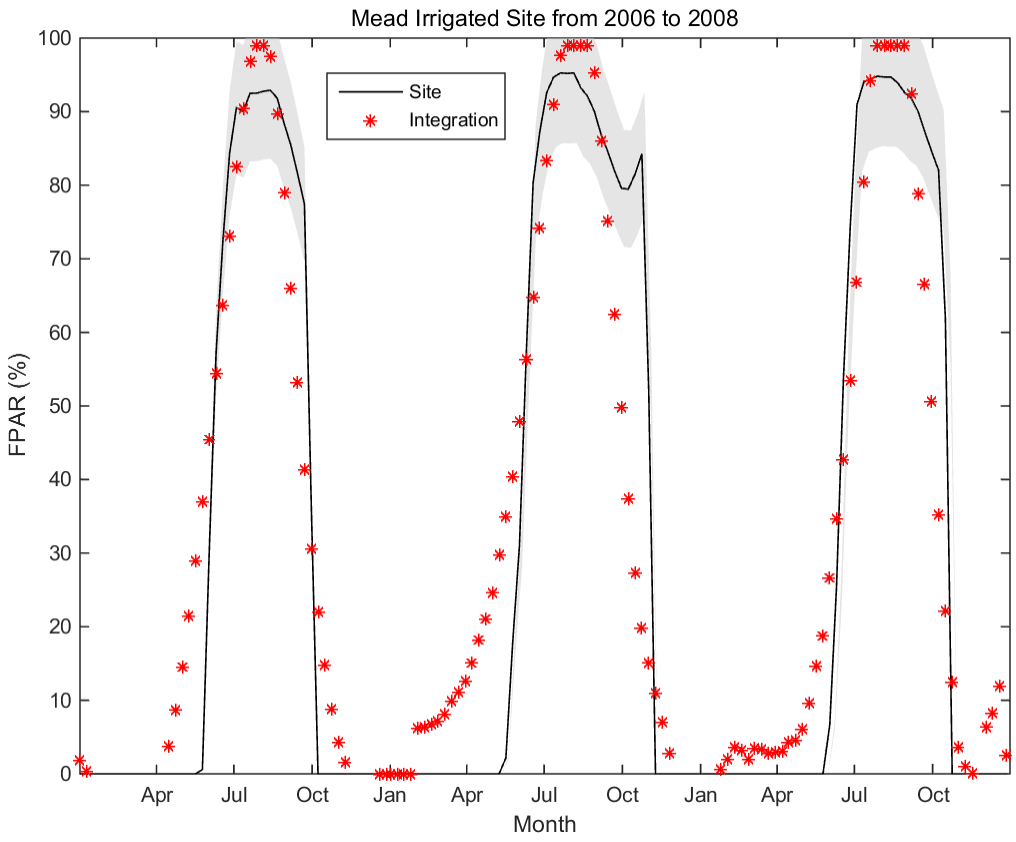
Mead Irrigated Site from 2006 to 2008
Site
Integration
FPAR (%)
Month
Apr
Jul
Oct
Jan
Apr
Jul
Oct
Jan
Apr
Jul
Oct

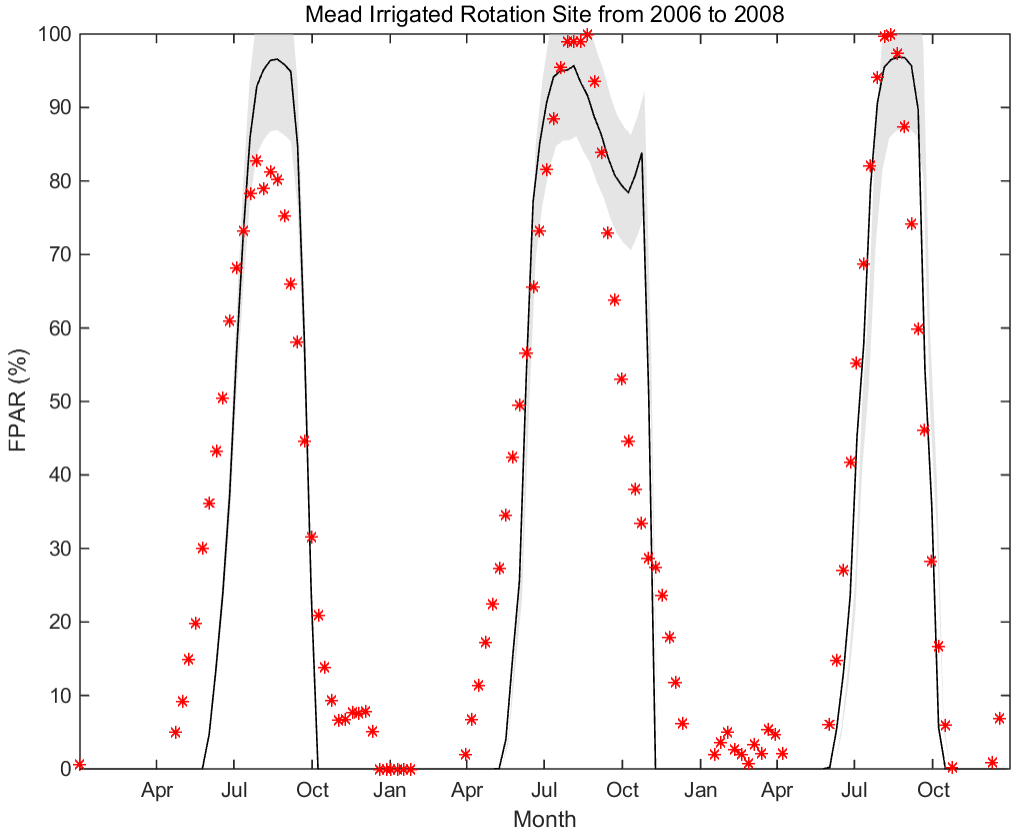
Mead Irrigated Rotation Site from 2006 to 2008
FPAR (%)
Month
Apr
Jul
Oct
Jan
Apr
Jul
Oct
Jan
Apr
Jul
Oct

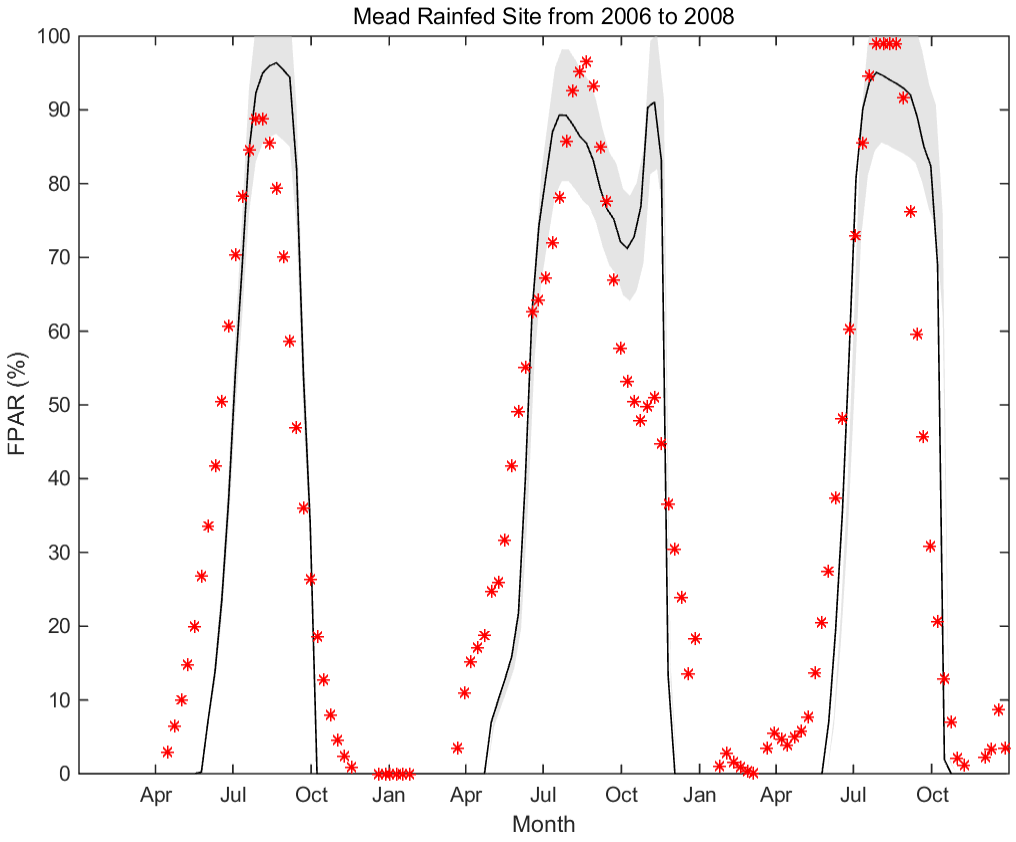
Mead Rainfed Site from 2006 to 2008
FPAR (%)
Month
0
10
20
30
40
50
60
70
80
90
100
Apr
Jul
Oct
Jan
Apr
Jul
Oct
Jan
Apr
Jul
Oct

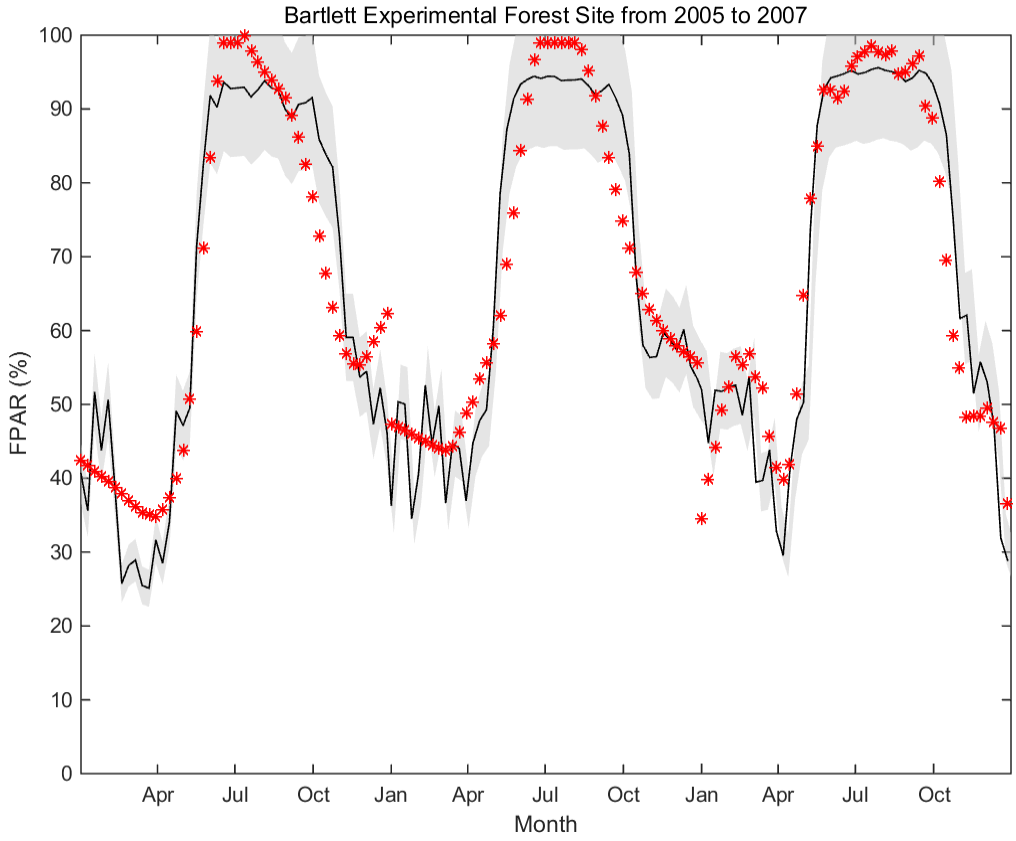
Bartlett Experimental Forest Site from 2005 to 2007
FPAR (%)
Month
0
10
20
30
40
50
60
70
80
90
100
Apr
Jul
Oct
Jan
Apr
Jul
Oct
Jan
Apr
Jul
Oct

Fig. 4-6 The time series of in-situ FAPAR measurements and integrated FAPAR at four AmeriFlux sites. The shaded area is the 10% accuracy requirement.

4.3.3. Regional scale fusion

The estimation of the FAPAR in multiple-resolution remotely sensed scenes, and the subsequent integration at the regional scale using the MRT method is presented in this subsection. Two study regions covering the four AmeriFlux sites were selected and their geographic locations are shown in Fig. 4-7 (a). The specific MODIS tiles and the MISR and Landsat orbits covering the two study regions are listed in Table 4-4. The temporal resolutions of the MISR, MODIS, and Landsat TM/ETM+ reflectance or FAPAR products are 2–9 days, 8 days, and 16 days, respectively. The MISR, MODIS, and Landsat scenes around the four AmeriFlux sites in the vegetation growing season were carefully selected in Cases 1 and 2 so that they had the closest imaging dates in all the three cases. The image qualities in Cases 1 and 2 were strictly controlled so that the scenes had little or no cloud contamination. Case 3 is a control experiment without quality control of the scene to determine the performance of the MRT on cloud contaminated scenes with gaps in the data. The imaging dates of the products differed within 4 days in Cases 1 and 2, and within 15 days in Case 3. The vegetation is assumed to have remained relatively stable within this short period and therefore, the integration of FAPAR from these different sensors is reliable.

The Landsat reflectance data were atmospherically corrected using the Landsat ecosystem disturbance adaptive processing system (LEDAPS) preprocessing code. Missing scan lines in the ETM+ image were filled with the values of the nearest

pixels. The 30 m spatial resolution Landsat TM and two ETM+ surface reflectance scenes are illustrated in Fig. 4-7 (b–d), respectively. The MSIR data were resampled into a spatial resolution of 960 m, and the MODIS 500 m and 250 m data were resampled into 480 m and 240 m, respectively, to construct a multi-scale tree-structured model. In this case, a 1 ×1 MISR pixel corresponds to 2 ×2 MODIS 480 m pixels, 4 ×4 MODIS 240 m pixels, and 32 ×32 TM/ETM+ 30 m pixels.

Table 4-4 The spatial coverage and imaging date information of the MODIS, the MISR and the Landsat data used in the three cases.

Case	MODIS tile	MISR orbit	Landsat orbit	MODIS date	MISR date	Landsat date
Case 1	H10V04	P27B58	P28R31	Aug 5–12, 2006	Aug 4, 2006	Aug 3, 2006
Case 2	H12V04	P12B55	P12R29	Aug 5–12, 2005	Aug 8, 2005	Aug 8, 2005
Case 3	H12V04	P11B55	P12R29	Sep 6–13, 2006	Sep 21, 2006	Sep 12, 2006

Case 1 covers three sites: Mead Irrigated, Mead Irrigated Rotation, and Mead Rainfed. Cases 2 and 3 cover Bartlett site. The “H” and “V” of MODIS tile means horizontal and vertical, respectively. The “P” and “B” of MISR orbit means path and block, respectively. The “P” and “R” of Landsat orbit means path and row, respectively.

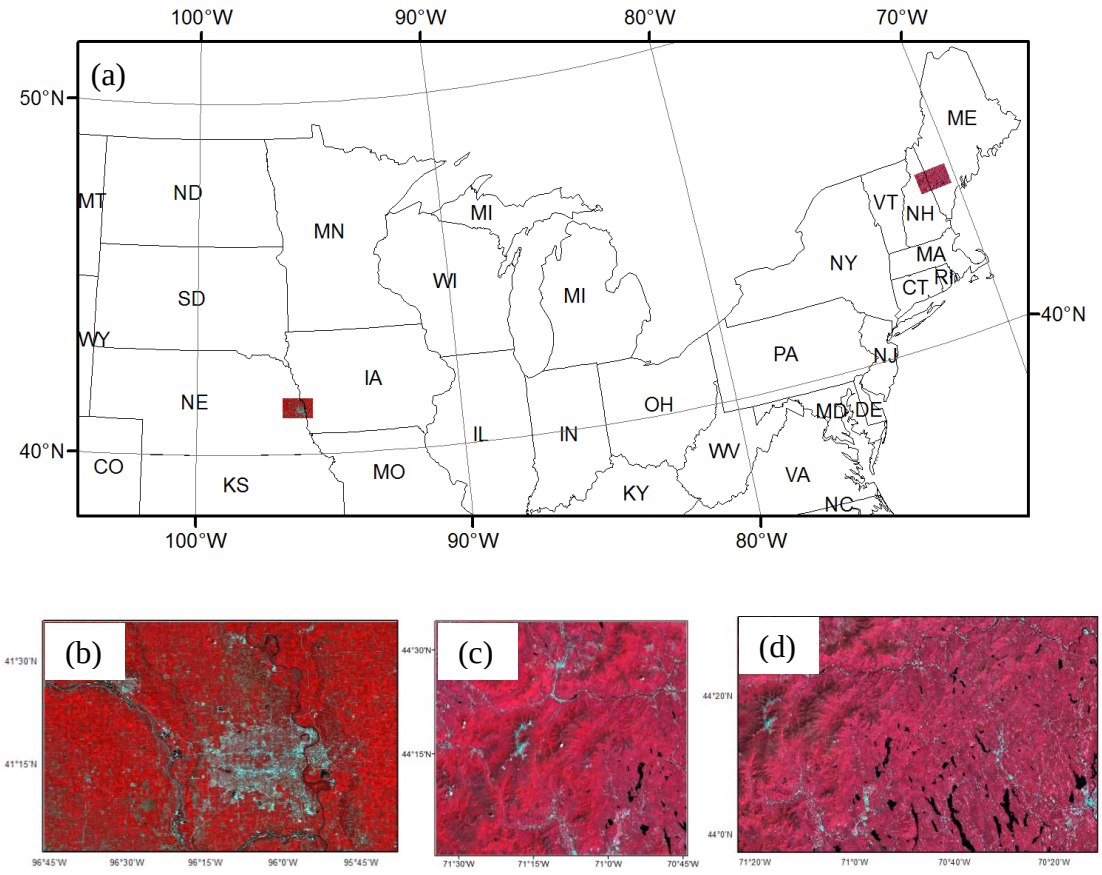

Fig. 4-7 (a) Geographic locations of the two study regions in Cases 1, 2 and 3. The study region of Case 1 is the lower left red rectangle, and the study region of Cases 2 and 3 are the upper right red rectangle. (b) The Landsat TM surface reflectance scene in Case 1 in NIR-Red-Green false color composition, which covers three sites: Mead Irrigated, Mead Irrigated Rotation, and Mead Rainfed. (c, d) The Landsat ETM+ surface reflectance scenes in Cases 2 and 3 in NIR-Red-Green false color composition, both of which cover the Bartlett site.

The MODIS FAPAR product uses the MCD12 land cover product to distinguish among 13 land covers globally. The National Land Cover Database 2006 (NLCD 2006) uses a 16-class land cover classification scheme for Landsat images. A land cover classification scheme combining these two classifications was used considering

the existing land covers in the two study regions. The MISR, MODIS, and Landsat images were classified into evergreen forest, deciduous forest, urban, grass, crops, barren soil, and water body. The classified images and surface reflectance images were combined to estimate vegetation FAPAR values using the model in Tao et al. (In review). Distributions of the FAPAR estimates in the MISR, MODIS, TM, and ETM+ images for the three cases are shown Fig. 4-8 (a–d), Fig. 4-11 (a–d) and Fig. 4-14 (a–d), respectively. The FAPAR estimates are consistent across different scales. They have similar distribution patterns across scales, with the highest values observed in evergreen forests, higher values in deciduous forests, and smaller values in crops, and close-to-zero values in rivers and central urban areas. Some gaps exist in the MISR scene in Case 3 caused by the missing values in the surface reflectance data. This is because that the MISR surface reflectance products have strict data control, including radiance angle-to-angle smoothness and image angle-to-angle correlation tests, so that there could be large gaps in the MISR level 2 surface reflectance product (Hu et al., 2007).

The MRT method was implemented to integrate the FAPAR data across different scales. Overlapping trees were utilized so that the resulting images were smooth, mitigating the blocky effect. The integration results are shown in Fig. 4-8 (e–h), Fig. 4-11 (e–h), and Fig. 4-14 (e–h) for Cases 1, 2, and 3, respectively. The MRT method filled the gaps in the original FAPAR estimates in the MISR data in Case 3. Therefore, image quality was greatly improved in terms of spatial continuity in this case. The FAPAR distribution became more homogeneous and continuous after data fusion in all the three cases, which is desirable in terms of continuity among multiple-scale data.

Some pixels with low values of FAPAR depicted as blue exist along the boundary between the vegetation and non-vegetation regions in the map after applying MRT. They were caused by the sparse vegetation observed near the river or urban area at higher resolution. The actual values of these blue pixels are very small (less than 0.1). Difference maps between other scales and the finest Landsat scale are shown in Fig. 4-9, Fig. 4-12, and Fig. 4-15 for the three cases, and they clearly demonstrate that differences became much smaller after applying the MRT method across scales.

The frequency histograms for all pixels in the maps across different scales are shown in Fig. 4-10 (a, b) and Fig. 4-13 (a, b) for Cases 1 and 2, respectively. The statistics of the FAPAR values agreed better with each other across scales after fusion. More vegetation pixels were detected in coarse resolution images after fusion due to the integration of the high-resolution Landsat data into the coarse-resolution images. The improvements were even greater when there were gaps in the original FAPAR estimates, as demonstrated in the frequency histograms in Fig. 4-16 (a, b) for Case 3. The regional mean of the MISR FAPAR estimates was significantly lower than the regional mean of the other products before fusion, but agreed well with the other products after fusion.

The frequency histograms of the difference maps between other scales and the finest Landsat scale are shown in Fig. 4-10 (c, d), Fig. 4-13 (c, d), and Fig. 4-16 (c, d) for the three cases, which verify that the differences among scales became, generally, sufficiently small (< 0.05) in both regions. Therefore, the FAPAR distributions at coarse-resolutions (960 m, 480 m, and 240 m) were closer to the distribution at the finest resolutions after data fusion. Because more details are available in higher-

resolution images, the results at the finer-scale were considered to be close to the truth. Therefore, FAPAR distributions at coarse-scales were improved after data fusion in terms of image quality and accuracy.

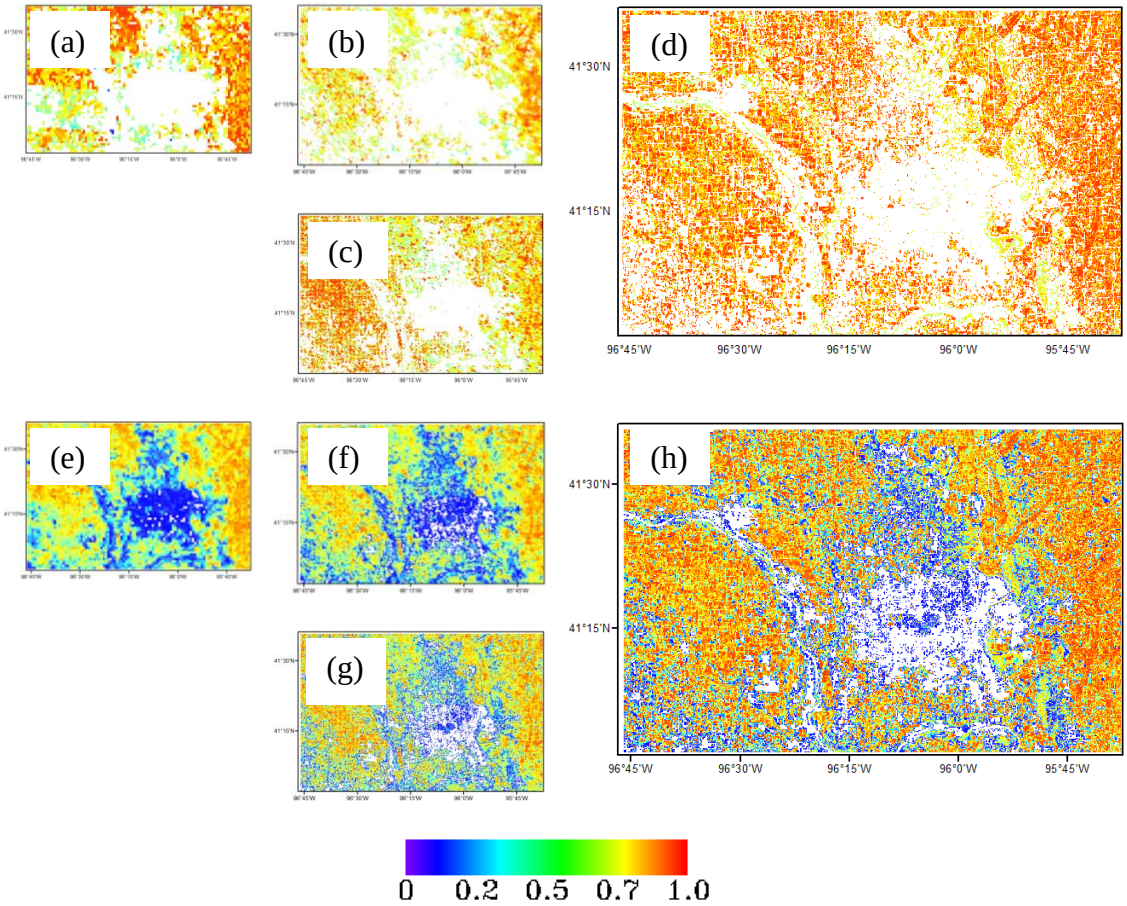

Fig. 4-8 FAPAR distributions before and after fusion in MISR, MODIS, and TM scenes in Case 1. (a-d) show MISR, MODIS 480 m, MODIS 240 m, and TM FAPAR estimates before fusion, and (e-h) show the FAPAR distributions after fusion. The white colors are non-vegetation or sparse vegetation with FAPAR values smaller than 0.01.

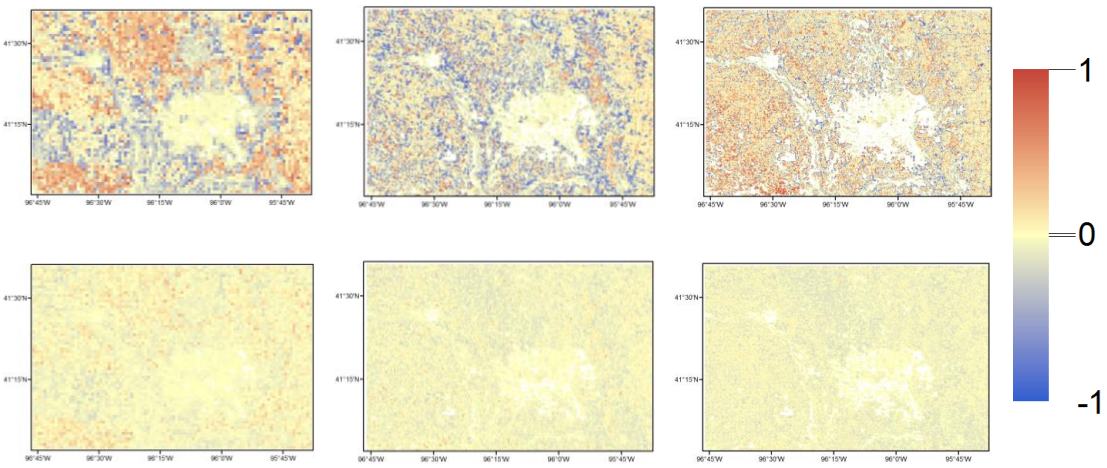

Fig. 4-9 Top panels show the differences between other scales FAPAR and TM FAPAR before fusion: MISR, MODIS 480 m, and MODIS 240 m from left to right. Bottom panels show the differences after fusion: MISR, MODIS 480 m, and MODIS 240 m from left to right.

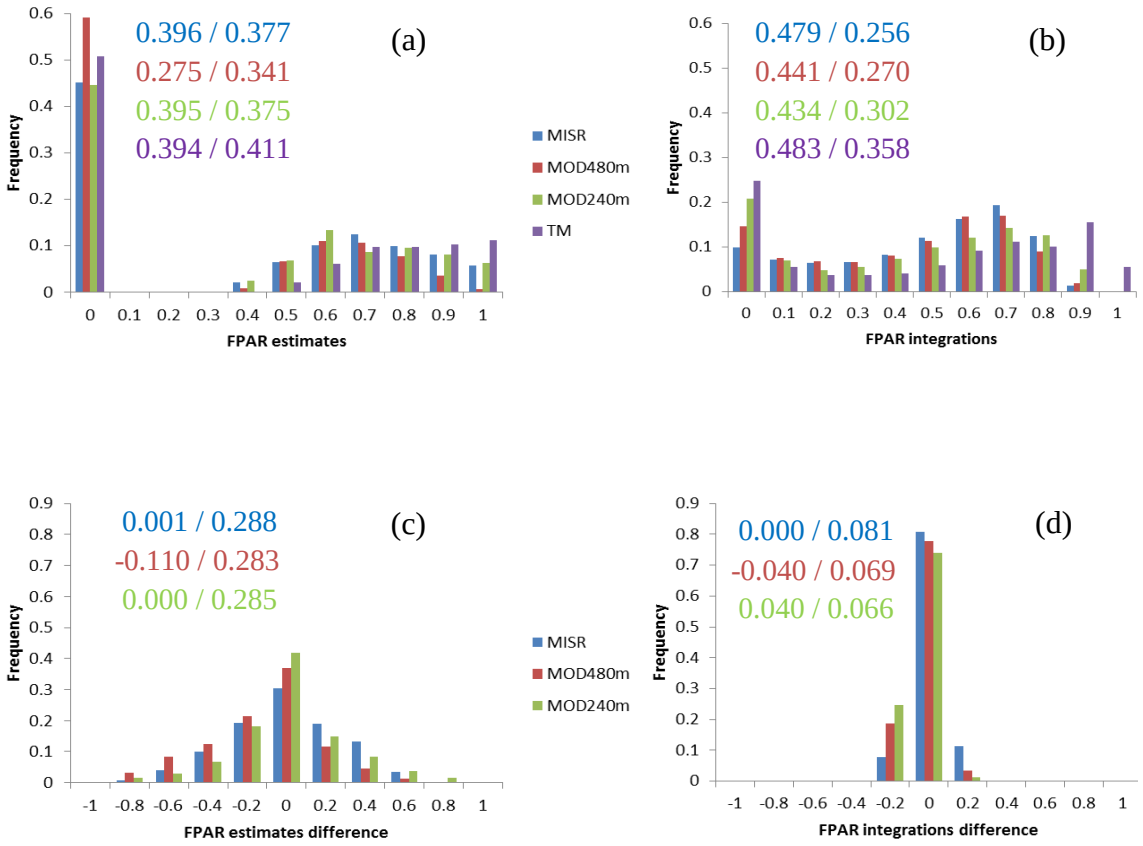

Fig. 4-10 The FAPAR frequency histograms in the MISR, MODIS, and TM scenes before (a) and after (b) data fusion in Case 1. Frequency histograms of the FAPAR differences between other scales FAPAR and TM FAPAR before (c) and after (d) fusion. The numbers are the regional mean and standard deviations.

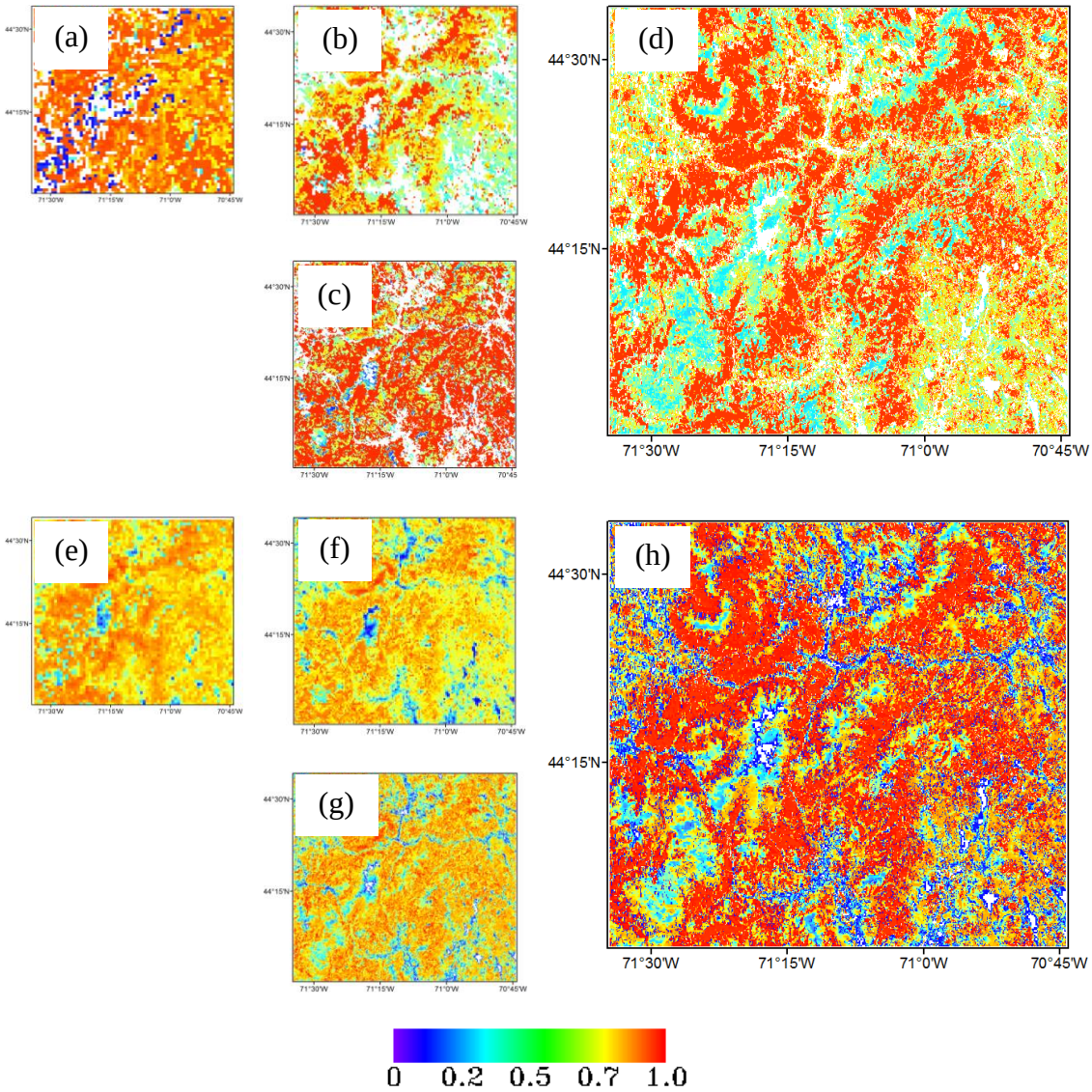

Fig. 4-11 FAPAR distributions before and after fusion in MISR, MODIS, and ETM+ scenes in Case 2. (a-d) show MISR, MODIS 480 m, MODIS 240 m, and ETM+ FAPAR estimates before fusion, and (e-h) show the FAPAR distributions after fusion.

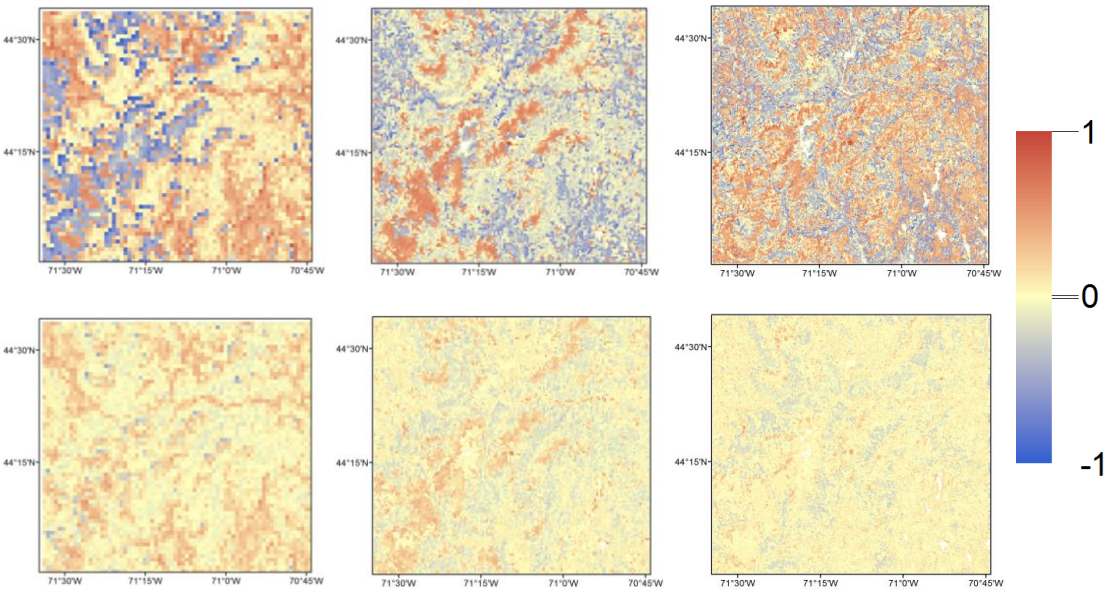

Fig. 4-12 Top panels show the differences between other scales FAPAR and ETM+ FAPAR before fusion: MISR, MODIS 480 m, and MODIS 240 m from left to right. Bottom panels show the differences after fusion: MISR, MODIS 480 m, and MODIS 240 m from left to right.

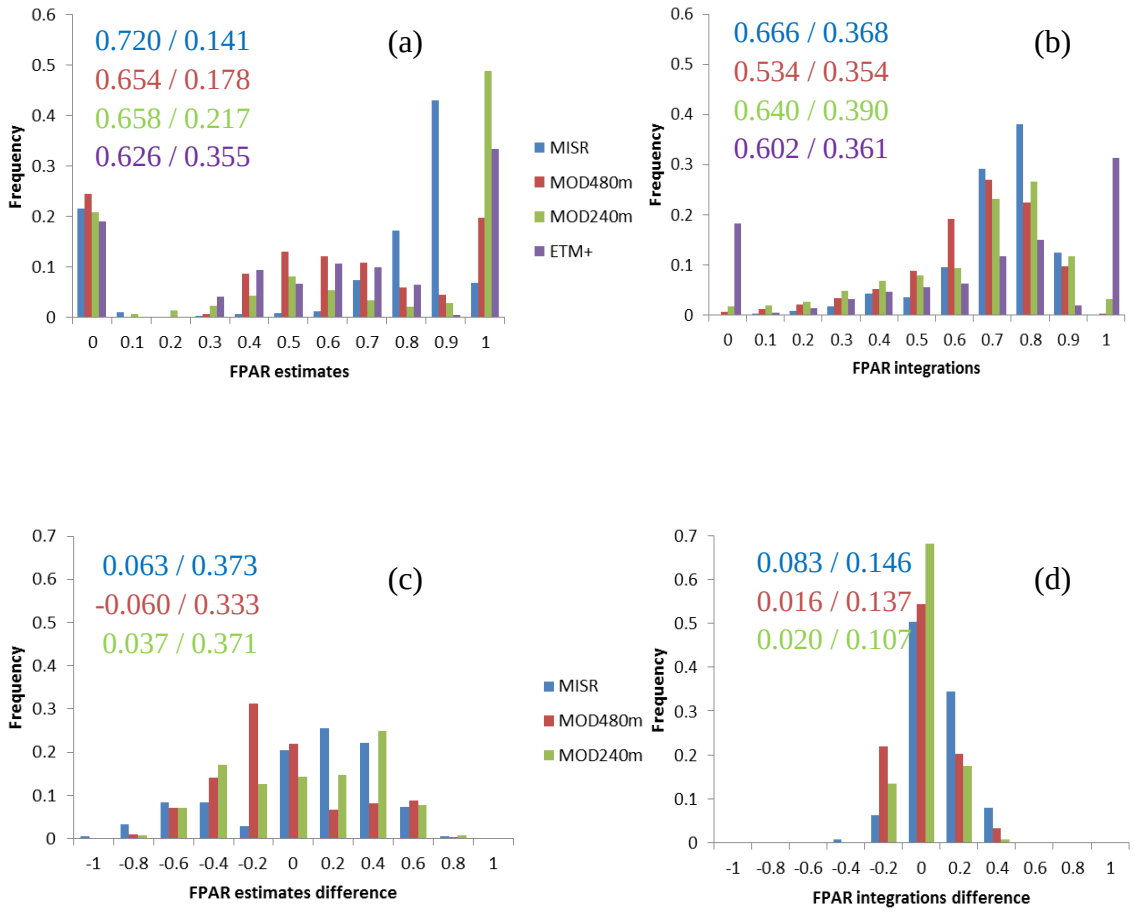

Fig. 4-13 The FAPAR frequency histograms in the MISR, MODIS, and ETM+ scenes before (a) and after (b) data fusion in Case 2. Frequency histograms of the FAPAR differences between other scales FAPAR and ETM+ FAPAR before (c) and after (d) fusion. The numbers are the regional mean and standard deviation.

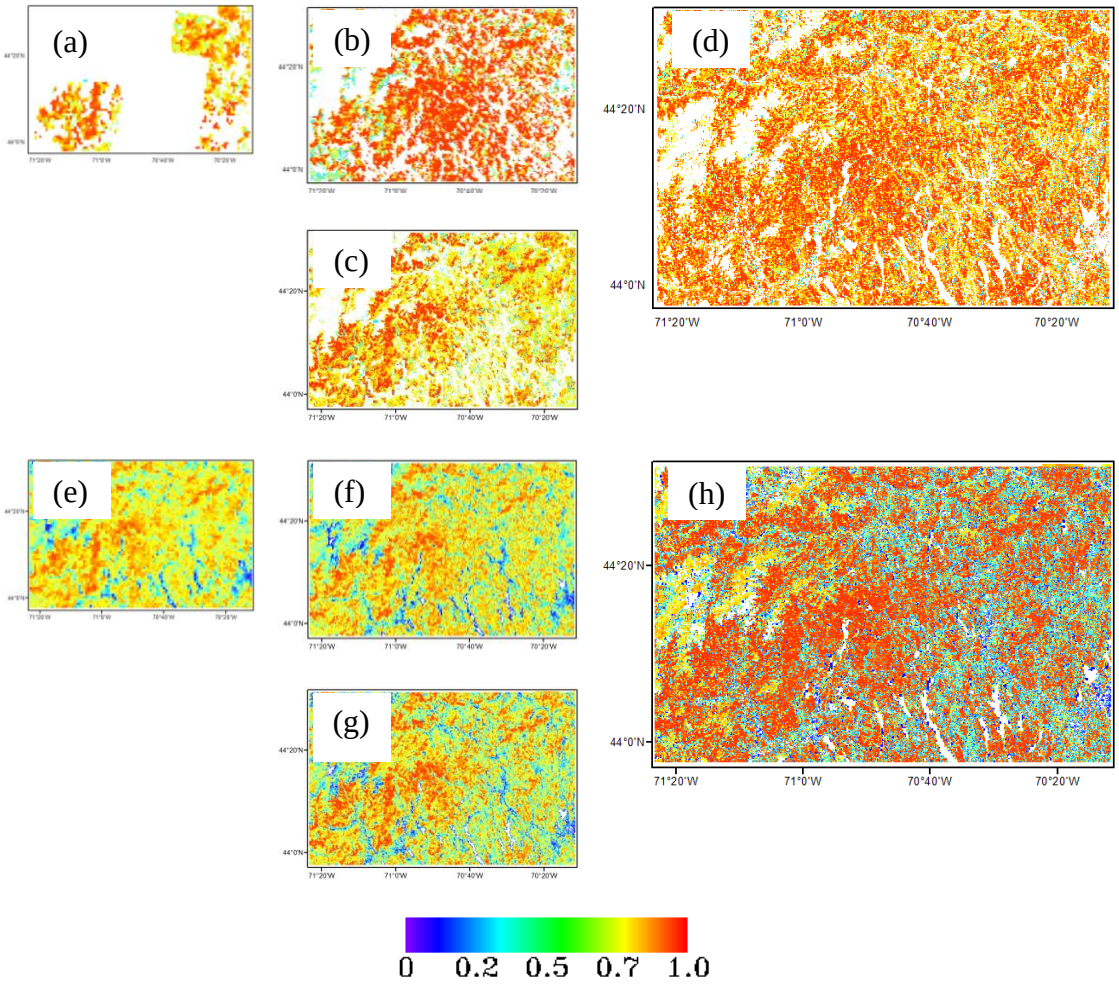

Fig. 4-14 FAPAR distributions before and after fusion in MISR, MODIS, and ETM+ scenes in Case 3. (a-d) show MISR, MODIS 480 m, MODIS 240 m, and ETM+ FAPAR estimates before fusion, and (e-h) show the FAPAR distributions after fusion.

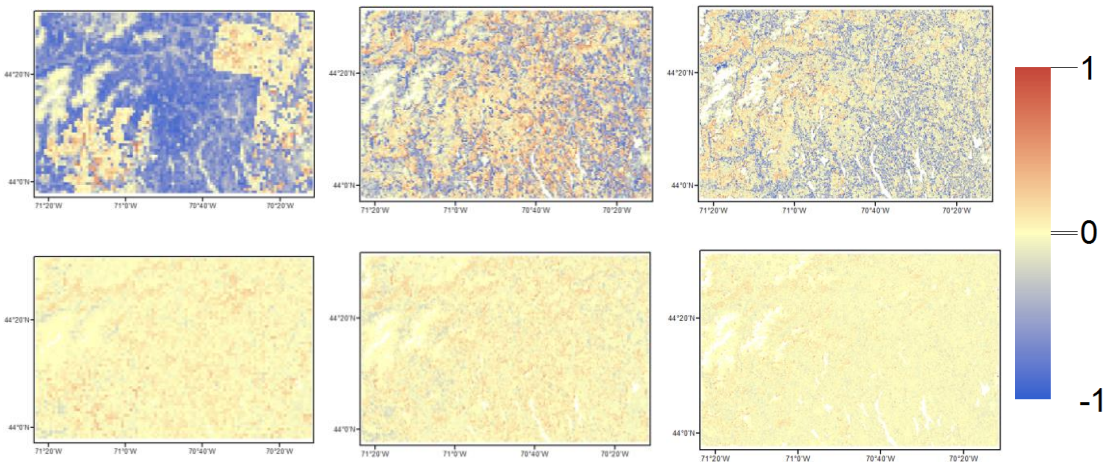

Fig. 4-15 Top panels show the differences between other scales FAPAR and TM FAPAR before fusion: MISR, MODIS 480 m, and MODIS 240 m from left to right. Bottom panels show the differences after fusion: MISR, MODIS 480 m, and MODIS 240 m from left to right.

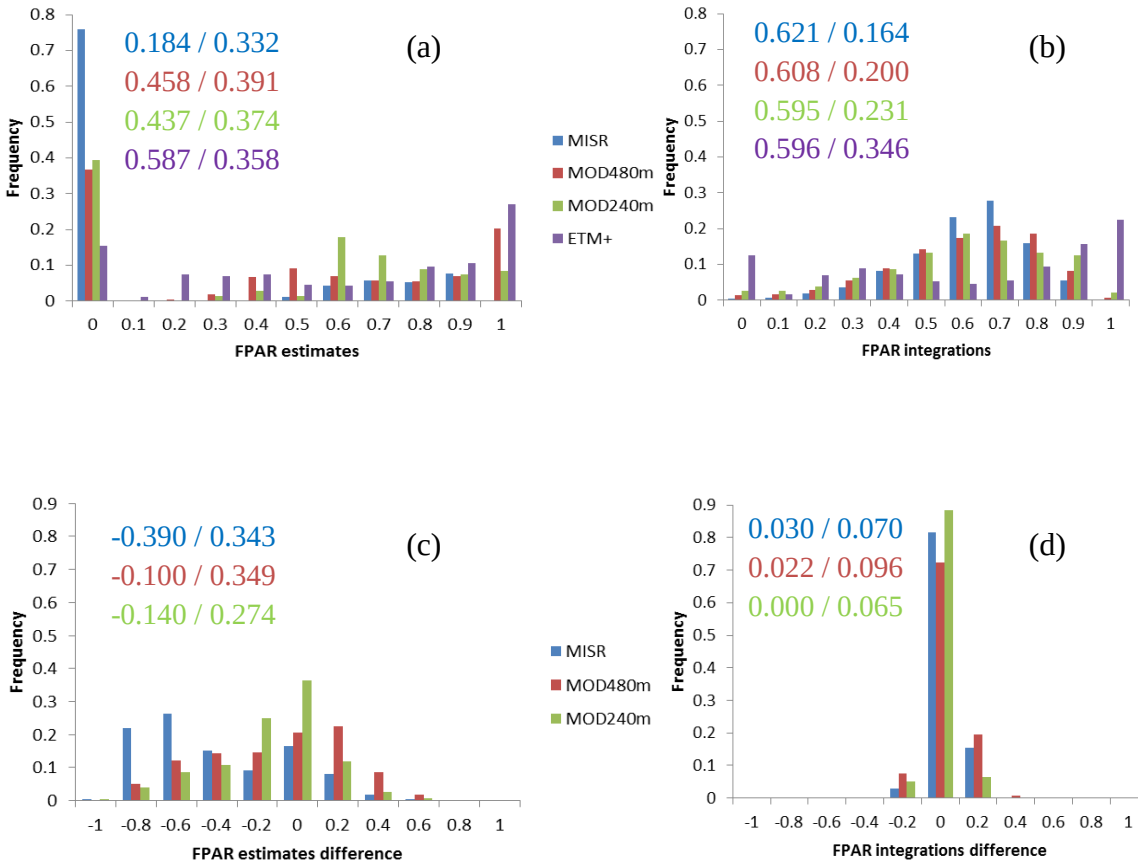

Fig. 4-16 The FAPAR frequency histograms in the MISR, MODIS, and ETM+ scenes before (a) and after (b) data fusion in Case 3. Frequency histograms of the FAPAR differences between other scales FAPAR and ETM+ FAPAR before (c) and after (d) fusion. The numbers are the regional mean and standard deviations.

4.4. Discussion

Satellite FAPAR products perform differently across different land covers. It is difficult to obtain a universal integration coefficient applicable to all land cover types due to their varied accuracy over different land cover types. The seasonal curves of individual FAPAR products are similar annually over one specific land cover type,

which makes feasible the integration over longer than one year time period once the integration coefficients are determined annually for the specific land cover. The prerequisite of a reliable integration is one year of in situ FAPAR measurements to determine the coefficients of individual FAPAR products. The validation of the integration results at the AmeriFlux sites showed that the coefficients were relatively reliable during years, with satisfactory integration results.

Individual FAPAR products and the integrated FAPAR perform better during the middle of the growing season than the beginning and end of the growing season. There exist some underestimations in the latter half of the year, and specifically at the end of the growing season. The discrepancy between FAPAR products and in situ measurements at the beginning and end of the growing season can be attributed to two reasons. One reason could be the time difference between the MODIS and MERIS FAPAR data imaging and the in situ measurements. The temporal resolution of MODIS and MERIS FAPAR products are 8 days or monthly without actual date-of acquisition information, and thus the imaging time may not overlap perfectly with that of in situ measurements. Therefore, the resultant FAPAR difference between satellite products and in situ measurements is large at the beginning and end of the vegetation growing season when the vegetation changes quickly. However, the time shift issue is not a serious issue during the middle of the vegetation growing season when the vegetation remains relatively stable. Another reason for the discrepancy is the senescence and leaves turning yellow at the end of growing season. This results in the difference between green FAPAR and the ground-based total FAPAR measurements which includes the absorptions of both green and yellow leaves during

this period. The MERIS FAPAR product corresponds to green FAPAR among the three satellite FAPAR products. This study removes the bias between green FAPAR and total FAPAR for the MERIS FAPAR product during the whole growing season. Further improvements may need to divide the growing season into two parts and remove the biases separately.

In the regional scale fusion experiments, the FAPAR distributions before the fusion vary significantly across scales. This could be a result of the differences between the surface reflectance data arising from the differences in the calibration and atmospheric correction processes. Needless to say, the differences in the FAPAR distributions are larger when there are missing values in the images at some scales. The differences become even greater when the MISR and MODIS FAPAR products are used, which is one of the reasons they were not directly used in the regional study. Another reason of not using the MISR and MODIS FAPAR products directly was that the spatial resolutions of the MISR and MODIS FAPAR products are 1.1 km and 1 km, respectively, which renders the generation of multiscale images difficult or the corresponding statistical analysis much more complex (Huang et al., 2002; Zhu et al., 2004). However, the differences of the FAPAR values for vegetation pixels across scales are smaller than as demonstrated in the frequency histograms of Fig. 4-10, Fig. 4-13, and Fig. 4-16, which show the FAPAR distributions in the whole image, regardless of whether the pixel is classified as vegetation or not. The histograms agree better across scales if the distributions of FAPAR for only vegetation pixels are displayed (histograms shown in Tao et al. (In review)).

Chapter 5 Conclusions

This study focuses on improving the estimation of FAPAR from multiple satellite data products. The accuracy of the existing FAPAR products was evaluated by intercomparison with each other at the global scale and validation with ground measurements. A new FAPAR model was developed and its parameterizations were designed to achieve an improved accuracy toward the requirement of 0.05. Multiple FAPAR data integration was implemented considering their characteristics and accuracy as an alternative to developing new models to improve the accuracy of FAPAR estimations. The major findings, major contributions, and future study are concluded in the following individual sections.

5.1. Major Findings

Five existing global FAPAR products, namely, MODIS, MERIS, MISR, SeaWiFS, and GEOV1 are intercompared and directly validated over different land cover types at the global, hemispheric and local scales. Absolute FAPAR values are on average in decreasing order of MISR, MODIS, GEOV1, SeaWiFS, and MERIS. The MISR and MODIS FAPAR products tend to agree well with each other and so do the MERIS and SeaWiFS FAPAR products, but the difference between the two groups could be as large as 0.1. The seasonality of the products agrees better with each other in the Northern Hemisphere and globally than in the Southern Hemisphere. The seasonality of northern hemispheric FAPAR is close to those of global FAPAR over most of the land cover types, including grass, crop, shrubland, and broadleaf deciduous,

needleleaf evergreen, and needleleaf deciduous forests. However, the conclusions from the northern hemispheric scale cannot be extended to the global scale for land covers such as savannahs and broadleaf evergreen forests, where seasonal patterns are obvious in the Northern Hemisphere but unnoticeable globally, because of the large contribution from the Southern Hemisphere over these two land covers. The differences between the products are consistent throughout the year over most of the land cover types, except over the forests. The possible reason could be traced to the different assumptions in the retrieval algorithms over forests and the differences between green and total FAPAR products due to tree trunk and branch absorption.

The MERIS, MODIS, MISR, and GEOV1 FAPAR products have an uncertainty of 0.14 validating with total FAPAR measurements, and 0.09 validating with green FAPAR measurements. The uncertainties of current satellite FAPAR products (within ±0.1) are still unable to meet the threshold accuracy requirements stipulated by GCOS (±0.05).

The FAPAR estimates by the new model were intercompared with reference satellite FAPAR products and validated with field measurements at the VAlidation of Land European Remote sensing Instruments (VALERI) and AmeriFlux experimental sites. The validation results showed that the FAPAR estimates by our method had slightly better performance than the MODIS and the MISR FAPAR products when using corresponding satellite LAI product values as input. The FAPAR estimates can be further improved with the improved LAI estimates from the presented model as input. The improvements are apparent at grasslands and forests with an 8% reduction of uncertainty. The new model can successfully identify the growing seasons and

produce smooth time series curves of estimated FAPAR over years. The root mean square error (RMSE) was reduced from 0.16 to 0.11 for MODIS and from 0.18 to 0.1 for MISR overall. Application of the presented model at a regional scale generated consistent FAPAR maps at 30 m, 500 m, and 1100 m spatial resolutions from the Landsat, MODIS, and MISR data.

As an alternative method to improving FAPAR accuracy in addition to developing new models, satellite FAPAR values were integrated using two data fusion schemes. The OI scheme was applied at the site scale to integrate the MODIS, MERIS and MISR FAPAR products. The MRT scheme was applied at the regional scale to integrate the MISR, MODIS, and TM/ETM+ FAPAR values at multiple resolutions. The integrated FAPAR using OI reduced the biases from the MISR (0.032), MODIS (0.015), and MERIS (-0.130) to -0.013. The R^2 improved close to 0.85, a 20% increase over the average R^2 of the individual products. The integrated FAPAR had an average accuracy of 0.09, which is on the path to the accuracy requirement of 0.05. The MRT algorithm filled the cloud contaminated regions and other gaps and therefore improved the image quality. Moreover, the FAPAR values became more consistent at multiple resolutions.

5.2. Major Contributions

This study assessed the FAPAR products in Chapter 2, improved FAPAR accuracy through a new model in Chapter 3 and applied the FAPAR fusion methods in Chapter 4. The major contributions are:

- No global inter-comparisons between MODIS, MISR, MERIS, GEOV1, and SeaWiFS FAPAR products have been made previously.
- Multiple FAPAR products have been assessed together with a comprehensive set of measurements from at least two field experiments, so that the validation efforts fulfilled the requirement of stage 2 of the validation: Product accuracy has been assessed over a widely distributed set of locations and time periods.
- A new FAPAR estimation algorithm has been developed with local pixel based soil background and leaf canopy albedos.
- The new algorithm uses just satellite data as input, and not being bound by a specific sensor.
- It is the first study on integrating FAPAR products at both the temporal and spatial domains for continuity and high accuracy.
- The reduced uncertainty in FAPAR values from this study by 5% would help to decrease an equal amount of uncertainty in the estimation of gross and net primary production and carbon fluxes.

5.3. Future Study

This study has some limitations, and corresponding future work could investigate the following:

- Significant efforts have to be accomplished to reach stage 3 of the validation: Product accuracy has been assessed, and the uncertainties in the product well-established via independent measurements made in a systematic and statistically robust way that represents global conditions.

- The presented FAPAR model is suitable for homogeneous landscape and has better performance over homogeneous land cover. Future study could develop an advanced FAPAR model suitable for heterogeneous landscape.
- Time shifts among FAPAR products may induce some error in the integration results. Further improvements could be increased temporal resolutions of individual FAPAR products to enhance time match.
- Further improvements of FAPAR accuracy include combining multiple observations with reduced uncertainty and addressing the scale difference between in situ measurements and moderate resolution pixels.

Appendix: The parameters for FAPAR estimation

The calculation of FAPAR requires the knowledge of LAI and ϕ, which can be solved using the following equations:

$$\rho = \rho^1 + \rho^{\mathrm{m}} \tag{A1}$$

where ρ^1 means the contribution of single scattering, and ρ^{m} represents the contribution of multiple scattering.

$$\begin{aligned}\rho^1 = \rho_{\mathrm{g}} &\left\{ e^{-\lambda_0\left[\frac{G_{\mathrm{s}}}{\mu_{\mathrm{s}}}+\frac{G_{\mathrm{v}}}{\mu_{\mathrm{v}}}-\frac{G_{\mathrm{v}}}{\mu_{\mathrm{v}}}\cdot\Gamma(\phi)\right]LAI} + \left[e^{-\lambda_0\frac{G_{\mathrm{v}}}{\mu_{\mathrm{v}}}\cdot LAI} - e^{-\lambda_0\left[\frac{G_{\mathrm{s}}}{\mu_{\mathrm{s}}}+\frac{G_{\mathrm{v}}}{\mu_{\mathrm{v}}}-\frac{G_{\mathrm{v}}}{\mu_{\mathrm{v}}}\cdot\Gamma(\phi)\right]LAI} \right] \frac{E_{\mathrm{d}}}{\mu_0 F_0 + E_{\mathrm{d}}} \right\} + \\ \rho_{\mathrm{c}} &\left\{ \left(1 - e^{-\lambda_0\frac{G_{\mathrm{v}}}{\mu_{\mathrm{v}}}\cdot LAI\cdot\Gamma(\phi)} \right) + \left[e^{-\lambda_0\frac{G_{\mathrm{v}}}{\mu_{\mathrm{v}}}\cdot LAI\cdot\Gamma(\phi)} - e^{-\lambda_0\frac{G_{\mathrm{v}}}{\mu_{\mathrm{v}}}\cdot LAI} \right] \frac{E_{\mathrm{d}}}{\mu_0 F_0 + E_{\mathrm{d}}} \right\}\end{aligned} \tag{A2}$$

where E_{d} is the diffuse irradiance from sky scattering; and $\mu_0 F_0$ is the direct irradiance from solar illumination. The meanings of other symbols are described in Section 3.2. The contribution of multi-scattering can be expressed by the Hapke model:

$$\rho^{\mathrm{m}} = \frac{\omega}{4}\cdot\frac{1}{\mu_{\mathrm{v}}\mu_0}\left[H\left(\mu_{\mathrm{v}}\right)H\left(\mu_{\mathrm{s}}\right)-1\right]I_{\mathrm{ms}} \tag{A3}$$

where ω is single scattering albedo of single leaf, $\omega \cong 2\rho_{\mathrm{v}}$

$$H\left(\mu_{\mathrm{s,v}}\right) = \frac{1+2\mu_{\mathrm{s,v}}}{1+2\mu_{\mathrm{s,v}}\sqrt{1-\omega}} \tag{A4}$$

$$I_{\mathrm{ms}} = \frac{1}{\Delta'}\left(1-e^{-\Delta'\cdot\lambda_0\cdot LAI}\right),\ \Delta' = \frac{G_{\mathrm{s}}}{\mu_{\mathrm{s}}}+\frac{G_{\mathrm{v}}}{\mu_{\mathrm{v}}} \tag{A5}$$

When solar and viewing directions overlap each other,

$$\rho^{\mathrm{m}} = \rho_{\mathrm{v}} \cdot \frac{\left[H^2\left(\mu_{\mathrm{v}}\right)-1\right]}{4\mu_{\mathrm{v}}G_{\mathrm{v}}}\left(1-e^{-2\lambda_0\frac{G_{\mathrm{v}}}{\mu_{\mathrm{v}}}LAI}\right) \tag{A6}$$

Therefore, Eqs. (A1), (A2), and (A3) express observed reflectance as a function of LAI and ϕ, which can be solved with observations at two or more wavelengths. The equation group is nonlinear and has to be solved with an iterative method, an optimization algorithm, or a LUT, the last of which is adopted here, considering its robustness.

Glossary

ETM+	Landsat Enhanced Thematic Mapper Plus
FAPAR	Fraction of absorbed PAR
GCOS	Global Climate Observing System
GPP	gross primary production
LAI	leaf area index
MGVI	MERIS Global Vegetation Index
MISR	Multi-angle Imaging SpectroRadiometer
MODIS	Moderate Resolution Imaging Spectroradiometer
MRT	Multiple resolution tree
NDVI	normalized difference vegetation index
NIR	near infrared
NPP	net primary production
OI	optimal interpolation
PAR	photosynthetically active radiation
RMSE	root mean square error
RT	radiative transfer
TM	Landsat Thematic Mapper
VALERI	VAlidation of Land European Remote sensing Instruments
4S	four stream
T_0	canopy transmittance along direct light penetrating path

T_f	canopy transmittance along diffuse light penetrating path
T_v	canopy transmittance along viewing direction
$\mathbf{A}_u$	state conversion matrix that estimates the variable at node *u* from its parent layer
$\mathbf{C}_u$	observation matrix that coverts the variable of interest to the satellite data
β	ratio of scattering light
λ_0	Nilson parameter
$\rho_{g,\lambda}$	ground reflectance at wavelength λ
$\rho_{v,\lambda}$	vegetation reflectance at wavelength λ
σ^2	variance of the error

References

Asner, G.P., Wessman, C.A., & Archer, S. (1998). Scale dependence of absorption of photosynthetically active radiation in terrestrial ecosystems. *Ecological Applications, 8*, 1003-1021

Asrar, G., Myneni, B.J., & Choudhury, B.J. (1992). Spatial heterogeneity in vegetation canopies and remote sensing of absorbed photosyntheticaly active radiation: A modeling study. *Remote Sensing of Environment, 41*, 85-103

Baret, F., Hagolle, O., Geiger, B., Bicheron, P., Miras, B., Huc, M., Berthelot, B., Nino, F., Weiss, M., Samain, O., Roujean, J.L., & Leroy, M. (2007). LAI, fAPAR and fCover CYCLOPES global products derived from VEGETATION - Part 1: Principles of the algorithm. *Remote Sensing of Environment, 110*, 275-286

Baret, F., Weiss, M., Lacaze, R., Camacho, F., Makhmara, H., Pacholcyzk, P., & Smets, B. (2013). GEOV1: LAI and FAPAR essential climate variables and FCOVER global time series capitalizing over existing products. Part1: Principles of development and production. *Remote Sensing of Environment, 137*, 299-309

Bonan, G.B., Oleson, K.W., Vertenstein, M., Levis, S., Zeng, X., Dai, Y., Dickinson, R.E., & Yang, Z.L. (2002). The land surface climatology of the community land model coupled to the NCAR community climate model. *Journal of Climate, 15*, 3123-3149

Camacho, F., Cemicharo, J., Lacaze, R., Baret, F., & Weiss, M. (2013). GEOV1: LAI, FAPAR essential climate variables and FCOVER global time series capitalizing over existing products. Part 2: Validation and intercomparison with reference products. *Remote Sensing of Environment, 137*, 310-329

Carrer, D., Roujean, J.L., Lafont, S., Calvet, J.C., Boone, A., Decharme, B., Delire, C., & Gastellu-Etchegorry, J.P. (2013). A canopy radiative transfer scheme with explicit FAPAR for the interactive vegetation model ISBA-A-gs: Impact on carbon fluxes. *Journal of Geophysical Research-Biogeosciences, 118*, 888-903

Chou, K.C. (1991). A stochastic modeling approach to multiscale signal processing. In, *Dept. EECS*: MIT

Chou, K.C., Willsky, A.S., & Nikoukhah, R. (1994). Multiscale systems, Kalman filters, and Riccati-equations. *Ieee Transactions on Automatic Control, 39*, 479-492

D'Odorico, P., Gonsamo, A., Pinty, B., Gobron, N., Coops, N., Mendez, E., & Schaepman, M.E. (2014). Intercomparison of fraction of absorbed photosynthetically active radiation products derived from satellite data over Europe. *Remote Sensing of Environment, 142*, 141-154

Fang, H., Liang, S., Townshend, J., & Dickinson, R. (2008). Spatially and temporally continuous LAI data sets based on an new filtering method: Examples from North America. *Remote Sensing of Environment, 112*, 75–93

Fang, H., Wei, S., & Liang, S. (2012). Validation of MODIS and CYCLOPES LAI products using global field measurement data. *Remote Sensing of Environment, 119*, 43-54

Fang, H.L., Liang, S.L., McClaran, M.P., van Leeuwen, W.J.D., Drake, S., Marsh, S.E., Thomson, A.M., Izaurralde, R.C., & Rosenberg, N.J. (2005). Biophysical characterization and management effects on semiarid rangeland observed from

Landsat ETM+ data. *Ieee Transactions on Geoscience and Remote Sensing*, *43*, 125-134

Fensholt, R., Sandholt, I., & Rasmussen, M.S. (2004). Evaluation of MODIS LAI, fAPAR and the relation between fAPAR and NDVI in a semi-arid environment using in situ measurements. *Remote Sensing of Environment, 91*, 490-507

Fieguth, P.W., Karl, W.C., Willsky, A.S., & Wunsch, C. (1995). Multiresolution optimal interpolation and statistical-analysis of TOPEX/POSEIDON satellite altimetry. *Ieee Transactions on Geoscience and Remote Sensing*, *33*, 280-292

Friedl, M.A. (1997). Examining the effects of sensor resolution and sub-pixel heterogeneity on vegetation spectral indices: implications for biophysical modeling. In D.A. Quattrochi, & M.F. Goodchild (Eds.), *Scale in remote sensing and GIS* (pp. 113-139). Boca Raton, Fla: Lewis

Gandin, L.S. (1965). *Objective analysis of meteorological fields*. Israel Program for Scientific Translations

GCOS (2011). Systematic observation requirements for satellite-based data products for climate, 79-83

Gobron, N., Pinty, B., Aussedat, O., Chen, J.M., Cohen, W.B., Fensholt, R., Gond, V., Huemmrich, K.F., Lavergne, T., Melin, F., Privette, J.L., Sandholt, I., Taberner, M., Turner, D.P., Verstraete, M.M., & Widlowski, J.L. (2006). Evaluation of fraction of absorbed photosynthetically active radiation products for different canopy radiation transfer regimes: Methodology and results using Joint Research Center products derived from SeaWiFS against ground-based estimations. *Journal of Geophysical Research-Atmospheres, 111*, doi:10.1029/2005JD006511

Gobron, N., Pinty, B., Aussedat, O., Taberner, M., Faber, O., Melin, F., Lavergne, T., Robustelli, M., & Snoeij, P. (2008). Uncertainty estimates for the FAPAR operational products derived from MERIS - Impact of top-of-atmosphere radiance uncertainties and validation with field data. *Remote Sensing of Environment, 112*, 1871-1883

Gobron, N., Pinty, B., Verstraete, M., & Govaerts, Y. (1999). The MERIS Global Vegetation Index (MGVI): Description and preliminary application. *International Journal of Remote Sensing, 20*, 1917-1927

Gobron, N., Pinty, B., Verstraete, M.M., & Widlowski, J.L. (2000). Advanced vegetation indices optimized for up-coming sensors: Design, performance, and applications. *Ieee Transactions on Geoscience and Remote Sensing, 38*, 2489-2505

Gu, Y.X., Belair, S., Mahfouf, J.F., & Deblonde, G. (2006). Optimal interpolation analysis of leaf area index using MODIS data. *Remote Sensing of Environment, 104*, 283-296

Hall, F., Masek, J.G., & Collatz, G.J. (2006). Evaluation of ISLSCP Initiative IIFASIR and GIMMS NDVI products and implications for carbon cycle science. *Journal of Geophysical Research-Atmospheres, 111*, doi: 10.1029/2006JD007438

Hanan, N.P., Burba, G., Verma, S.B., Berry, J.A., Suyker, A., & Walter-Shea, E.A. (2002). Inversion of net ecosystem CO2 flux measurements for estimation of canopy PAR absorption. *Global Change Biology*, *8*, 563-574

He, T., Gao, F., Liang, S., Peng, Y., & Anderson, M. (2015). Mapping climatological bare soil albedo during 2000-2012 over the contiguous United States using MODIS data. *submitted*

He, T., Liang, S.L., Wang, D.D., Shuai, Y.M., & Yu, Y.Y. (2014). Fusion of Satellite Land Surface Albedo Products Across Scales Using a Multiresolution Tree Method in the North Central United States. *Ieee Transactions on Geoscience and Remote Sensing, 52*, 3428-3439

Houghton, R.A. (1995). Land-use change and the carbon-cycle. *Global Change Biology, 1*, 275-287

Hu, J.N., Su, Y., Tan, B., Huang, D., Yang, W.Z., Schull, M., Bull, M.A., Martonchik, J.V., Diner, D.J., Knyazikhin, Y., & Myneni, R.B. (2007). Analysis of the MISR LA/FPAR product for spatial and temporal coverage, accuracy and consistency. *Remote Sensing of Environment, 107*, 334-347

Hu, J.N., Tan, B., Shabanov, N., Crean, K.A., Martonchik, J.V., Diner, D.J., Knyazikhin, Y., & Myneni, R.B. (2003). Performance of the MISR LAI and FPAR algorithm: a case study in Africa. *Remote Sensing of Environment, 88*, 324-340

Huang, H.C., Cressie, N., & Gabrosek, J. (2002). Fast, resolution-consistent spatial prediction of global processes from satellite data. *Journal of Computational and Graphical Statistics, 11*, 63-88

Huemmrich, K.F., Privette, J.L., Mukelabai, M., Myneni, R.B., & Knyazikhin, Y. (2005). Time-series validation of MODIS land biophysical products in a Kalahari woodland, Africa. *International Journal of Remote Sensing, 26*, 4381-4398

Irving, W.W., Fieguth, P.W., & Willsky, A.S. (1997). An overlapping tree approach to multiscale stochastic modeling and estimation. *Ieee Transactions on Image Processing, 6*, 1517-1529

Jhee, H., Cho, H.-C., Kahng, H.-K., & Cheung, S. (2013). Multiscale quadtree model fusion with super-resolution for blocky artefact removal. *Remote Sensing Letters, 4*, 325-334

Kaminski, T., Knorr, W., Scholze, M., Gobron, N., Pinty, B., Giering, R., & Mathieu, P.P. (2012). Consistent assimilation of MERIS FAPAR and atmospheric CO2 into a terrestrial vegetation model and interactive mission benefit analysis. *Biogeosciences, 9*, 3173-3184

Kanniah, K.D., Beringer, J., Hutley, L.B., Tapper, N.J., & Zhu, X. (2009). Evaluation of Collections 4 and 5 of the MODIS Gross Primary Productivity product and algorithm improvement at a tropical savanna site in northern Australia. *Remote Sensing of Environment, 113*, 1808-1822

Knyazikhin, Y., Martonchik, J.V., Diner, D.J., Myneni, R.B., Verstraete, M., Pinty, B., & Gobron, N. (1998a). Estimation of vegetation canopy leaf area index and fraction of absorbed photosynthetically active radiation from atmosphere-corrected MISR data. *Journal of Geophysical Research-Atmospheres, 103*, 32239-32256

Knyazikhin, Y., Martonchik, J.V., Myneni, R.B., Diner, D.J., & Running, S.W. (1998b). Synergistic algorithm for estimating vegetation canopy leaf area index and fraction of absorbed photosynthetically active radiation from MODIS and MISR data. *Journal of Geophysical Research-Atmospheres, 103*, 32257-32275

Li, Z.Q., Whitlock, C.H., & Charlock, T.P. (1995). Assessment of the global monthly mean surface insolation estimated from satellite measurements using global energy-balance archive data. *Journal of Climate, 8*, 315-328

Liang, S. (2004). *Quantitative Remote Sensing of Land Surfaces*. New York: John Wiley & Sons, Inc.

Liang, S., Li, X., & Wang, J. (2012). *Advanced Remote Sensing: Terrestrial Information Extraction and Applications*. Academic Press, 2012, ISBN 9780123859556

Liang, S.L. (2007). Recent developments in estimating land surface biogeophysical variables from optical remote sensing. *Progress in Physical Geography, 31*, 501-516

Martinez, B., Camacho, F., Verger, A., Garcia-Haro, F.J., & Gilabert, M.A. (2013). Intercomparison and quality assessment of MERIS, MODIS and SEVIRI FAPAR products over the Iberian Peninsula. *International Journal of Applied Earth Observation and Geoinformation, 21*, 463-476

Maselli, F., Chiesi, M., Fibbi, L., & Moriondo, M. (2008). Integration of remote sensing and ecosystem modelling techniques to estimate forest net carbon uptake. *International Journal of Remote Sensing, 29*, 2437-2443

McCallum, A., Wagner, W., Schmullius, C., Shvidenko, A., Obersteiner, M., Fritz, S., & Nilsson, S. (2010). Comparison of four global FAPAR datasets over Northern Eurasia for the year 2000. *Remote Sensing of Environment, 114*, 941-949

Morisette, J.T., Baret, F., Privette, J.L., Myneni, R.B., Nickeson, J.E., Garrigues, S., Shabanov, N.V., Weiss, M., Fernandes, R.A., Leblanc, S.G., Kalacska, M., Sanchez-Azofeifa, G.A., Chubey, M., Rivard, B., Stenberg, P., Rautiainen, M., Voipio, P., Manninen, T., Pilant, A.N., Lewis, T.E., Iiames, J.S., Colombo, R., Meroni, M., Busetto, L., Cohen, W.B., Turner, D.P., Warner, E.D., Petersen, G.W.,

Seufert, G., & Cook, R. (2006). Validation of global moderate-resolution LAI products: A framework proposed within the CEOS Land Product Validation subgroup. *Ieee Transactions on Geoscience and Remote Sensing, 44*, 1804-1817

Morton, D.C., Nagol, J., Carabajal, C.C., Rosette, J., Palace, M., Cook, B.D., Vermote, E.F., Harding, D.J., & North, P.R.J. (2014). Amazon forests maintain consistent canopy structure and greenness during the dry season. *Nature, 506*, 221-224

Myneni, R.B., Hoffman, S., Knyazikhin, Y., Privette, J.L., Glassy, J., Tian, Y., Wang, Y., Song, X., Zhang, Y., Smith, G.R., Lotsch, A., Friedl, M., Morisette, J.T., Votava, P., Nemani, R.R., & Running, S.W. (2002). Global products of vegetation leaf area and fraction absorbed PAR from year one of MODIS data. *Remote Sensing of Environment, 83*, 214-231

Myneni, R.B., Yang, W.Z., Nemani, R.R., Huete, A.R., Dickinson, R.E., Knyazikhin, Y., Didan, K., Fu, R., Juarez, R.I.N., Saatchi, S.S., Hashimoto, H., Ichii, K., Shabanov, N.V., Tan, B., Ratana, P., Privette, J.L., Morisette, J.T., Vermote, E.F., Roy, D.P., Wolfe, R.E., Friedl, M.A., Running, S.W., Votava, P., El-Saleous, N., Devadiga, S., Su, Y., & Salomonson, V.V. (2007). Large seasonal swings in leaf area of Amazon rainforests. *Proceedings of the National Academy of Sciences of the United States of America, 104*, 4820-4823

Olofsson, P., & Eklundh, L. (2007). Estimation of absorbed PAR across Scandinavia from satellite measurements. Part II: Modeling and evaluating the fractional absorption. *Remote Sensing of Environment, 110*, 240-251

Pickett-Heaps, C.A., Canadell, J.G., Briggs, P.R., Gobron, N., Haverd, V., Paget, M.J., Pinty, B., & Raupach, M.R. (2014). Evaluation of six satellite-derived Fraction of Absorbed Photosynthetic Active Radiation (FAPAR) products across the Australian continent. *Remote Sensing of Environment, 140*, 241-256

Pinty, B., Clerici, M., Andredakis, I., Kaminski, T., Taberner, M., Verstraete, M.M., Gobron, N., Plummer, S., & Widlowski, J.L. (2011). Exploiting the MODIS albedos with the Two-stream Inversion Package (JRC-TIP): 2. Fractions of transmitted and absorbed fluxes in the vegetation and soil layers. *Journal of Geophysical Research-Atmospheres, 116*

Preisendorfer, R. (1988). *Principal Component Analysis in Meteorology and Oceanography*. Elsevier

Ross, J. (1981). *The Radiation Regime and Architecture of Plant Stands*. The Hague, Boston and London: Dr. W. Junk Publishers

Seixas, J., Carvalhais, N., Nunes, C., & Benali, A. (2009). Comparative analysis of MODIS-FAPAR and MERIS-MGVI datasets: Potential impacts on ecosystem modeling. *Remote Sensing of Environment, 113*, 2547-2559

Serbin, S.P., Ahl, D.E., & Gower, S.T. (2013). Spatial and temporal validation of the MODIS LAI and FPAR products across a boreal forest wildfire chronosequence. *Remote Sensing of Environment, 133*, 71-84

Shabanov, N.V., Huang, D., Yang, W.Z., Tan, B., Knyazikhin, Y., Myneni, R.B., Ahl, D.E., Gower, S.T., Huete, A.R., Aragao, L., & Shimabukuro, Y.E. (2005). Analysis and optimization of the MODIS leaf area index algorithm retrievals over

broadleaf forests. *Ieee Transactions on Geoscience and Remote Sensing, 43*, 1855-1865

Steinberg, D.C., Goetz, S.J., & Hyer, E.J. (2006). Validation of MODIS F-PAR products in boreal forests of Alaska. *Ieee Transactions on Geoscience and Remote Sensing, 44*, 1818-1828

Tao, X., Liang, S., & He, T. (In review). Estimation of fraction of absorbed photosynthetically active radiation from multiple satellite data: Model development and validation. *Remote Sensing of Environment*

Tao, X., Liang, S., & Wang, D.D. Assessment of five global satellite products of fraction of absorbed photosynthetically active radiation: Intercomparsion and direct validation against ground-based data. *Remote Sensing of Environment, 2015*, http://dx.doi.org/10.1016/j.rse.2015.1003.1025

Tao, X., Yan, B., Wang, K., Wu, D., Fan, W., Xu, X., & Liang, S. (2009). Scale transformation of leaf area index product retrieved from multi-resolution remotely sensed data: Analysis and case studies. *International Journal of Remote Sensing, 30*, 5383-5395

Tian, Y., Dickinson, R.E., Zhou, L., Zeng, X., Dai, Y., Myneni, R.B., Knyazikhin, Y., Zhang, X., Friedl, M., Yu, II, Wu, W., & Shaikh, M. (2004). Comparison of seasonal and spatial variations of leaf area index and fraction of absorbed photosynthetically active radiation from Moderate Resolution Imaging Spectroradiometer (MODIS) and Common Land Model. *Journal of Geophysical Research-Atmospheres, 109*, doi: 10.1029/2003JD003777

Turner, D.P., Ritts, W.D., Cohen, W.B., Maeirsperger, T.K., Gower, S.T., Kirschbaum, A.A., Running, S.W., Zhao, M.S., Wofsy, S.C., Dunn, A.L., Law, B.E., Campbell, J.L., Oechel, W.C., Kwon, H.J., Meyers, T.P., Small, E.E., Kurc, S.A., & Gamon, J.A. (2005). Site-level evaluation of satellite-based global terrestrial gross primary production and net primary production monitoring. *Global Change Biology, 11*, 666-684

Vina, A., & Gitelson, A.A. (2005). New developments in the remote estimation of the fraction of absorbed photosynthetically active radiation in crops. *Geophysical Research Letters, 32*

Wang, D.D., & Liang, S.L. (2011). Integrating MODIS and CYCLOPES Leaf Area Index Products Using Empirical Orthogonal Functions. *Ieee Transactions on Geoscience and Remote Sensing, 49*, 1513-1519

Wang, Y., Tian, Y., Zhang, Y., El-Saleous, N.Z., Knyazikhin, Y., Vermote, E.F., & Myneni, R.B. (2001). Investigation of product accuracy as a function of input and model uncertainties: Case study with SeaWiFS and MODIS LAI/FPAR algorithm. *Remote Sensing of Environment, 78*, 299-313

Weiss, M., Baret, F., Garrigues, S., & Lacaze, R. (2007). LAI and fAPAR CYCLOPES global products derived from VEGETATION. Part 2: validation and comparison with MODIS collection 4 products. *Remote Sensing of Environment, 110*, 317-331

Widlowski, J.L., Taberner, M., Pinty, B., Bruniquel-Pinel, V., Disney, M., Fernandes, R., Gastellu-Etchegorry, J.P., Gobron, N., Kuusk, A., Lavergne, T., Leblanc, S., Lewis, P.E., Martin, E., Mottus, M., North, P.R.J., Qin, W., Robustelli, M., Rochdi,

N., Ruiloba, R., Soler, C., Thompson, R., Verhoef, W., Verstraete, M.M., & Xie, D. (2007). Third Radiation Transfer Model Intercomparison (RAMI) exercise: Documenting progress in canopy reflectance models. *Journal of Geophysical Research-Atmospheres, 112*, Art. No. D09111

Xu, X., Fan, W., & Tao, X. (2009). The spatial scaling effect of continuous canopy leaves area index retrieved by remote sensing. *Science in China Series D-Earth Sciences, 52*, 393-401

Yang, W.Z., Huang, D., Tan, B., Stroeve, J.C., Shabanov, N.V., Knyazikhin, Y., Nemani, R.R., & Myneni, R.B. (2006). Analysis of leaf area index and fraction of PAR absorbed by vegetation products from the terra MODIS sensor: 2000-2005. *Ieee Transactions on Geoscience and Remote Sensing, 44*, 1829-1842

Zhang, Q., Xiao, X., Braswell, B., Linder, E., Baret, F., & Moore III, B. (2005). Estimating light absorption by chlorophyll, leaf and canopy in a deciduous broadleaf forest using MODIS data and a radiative transfer model. *Remote Sensing of Environment, 99*, 357 – 371

Zhu, J., Morgan, C.L.S., Norman, J.M., Yue, W., & Lowery, B. (2004). Combined mapping of soil properties using a multi-scale tree-structured spatial model. *Geoderma, 118*, 321-334

Zubko, V., Leptoukh, G.G., & Gopalan, A. (2010). Study of Data-Merging and Interpolation Methods for Use in an Interactive Online Analysis System: MODIS Terra and Aqua Daily Aerosol Case. *Ieee Transactions on Geoscience and Remote Sensing, 48*, 4219-4235

WWW Sites

WWW1: The VALERI validation data.

http://w3.avignon.inra.fr/valeri/fic_htm/database/main.php

WWW2: The AmeriFlux validation data. http://ameriflux.ornl.gov/

WWW3: The MODIS Collection 5 data.

http://ladsweb.nascom.nasa.gov/data/search.html

WWW4: The MISR data. http://l0dup05.larc.nasa.gov/MISR/cgi-bin/MISR/main.cgi

WWW5: The geoland2 GEOV1 product.

http://land.copernicus.eu/global/products/FAPAR

WWW6: The MERIS data. https://earth.esa.int/web/guest/data-access/browse-data-products

WWW7: The SeaWiFS data.

http://fapar.jrc.ec.europa.eu/WWW/Data/Pages/FAPAR_Download/FAPAR_Download.php#a_dataTable

WWW8: The Landsat TM and ETM+ data. http://espa.cr.usgs.gov/